

**Kelvin-Helmholtz Instability at Earth's magnetopause: THEMIS
Observations and OpenGGCM Simulations**

by

Shiva Kavosi

B.S., Applied Physics, Shahid Chamran University, 2006

M.S., Plasma Physics, Shahid Beheshti University, 2009

DISSERTATION

Submitted to the University of New Hampshire
in partial fulfillment of
the requirements for the degree of

Doctor of Philosophy

in

Physics

September 2015

ALL RIGHTS RESERVED

© 2015

Shiva Kavosi

This thesis/dissertation has been examined and approved in partial fulfillment of the requirements for the degree of Doctor of Philosophy in Physics by

Thesis director, Joachim Raeder

Professor, Department of Physics

Charlie Farrugia

Professor, Department of Physics

Martin A. Lee

Professor, Department of Physics

Kai Germaschewski

Associate Professor, Department of Physics

Patricia Solvignon

Assistant Professor, Department of Physics

On August 11, 2015

Dedication

To my Mom, Mahnaz

Acknowledgments

I have taken efforts in this project. However, I would never have been able to finish this dissertation without the guidance of my Advisor, my committee members, and support from my family and friends.

First, I thank my advisor, Prof. Jimmy Raeder for the continuous support of my PhD research, for his motivation, enthusiasm, and immense knowledge. His guidance helped me in all the time of my research. Thank you for sending me out to summer schools, meetings, workshops, and conferences where I had the opportunity of meeting researchers of our field. Thank you for submitting my paper to Nature journal.

I am grateful to, Prof. Charlie Farrugia, Prof. Marty Lee, Dr. Kai Germaschewski, and Dr. Patricia Solvignon for sitting on my thesis committee. I especially thank Dr. Charlie Farrugia, who in many respects, patiently helping me through my research and answers all my questions.

I appreciate everyone at THEMIS team, who contributed the observational data for this research and for providing the THEMIS Data Analysis Software (TDAS), which definitely sped up the completion of this work.

I would like to thank Matthew Gilson for his Pyggcm and Pyprobe package. I am also grateful to, Kris Maynard and Steve Abbott for their patience and time to answer all my programing questions. Thank you all, without your help, my research would have taken longer to be accomplished.

I deeply appreciate Banafsheh and Narges for being great friends and for the memories and fun times during conferences and workshops. I am especially grateful to, Banafsheh, who was the best office mate I could ever ask for.

I would like to thank my family especially my cousin, Vida for supporting me spiritually throughout the exhausted days of the graduate school.

I also wish to thank my fiancé, Yasser, for being next to me during these years. Yasser, thank you for editing my dissertation, without your help I would not finish my dissertation on time.

Table of Contents

Dedication	iv
Acknowledgments	v
Table of Contents	vi
List of Tables	ix
List of Figures	x
ABSTRACT	xix
1. Introduction	1
1.1 The Solar Wind	1
1.2 The Earth's Magnetosphere	3
1.3 The Magnetopause	6
1.4 Magnetopause Instabilities and Oscillations	7
1.4.1 Magnetic Reconnection	8
1.4.2 Kelvin-Helmholtz Instability.....	11
1.4.3 Ubiquity of Kelvin-Helmholtz Instability throughout Universe	22
1.5 Outline of Thesis	24
2. Kelvin-Helmholtz vortices at Earth's Magnetopause	25
2.1 Introduction	25
2.2 Earlier studies: Simulations and Observations	27
2.3 Mass and Energy Transfer within Vortices	30
2.3.1 Magnetic Reconnection	30
2.3.2 Secondary Instabilities and Turbulence	32
2.4 Kelvin-Helmholtz waves and Flux-Transfer Events (FTEs).....	35

2.4.1	Flux Transfer Event identification.....	35
2.4.2	Kelvin-Helmholtz Vortex identification	39
2.5	THEMIS Observations of KH waves and FTEs	44
2.5.1	KH waves in linear stage on 01/13/2012.....	44
2.5.2	KH waves in nonlinear stage on 04/19/2008.....	47
2.5.3	KH waves under southward IMF on 02/27/2012.....	50
2.5.4	FTEs Event 1 on 11/30/2012.....	54
2.5.5	FTEs Event 2 on 12/16/2012.....	56
2.6	KH vortices or FTEs.....	59
2.6.1	FTEs and KH waves on 01/02/2011.....	60
2.7	Summary	66
3.	Ubiquity of Kelvin-Helmholtz waves at Earth's Magnetopause	68
3.1	Introduction.....	68
3.2	Event selection.....	69
3.3	Statistical Results.....	71
3.3.1	Occurrence rate	72
3.3.2	IMF dependence	75
3.3.3	Solar wind parameter dependences.....	77
3.4	Discussion and Conclusions.....	79
4.	Simulation results: OpenGGCM	82
4.1	Introduction.....	82
4.2	The OpenGGCM.....	83
4.3	Generic Runs: Constant Solar Wind.....	84
4.3.1	Overview of simulation results.....	85
4.3.2	Effect of magnetic field magnitude.....	93
4.3.3	Effect of boundary layer thickness.....	96
4.3.4	Effect of numerical resolution.....	100
4.4	Event study: THEMIS Observations.....	103
4.4.1	THEMIS Observations on 07/06/2014	103
4.4.2	OpenGGCM simulation of THEMIS Observations.....	106
4.5	Discussion and conclusions	112

5. Discussion and Future Work	115
5.1 Discussion and Conclusions.....	115
5.2 Future works.....	118
5.2.1 Dawn-dusk asymmetry.....	118
5.2.2 Kelvin-Helmholtz instability under southward IMF.....	120
Bibliography	123

List of Tables

Table 2-1: Summary of FTE separation times	38
Table 2-2: Comparison between the properties of FTEs and non-linear KH wave	61
Table 4-1: Solar Wind input Parameters	85

List of Figures

Figure 1.1: A schematic diagram illustrating how the rotation of the solar wind source region creates a Parker Spiral configuration due to the frozen in theorem. Figure downloaded from http://how.gi.alaska.edu/ao/msp/chapters/chapter6.pdf	3
Figure 1.2: Chapman-Ferraro cavity and dipole and bullet shaped magnetosphere: (a) Disturbed dipole field geometry in the mirror method, (b) Chapman-Ferraro cavity, and (c) Formation of the bullet-shaped magnetosphere in the moving solar wind.	4
Figure 1.3: An illustration of Earth's magnetosphere and currents (Crooker et al. 1999).....	5
Figure 1.4: Illustration of particle dynamics at Chapman-Ferraro-Type. Figure downloaded from Magnetopause. http://how.gi.alaska.edu/ao/msp/chapters/chapter8.pdf	7
Figure 1.5: Topological structure of 2D reconnection (a), (b), and (c) Dungey's reconnection model (1961): locations of magnetic reconnection at sub- solar magnetopause as well as in tail plasma sheet.	10
Figure 1.6: Shear Boundary layer Ong and Roderick (1972).	17
Figure 1.7: Growth rate versus wave number. Effect of the boundary layer thickness and parallel magnetic field. A is Alfvén Mach number from Ong and Roderick (1972).....	18
Figure 1.8: Growth rate versus wave number. Effect of the boundary layer thickness and compressibility. M is Magnetosonic Mach number from Ong and Roderick (1972).....	19

Figure 1.9: Normalized growth rate for KH instability with flow perpendicular to magnetic field. Maximum growth occurs when, $k_y \Delta \sim 0.5 - 1$, where k_y is the wave-vector along the flow direction and $\Delta = 2a$ is the width of the shear layer from Miura and Pritchett (1982) 21

Figure 1.10: (a) KH waves observed at Sun. (b) observed at atmosphere of Jupiter (c) observed at Saturn (d) breaking wave pattern made in clouds. 23

Figure 2.1: KH vortex at the Earth’s magnetopause adapted (Fairfield, 2000). 26

Figure 2.2: Schematic of reconnection in a K–H Vortex from Nykyri and Otto (2001). 32

Figure 2.3: Number density profiles with flow vectors obtained by the ideal MHD simulation. The onset of secondary KH waves grow within the parent vortex is observed in Figure 2.2b. Turbulence is produced within the vortex in Figure 2.3c and Figure 2.3d. From Matsumoto, et al. (2004). 34

Figure 2.4: Taxonomy of magnetosheath (left) and magnetospheric (right) FTEs by Paschmann et al. (1982) and Elphic (1995). B is observed magnetic field, N is plasma density, V is bulk speed, T is temperature, and EP is energetic particle flux. 37

Figure 2.5: Schematic drawing of rolled-up KH vortices at the dusk-flank magnetopause. The relationship between the streamline pattern (black lines) and total (magnetic plus plasma) pressure and density (red, dense; blue, tenuous) distributions, when viewed in the vortex rest frame. The sub-solar region is to the left. The total pressure minimizes at the center (L) of the vortices, while it maximizes at the hyperbolic point (H), which is a flow stagnation point in the vortex rest frame, and around which the streamlines form hyperbolas (Miura, 1997). It is expected that magnetosphere-to-magnetosheath transitions be characterized by large and rapid density increases coincide with maxima in the total pressure (see example in Figure 2.6). From Hasegawa, (2012). 40

Figure 2.6: KH vortices observed by Cluster. Quasi-periodic fluctuations of the bulk plasma parameters during Cluster 1 (C1) observations of rolled-up KH vortices showing: (a) Ion density, (b) M and N components of the smoothed velocity (c) total pressure (magnetic plus ion pressure),

and (d) wavelet spectra of the total pressure. Note that density jumps from the magnetospheric to magnetosheath values closely coincide with total pressure maxima (red vertical dashed lines), as expected in developed KH vortices and explained in Figure 2.5. From Hasegawa, (2012). 42

Figure 2.7: MHD simulation of KH waves. Plasma density (left column) and scatter plots of the x (sunward) component of the velocity V_x versus plasma density N/N_0 , at different stages of 3D MHD KH instability simulations generated from virtual spacecraft observations of the simulated KH wave or vortex. The left panels show the normalized density in the x-y plane in color. The initial values of V_x are -1 and $+1$ on the magnetosheath and on the magnetospheric side, respectively. Within the rolled-up vortex (top), a significant fraction of low-density plasma ($N/N_0 < 0.5$) has an anti-sunward speed higher than that of the magnetosheath plasma characterized by $V_x = -1$ and $N/N_0 = 1$. In the linear and not-yet-rolled-up stages (bottom two rows) no such relation exists (from Hasegawa et al. 2006). 43

Figure 2.8: Geotail observation of solar wind parameters on 13 Jan 2012. From top to bottom: magnetic field components by (red), b_x (blue), b_z (black), X component of the velocity V_x , (c) wavelet spectrum of V_x , rr density, and wavelet spectrum of the density, rr. The red vertical lines shows the event interval. The frequency of oscillations in solar wind is ~ 0.004 Hz ($T \sim 250$ s). 45

Figure 2.9: Time series data from THEMIS E on 13 Jan 2012. From top to bottom: (a) Ion density, (b) M component of the velocity V_m , (c) N components of the velocity V_n , (d) N component of magnetic field B_n , (e) Magnetic field magnitude B_{tot} , (f) total (magnetic plus ion) pressure, (g) Omnidirectional ion energy flux spectrogram, and (h) wavelet spectrum of the total pressure. The wave period is approximately 90 s. 46

Figure 2.10: Scatter plot of the velocity component, V_x , tangential to the nominal magnetopause, versus ion density for the event shown in Figure 2.9. The $-X$ direction is roughly along the $-M$ direction, i.e., tangential to the magnetopause and anti- sunward. The plot confirms that there has no low-density plasma with anti-sunward speed higher than that of the magnetosheath plasma. The horizontal dashed line is the velocity of magnetosheath plasma and the red circle shows where we expect low density and high speed plasma. No particles depicted as black star in red circle indicates that the KH waves are in linear stage. 47

Figure 2.11: Time series of data for THEMIS C on 19 April 2008. Kelvin–Helmholtz waves observed at the dawn flank magnetopause by THEMIS C on 19 April 2008. The panels show, from top to bottom: (a) the ion number density, (b) the M component of ion velocity, (c) normal component of the ion velocity vector, (d) normal component of magnetic field, (e) total magnetic field, (f) total (magnetic plus ion) pressure, (g) omnidirectional ion energy spectrogram, and (h) wavelet spectra of the total pressure. The wave period is approximately 100 s. 49

Figure 2.12: Scatter plot of the ion velocity V_x component versus ion density. The data are from THEMIS C for the 19 April 2008 event. Each symbol represents one of the samples, which were taken at 5 min cadence. Negative V_x values indicate anti-sunward flow. The plot confirms that this event consists of rolled-up KH vortices, because a fraction of the low-density magnetospheric plasma, indicated by the red ellipse, flows faster than the magnetosheath plasma ($> 350 \text{ km s}^{-1}$, shown by the dashed red line). 50

Figure 2.13 Wind observations of solar wind parameters on 27 Feb 2012. . From top to bottom: magnetic field components by (red), b_x (blue), b_z (black), X component of the velocity V_x , wavelet spectrum of V_x , density, n_r , and wavelet spectrum of the density. The red vertical lines shows the event interval. The frequency of ocsilations in solar wind is $\sim 0.025 \text{ Hz}$ ($T \sim 400 \text{ s}$). 52

Figure 2.14: Time series of data in GSM THEMIS E observations on 27 Feb 2012. From top to bottom: (a) Ion density, (b) M component of the velocity V_m , (c) N components of the velocity V_n , (d) N component of magnetic field B_n , (e) Magnetic field magnitude B_{tot} , (f) total (magnetic plus ion) pressure, (g) Omnidirectional on ion energy flux, and (h) wavelet spectra of the total pressure. For the interval 1240-1250 the wave period is approximately 60 s. 53

Figure 2.15: Time series of data in GSM THEMIS A observation on 30 Nov 2012. From top to bottom: (a) Ion density, (b) M component of the velocity V_m , (c) N components of the velocity V_n , (d) N component of magnetic field B_n , (e) Magnetic field magnitude B_{tot} , (f) total (magnetic plus ion) pressure, (g) Omni-directional ion energy flux, and (h) wavelet spectrum of the total pressure. The red vertical dashed lines mark the approximate centers of the FTEs. 55

Figure 2.16: V_x - N scatter plot in the same format as previously shown, for the 11/30/2012 event. The data are from THEMIS A for 30 Nov 2012 event. Each symbol represents one of the samples, which were taken at 5 min cadence. Negative V_x values indicate anti-sunward flow. The red circle designates the area where one would expect data points if rolled-up KH vortices existed. The V_x - N profile is clearly different than the KH waves profile illustrates in Figure 2.5..... 56

Figure 2.17: Time series of data in GSM taken by the THEMIS D on 16 Dec 2010. From top to bottom: (a) Ion density, (b) M component of the velocity (in the Earth's rest frame) V_M , (c) N components of the velocity V_N , (d) N component of magnetic field B_N , (e) Magnetic field magnitude B_{tot} , (f) total (magnetic plus ion) pressure, (g) Omnidirectional ion energy flux spectrogram. The red vertical dashed lines mark the approximate centers of the FTEs..... 58

Figure 2.18: V_x - N scatter plot for the 11/30/2012 event. The data are from THEMIS D on 16 Dec 2010. Each symbol represents one of the samples, which were taken at 5 min cadence. This is from a series of FTEs and shows a distribution that is distinctively different from KH wave. 59

Figure 2.19: THEMIS A observations on 2 January 2011. From top to bottom: (a) Ion density, (b) M component of the velocity V_m , (c) N components of the velocity V_n , (d) N component of magnetic field B_n , (e) Magnetic field magnitude B_{total} , (f) total (magnetic plus ion) pressure, (g) Omni-directional ion energy flux, and (h) wavelet spectrum of the total pressure. The red vertical dashed lines mark the approximate centers of the FTEs during the first part of the interval 1125-1155 and passes through the edge of KH waves during 1155-1215..... 63

Figure 2.20: Scatter plot of the velocity component, V_x , tangential to the nominal magnetopause versus ion density seen in the rolled-up vortices detected by THEMIS. The event is the same as the one shown in Figure 2.19. Here, the -x direction is defined to be along the ion velocity (in GSM) averaged over the interval under investigation (1130 - 1215 UT), and is roughly along the -M direction (anti-sunward) in LMN coordinates. The red stars have shown the first part of the event (1130-1150), FTEs. The black stars have shown the second part of the event (1155-1215), KH waves. There is some low-density plasma (circled in red) that flows faster than magnetosheath plasma, confirming that rolled-up vortices are present. These data points all come

from the second part of the event, i.e., 1155 – 1215 UT illustrated as a black stars as shown in the red circle..... 64

Figure 2.21: THEMIS D observations on 2 January 2011. From top to bottom: (a) Ion density, (b) M component of the velocity V_m , (c) N components of the velocity V_n , (d) N component of magnetic field B_n , (e) Magnetic field magnitude B_{total} , (f) total (magnetic plus ion) pressure, (g) Omni-directional ion energy flux, and (h) wavelet spectrum of the total pressure. The interval 1120-1150 shows FTEs signitures. 65

Figure 3.1: THEMIS orbita phases. Dusk phase(a) the apogee of the orbits is on the dusk side of the magnetosphere. Dawn phase (b) the apogee of the orbits is on the dawn side of magnetsphere. Probe 1 apogee (red) is at 30 Re, Probe 2 (green) at 20 Re, Probes 3 (dark blue), 4 (pink) , and 5 (light blue) at 12 Re. Dusk phase and dawn phase (c),(d). Since 2011, probes 3 and 4 apogees have changed to 12 Re, and Probe 5 apogee (light blue) has changed to 13 Re. P1 and P2 have now become ARTEMIS..... 71

Figure 3.2: Scattorplot of occurrence of KH waves and total magnetopause crossings, for different years from 2007 to 2013. The distribution of occurrence of all events (KHI and total magnetopause crossings) is plotted for different clock angle and velocities. Each dot shows five minute of magnetopause crossing. Color shows details about wave kind KH waves (orange) and total events (gray)..... 73

Figure 3.3: Top panel (a) shows occurrence rate of KH wave for different years 2007-2013. Orange bins show the relative KH wave occurrence rate and grey bins show the number of 5-min KH wave intervals in that bin. Bottom panel (b) shows sunspot number from 2001-2018. The red circle shows the interval of our THEMIS survey 2007-2013. 74

Figure 3.4: KH waves occurrence rate as a function of IMF clock angle (a) and cone angle(b). The clock angle is defined as $\text{atan}(B_y/B_z)$, and the cone angle is defined as $\text{acos}(B_x/B)$. X points towards the Sun, Y points duskward, Z points north, and $R = (Y^2 + Z^2)^{1/2}$ 75

Figure 3.5: The duration of KH waves event versus different clock angles. 76

Figure 3.6: Occurrence rate of KH wave as a function of solar wind plasma parameters. Orange bins show the relative KH wave occurrence rate and grey bins show the number of 5-min KH wave intervals in that bin. The panels show, respectively, the dependence on the solar wind velocity (a), the solar wind density (b), the solar wind Mach number, and (c) the IMF magnitude. The parameter dependence is mostly as expected from the KH dispersion relation, but the significant occurrence rate at low velocity (<300 km/s) is not expected. 78

Figure 4.1: Time series of OpenGGCM simulation under constant solar wind at the point close to terminator (+3, -9, 0). From top to bottom: Ion density n_r , x component of the velocity V_x , y components of the velocity V_y , x and y components of magnetic field B_x , B_y , Magnetic field magnitude B_{tot} , total (magnetic plus ion) pressure, and wavelet spectrum of the y component of velocity 87

Figure 4.2: OpenGGCM simulation under constant solar wind at (-10, -15.5, 0) downstream of the dawn meridian. From top to bottom: Ion density n_r , x component of the velocity V_x , y components of the velocity V_y , x and components of magnetic field B_x , B_y , Magnetic field magnitude B_{tot} , total (magnetic plus ion) pressure, and wavelet spectrum of the y component of velocity 88

Figure 4.3: OpenGGCM simulations under constant solar wind condition at (-10,-15.5,0). Left panel is time series of simulation result under southward IMF (first hour of simulation). Right panel features the time series of simulation results under northward IMF (second hour of simulation result). From top to bottom: Ion density n_r , x component of the velocity V_x , y components of the velocity V_y , x and components of magnetic field B_x and B_y , Magnetic field magnitude B_{tot} , total (magnetic plus ion) pressure, and wavelet spectrum of the y component of velocity 89

Figure 4.4: Scatterplots of the velocity V_x versus plasma density N from OpenGGCM simulation for southward IMF on the left and color-coded current density plots on the right. The blue dot in color-coded current density plots on the right shows the location of virtual spacecraft. The top left scatterplot confirms that the simulated KH waves are in linear stage. The bottom left scatterplot shows no low-density magnetospheric plasma, indicated by the red ellipse flowing faster than magnetosheath plasma. 91

Figure 4.5: Scatterplots of the velocity V_x versus plasma density N from OpenGGCM simulation for northward IMF on the left and color-coded current density plots on the right. The blue dot in color-coded current density plots on the right shows the location of virtual spacecraft. The top left scatterplot confirms that the simulated KH waves are in linear stage. The bottom left scatterplot confirms that a fraction of the low-density magnetospheric plasma indicated by the red ellipse flows faster than magnetosheath plasma..... 92

Figure 4.6: Time series of OpenGGCM simulations for northward IMF at (-10,-15.5,0). The 01:20-02:00 interval is for magnetic field magnitude $|B|=5$ nT. The second interval 02:00-03:00 is for $|B|=10$ nT. 95

Figure 4.7: Scatter plots of the velocity V_x versus plasma density N for OpenGGCM simulation for northward IMF intervals. The left panel is a scatterplot for KH waves for northward IMF and $|B|=5$ nT(second hour in simulation) and the scatterplots on the right is for KH waves for northward IMF and $|B|=10$ nT. (Third hour in simulation). Both panels confirm that that a fraction of the low-density magnetospheric plasma indicated by the red ellipse flows faster than magnetosheath plasma. the KH waves are in nonlinear stage. 96

Figure 4.8: Velocity profile V_x -Y near the KH wave region for the OpenGGCM simulation. The top panel is from simulation results under southward IMF, the middle panel is for simulation result under northward IMF ($|B|=5$ nT) and the bottom panel is for simulation result under northward IMF ($|B|=10$ nT). The vertical dashed line is the location of the IEBL while the vertical solid line is the location of the magnetopause. The region between these two lines, d , is the simulation boundary layer..... 99

Figure 4.9: Color-coded current density plots from OpenGGCM simulation. The color-coding shows the current density in the equatorial plane. The plots on the left panel related to simulation with reduced resolution with center of grids shifted to dawn. The plots on the middle panel related to simulation with resolution with high resolution not center shifted. The plots on the right panel related to simulation with reduced resolution and center of grids shifted to dusk. 101

Figure 4.10: Geotail observations of solar wind parameters on 7 June 2014. From top to bottom: magnetic field components by (red), b_x (blue), b_z (black, X component of the velocity V_x , (c)

wavelet spectrum of V_x , rr density, and wavelet spectrum of the density, rr . The red vertical dashed lines show the event interval. 104

Figure 4.11: THEMIS E observations on 7 June 2014. From top to bottom: (a) Ion density, (b) M component of the velocity V_m , (c) N components of the velocity V_n , (d) N components of magnetic field B_N , (e) Magnetic field magnitude B_{total} , (f) total (magnetic plus ion) pressure, (g) Omni-directional ion energy flux, and (h) wavelet spectrum of density. 105

Figure 4.12: A comparison of THEMIS observations with OpenGGCM simulation. On 7 June 2014. Left panel is OpenGGCM result: From top to bottom: Ion density rr , x component of the velocity V_x , y components of the velocity V_y , x and components of magnetic field B_x and B_y , Magnetic field magnitude B_{tot} , total (magnetic plus ion) pressure, and wavelet spectrum of the y component of velocity. Right panel are THEMIS observations. From top to bottom: (a) Ion density, (b) M component of the velocity V_m , (c) N components of the velocity V_n , (d) N component of magnetic field B_n , (e) Magnetic field magnitude B_{tot} , (f) total (magnetic plus ion) pressure, (g) ion energy flux, and (h) wavelet spectrum of density. 108

Figure 4.13: A comparison of THEMIS observations with OpenGGCM simulation. Scatter plot of the ion velocity V_x versus ion density. The plots on the left panel are for OpenGGCM simulations. 109

Figure 4.14: OpenGGCM simulation of event observed by THEMIS on 7, June 2014 shown in Figure 4.9. The color-coding shows the current density in the equatorial plane. 110

Figure 4.15: Velocity profile near the KH wave region for a particular timestep for the OpenGGCM simulation of THEMIS event for two different intervals: The left plot simulated boundary layer under southward IMF. The right plot is simulated boundary layer under northward IMF. The region between these two vertical dashed lines, d , is the simulation boundary layer. 111

ABSTRACT

Kelvin-Helmholtz Instability at the Earth's magnetopause: THEMIS Observations and OpenGGCM Simulations

by

Shiva Kavosi

University of New Hampshire, September, 2015

Magnetic reconnection is believed to be the dominant process by which solar wind plasma enters the magnetosphere. However, for periods of northward interplanetary magnetic field (IMF) reconnection is less likely at the dayside magnetopause, and Kelvin-Helmholtz (KH) waves may be important agents for plasma entry and for the excitation of ultra-low-frequency (ULF) waves. The relative importance of KH waves is controversial because no statistical data on their occurrence frequency exists. Here we survey seven years of in-situ data from the NASA THEMIS (Time History of Events and Macro scale Interactions during Substorms) mission in order to create a database of magnetopause crossings throughout the entire mission in motivation to investigate the occurrence rate of KH waves at the Earth's magnetopause. Our analysis, using very conservative criteria to positively identify KH waves, has shown that KH waves at the Earth's magnetopause are ubiquitous and are present approximately 19% of the time regardless

of the solar wind conditions. This occurrence frequency is much higher than has been previously thought and suggests that KH waves may be more important for plasma transport across the magnetopause, and frequently drive magnetospheric ULF waves.

Our statistical analysis shows that the occurrence rate of KH waves increases with solar wind speed, Alfvén Mach number, and number density, but is mostly independent of IMF magnitude. The occurrence rate increases with the IMF cone angle and maximizes at zero clock angle at about 35% for near northward IMF, and about 10% under southward IMF conditions. Although the occurrence rate under southward IMF is significantly higher than previously detected, it is still approximately four times less than the occurrence rate under northward IMF. The previous study suggested that the irregular and temporally intermittent structure of KH waves due to dynamically active sub solar behavior under southward IMF condition may explain the preferential in situ detection of KH waves under northward IMF. This explanation is also consistent with the KH waves under southward IMF in our database. The majority of the events during southward IMF are irregular, short and polychromatic in compared to regular, long lasting and monochromatic waves under northward IMF. To effectively isolate these differences, we performed OpenGGCM global simulations for both constant idealized solar wind and a THEMIS event under southward IMF conditions. The simulation results also show that the KH waves under southward IMF are irregular, higher frequency, and polychromatic in compared to northward IMF.

Chapter 1

Introduction

1.1 The Solar Wind

The Sun is composed of 90% hydrogen, 10% helium, and an admixture of 0.1% heavier atoms. These solar materials are ionized due to the extremely high temperature, which results from the nuclear reaction occurring at the sun's highly compressed core. Therefore, a large electric field created between the protons and electrons causes protons accelerating outwards. The continuous streaming away of the accelerated charged particles results in the supersonic expansion (300-800 km/s) of the solar corona into interplanetary space. This supersonic coronal flowing away is called solar wind. In the mid-1950s, the British mathematician Sydney Chapman calculated the properties of a high-temperature gas and determined it to be a conductor of heat that must extend out into space beyond Earth's orbit (Chapman, 1957). Additionally, in the 1950s a German scientist named Ludwig Biermann proposed that whenever a comet is headed towards or away from the Sun, its tail always points away from the Sun. According to Eugene Parker's theory (1958), the phenomenon of solar wind originates from the Sun's corona and

ceases at the boundary of interstellar space. In fact, the solar wind has several source regions along with its properties depending upon which region it originated from. The two primary types of solar wind are known as “slow” solar wind (~ 400 km/s) and “fast” solar wind (~ 700 km/s). High-speed streams of solar wind escape from coronal holes (regions of open magnetic field lines) and travel out quite unrestricted by the Sun’s magnetic field in to the Heliosphere. The plasma in a coronal hole is cooler and lower in density than on average, thus the high-speed solar wind is also cooler and lower in density. Low-speed flows are thought to originate from the outer regions of coronal streamers. Another source of solar wind plasma are large transient events called coronal mass ejections (CMEs). Magnetic reconnection of complex field lines in the solar corona is considered to be the primary driver behind them. The first spacecraft observations of the solar wind were made by the Luna 1 and were verified by Luna 2 and Luna 3 spacecraft in 1959. Three years later their measurements were recorded by Americans, using the Mariner 2 spacecraft. The interplanetary space is filled by interplanetary magnetic field (IMF). Because of its large conductivity, the solar wind is often assumed to be an ideal Magnetohydrodynamics (MHD) fluid. The ideal (MHD) fluid treatment assumes the IMF is frozen in the solar wind and transported out with it into interplanetary space (Gurnett and Bhattachajee, 2005). This property that the magnetic field lines move with the plasma is known as the Alfvén frozen-flux theorem or the “frozen in theorem”. The solar wind flows out from the Sun in an approximately radial direction, however, as the Sun rotates the solar wind source region rotates along with it. The rotation of the source region causes sequential “parcels” of solar wind to flow out radially in a slightly angular direction. According to the frozen in theorem, the magnetic field is embedded within the solar wind but is also anchored in the solar wind source region. As the source region

rotates and the parcels flow radially away from Sun, the magnetic field is also forced into a spiral configuration, linking these individual parcels to the source region on the Sun. This spiral configuration of solar wind first envisaged by Parker (1958) and known as the Parker Spiral configuration is depicted in Figure 1.1.

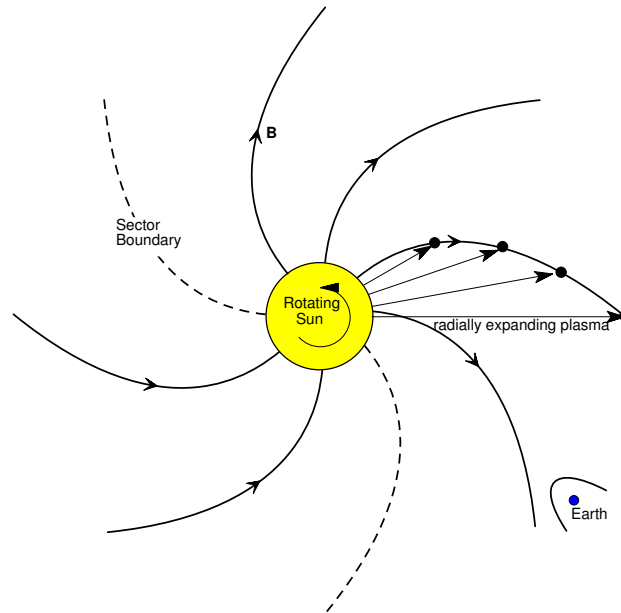


Figure 1.1: A schematic diagram illustrating how the rotation of the solar wind source region creates a Parker Spiral configuration due to the frozen in theorem. Figure downloaded from <http://how.gi.alaska.edu/ao/msp/chapters/chapter6.pdf>.

1.2 The Earth's Magnetosphere

While the dipolar magnetic field of the Earth has been known for many years, the fact that it was hit by solar wind is a recent concept and was first proposed by Chapman and Ferraro (1931). The

two had realized that this electrically neutral gas (plasma) would be a perfect conductor of electricity. Therefore, when this conducting stream hit the Earth's magnetic dipole its magnetic field configuration was deflected. This can be described using the mirror field method, in which a conducting plane representing the solar wind is replaced by an image of the dipole located symmetrically with respect to the plane as shown in Figure 1.2a. This strong field of Earth creates a cavity in the solar wind which is called the Chapman-Ferraro cavity as shown in Figure 1.2b (Chapman and Ferraro, 1930). Gold (1959a) was the first to call this cavity a bullet-shaped plasma cavity, the magnetosphere, as depicted in Figure 1.2c. The magnetosphere contains various large-scale regions which vary in terms of the composition, energies, and densities of the plasmas that occupy them as shown in Figure 1.3.

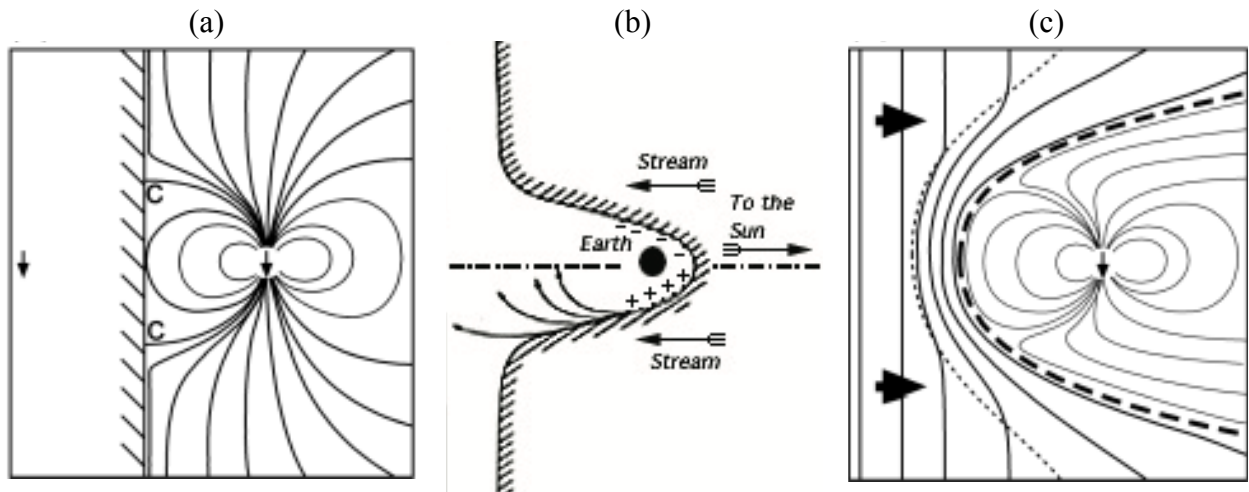


Figure 1.2: Chapman-Ferraro cavity and dipole and bullet shaped magnetosphere: (a) Disturbed dipole field geometry in the mirror method, (b) Chapman-Ferraro cavity, and (c) Formation of the bullet-shaped magnetosphere in the moving solar wind.

As the solar wind flow is supersonic, a shock wave is generated upstream of the Earth (the bow shock). At this shock, the solar wind speed is reduced to subsonic values in order to pass around the Earth. Consequently, plasma ‘piles up’, and the plasma density increases. Much of the bulk kinetic energy of the solar wind is converted to thermal energy, thus the temperature also increases across the shock. This region of shocked dense plasma of solar wind origin is called the magnetosheath. The magnetosheath plasma flows around the magnetosphere and the boundary between the magnetosheath and magnetosphere is called the magnetopause.

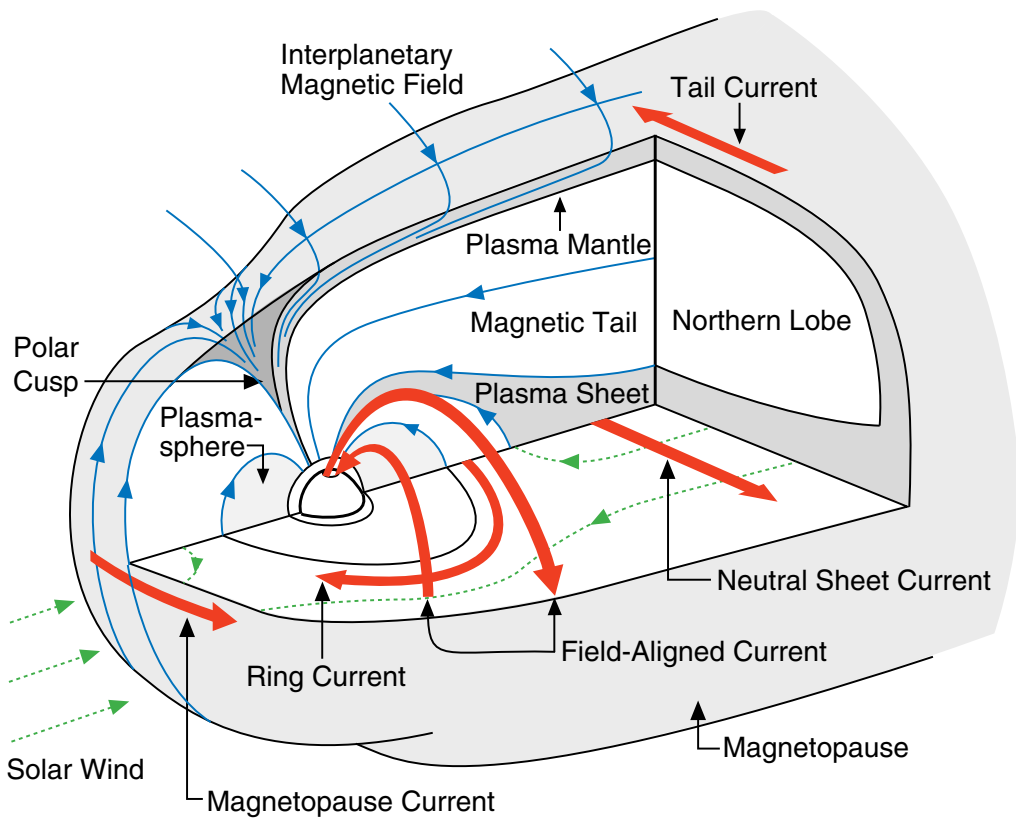


Figure 1.3: An illustration of Earth’s magnetosphere and currents (Crooker et al. 1999).

1.3 The Magnetopause

The magnetopause is a current layer shielding the Earth's magnetic field from the solar wind which was first proposed by Chapman and Ferraro as an intermittent boundary (1931a,b), and some years after was predicted to be a permanent feature of the magnetosphere (Dungey, 1954a). The simplest form of such a boundary is often called the Chapman-Ferraro current layer. The Chapman and Ferraro model correctly predicts the presence of a surface current on the boundary of the Earth's magnetosphere, the magnetopause. The existence of this current can be understood from the basic particle dynamics as shown in Figure 1.4. The figure shows a simple planar magnetopause boundary separating an un-magnetized solar wind from a magnetosphere containing no plasma. The magnetopause current is carried by the collective action of the solar-wind particles, each of which performs a half gyration in the geomagnetic field before returning to the magnetosheath. Ions impinging on the magnetosphere have a larger gyro-radius than the electrons. Ions move opposite to the electrons in this boundary layer. This generates a surface current, which separates the magnetosheath from the magnetosphere. The most fundamental conclusion of Chapman and Ferraro was that a boundary would form between the solar wind and magnetosphere, and that the solar wind would essentially fail to penetrate the space near Earth. This is called a 'closed' magnetosphere by Chapman and Ferraro (1930). The real Magnetopause apparently isn't an ideal Chapman and Ferraro magnetopause. An ideal magnetopause Chapman-Ferraro or tangential discontinuity has no mass flow across the boundary, no energy flux, and no drag force. On the other hand, some

particles observed in the magnetosphere are from the solar wind. This suggests that particles penetrate into the magnetosphere across the magnetopause.

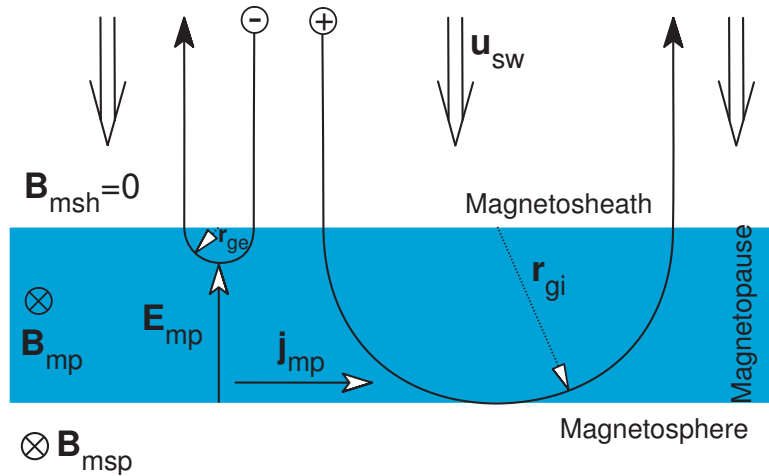


Figure 1.4: Illustration of particle dynamics at Chapman-Ferraro-Type. Figure downloaded from Magnetopause. <http://how.gi.alaska.edu/ao/msp/chapters/chapter8.pdf>.

1.4 Magnetopause Instabilities and Oscillations

The outer boundary of the Earth's magnetosphere, the magnetopause is constantly in motion and hence unstable. Understanding the mechanisms responsible for these motions and instabilities at the magnetopause boundary has been the topic of many papers in recent years (The importance of this topic lies in the fact that instabilities at the magnetopause control the transport of mass, momentum, and energy into the magnetosphere.

Numerous researchers have performed observational studies of magnetopause motions to check

various theories related to instabilities and to understand the origin of plasma transport at the magnetosphere boundary (Southwood, 1968; Kivelson and Chen, 1995; Lockwood, 1991). This transfer of plasma and momentum through the boundary is verified by the existence of the magnetotail (Freeman et al. 1968). However, there is no unanimous agreement about the exact physical mechanism involved in the plasma entry. Several mechanisms presumably contribute to these motions which are well correlated with conditions in the solar wind and can be divided into three distinct driving mechanisms: oscillations driven by variations in the solar wind dynamic pressure and magnetosheath (Sibeck et al. 1990,1991), intrinsic instabilities of the boundary layer such as the Kelvin-Helmholtz (KH) instability driven by the strong velocity shear at the dawn and dusk magnetopause (Southwood, 1968; Walker, 1981; Wu, 1986), and reconnection-related phenomena or Flux Transfer Events (FTEs) which are oscillations driven by the large magnetic shear between the geomagnetic field and the interplanetary magnetic field (Song et al. 1988). Among these mechanisms, magnetic reconnection and KH instability are considered to be two of the most important mechanisms for plasma transport across the Earth's magnetospheric boundary layer. Magnetic reconnection is considered to be the dominant process during southward interplanetary magnetic field (IMF), and KH instability has been suggested to play an important role under northward IMF condition. In the subsequent sections the concept of reconnection and also the KH instability will be briefly discussed.

1.4.1 Magnetic Reconnection

Magnetic reconnection primarily means reconfiguration of two different magnetic field topologies in which plasma elements that are initially connected to one magnetic field become

attached to another magnetic field. The concept of magnetic reconnection was first proposed by Giovanelli (1947) to be the mechanism that breaks the frozen-in condition and causes heating and acceleration of plasma in solar flares. Fred Hoyle, a famous British astronomer, assigned Giovanelli's idea as a project to his graduate student James Dungey. Dungey studied oppositely directed magnetic field lines separated by a thin current sheet as shown in Figure 1.5(a). The ideal MHD magnetic induction equation can be derived by substituting the ideal Ohm's law Equation (1.1) into Faraday's law Equation (1.2) as shown in Equation (1.3). When a field obeys the magnetic induction equation, plasma remains "frozen" into the field.

$$\mathbf{E} + \frac{\mathbf{v} \times \mathbf{B}}{c} = 0 \quad (1.1)$$

$$\frac{\partial \mathbf{B}}{\partial t} = -\frac{1}{c} \nabla \times \mathbf{E} \quad (1.2)$$

$$\frac{\partial \mathbf{B}}{\partial t} = \nabla \times (\mathbf{v} \times \mathbf{B}) \quad (1.3)$$

In other words, the bulk plasma flow carries not only the particles but also the magnetic field \mathbf{B} along with it. This means two particles connected by a single magnetic field line at one time t would remain connected by the same field line at the later time $t + dt$. Therefore, this "frozen-in" condition prohibits any changes in magnetic field line topology. However, Dungey suggested that by introducing a finite resistivity into the ideal Ohm's Law equation (1.1) the topology of magnetic field lines would be able to change near a magnetic neutral point:

$$\mathbf{E} = -\frac{\mathbf{v} \times \mathbf{B}}{c} + \eta \mathbf{J} \quad (1.4)$$

This would enable magnetic field lines to cross-connect at the x-line in the center of Figure 1.5(b). The tension in the newly formed field lines would propel those field lines away from the x-line. Once outside of the dissipation region near the x-line, the frozen-in condition holds once again, and so the magnetic field drags plasma along with it downstream.

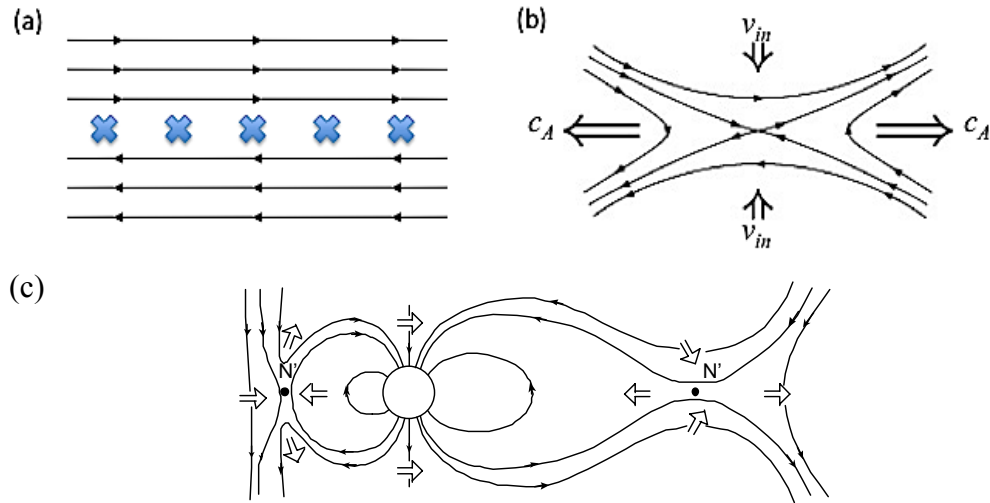


Figure 1.5: Topological structure of 2D reconnection (a), (b), and (c) Dungey’s reconnection model (1961): locations of magnetic reconnection at sub- solar magnetopause as well as in tail plasma sheet.

Dungey invented the term “magnetic reconnection” to describe this process. He proposed the two possible locations for magnetic reconnection in the magnetosphere: the sub- solar magnetopause and the tail plasma sheet as depicted in Figure 1.5(c). The primary consequence of this reconnection process is that the two plasma populations, which were originally on separate and isolated flux tubes, are now on the same flux tube and can easily mix.

1.4.2 Kelvin-Helmholtz Instability

Kelvin-Helmholtz instability is a fluid instability, which is applicable to plasma dynamic excited by a velocity shear (Chandrasekhar, 1961). It can be consider both hydrodynamics and hydro magnetic instability. The principle difference between hydrodynamics and hydro magnetic is the presence of the magnetic field, which can stabilize the instability when it lies parallel of the flow shear vector. Dungey (1955) proposed the idea that Kelvin-Helmholtz instability occurs at the magnetopause boundary. Soon after that, theoretical attempts to describe the instability at the magnetopause boundary were followed (Parker, 1963; Sen, 1963; Fejer, 1964; Southwood, 1968; Kivelson and Pu, 1984). These early works resulted in necessary conditions for the onset of the KH instability at the magnetopause boundary, which is valid for incompressible plasmas separated by a tangential discontinuity (Hasegawa, 1975), which will be discussed in the next section.

1.4.2.1 Theoretical view

The linear dispersion relation for KH instability for the most ideal case is derived in this section. A smooth boundary in MHD scale and incompressible plasma perturbations are assumed (Hasegawa, 1975). Assuming δx is a small displacement from equilibrium then the velocity of perturbation of plasma fluid from equilibrium can be defined as $\delta \mathbf{V} = d\delta x/dt$. The strategy is to linearize the induction equation (1.3) and momentum equation (1.5) and find an expression for displacement δx .

$$\frac{m_i n_0 \partial V}{\partial t} = -\nabla P - \frac{1}{\mu_0 \mathbf{B}} \times (\nabla \times \mathbf{B}) \quad (1.5)$$

The linearized induction equation is

$$\delta \mathbf{B} = \nabla \times (\delta \mathbf{x} \times \mathbf{B}_0) = \mathbf{B}_0 \cdot \nabla \delta \mathbf{x} - \delta \mathbf{x} \cdot \nabla \mathbf{B}_0 - \mathbf{B}_0 \nabla \cdot \delta \mathbf{x} \quad (1.6)$$

Where it has been integrated with respect to t. The linearized momentum equation is

$$\mu_0 m_i n_0 d^2 \delta \mathbf{x} / dt^2 = -\mu_0 \nabla \delta p - \delta \mathbf{B} \times (\nabla \times \mathbf{B}_0) - \mathbf{B}_0 \times (\nabla \times \delta \mathbf{B}) \quad (1.7)$$

The first order variation in the total pressure is

$$\mu_0 \delta p_{tot} = \mu_0 \delta p + \mathbf{B}_0 \cdot \delta \mathbf{B} \quad (1.8)$$

By using standard vector operations and eliminating the magnetic field perturbation from Equation (1.7) and (1.8) and using Equation (1.6):

$$m_i n_0 \left[(\mathbf{v}_A \cdot \nabla)^2 - \frac{\partial^2}{\partial t^2} \right] \delta \mathbf{x} = \nabla \delta p_{tot} + \mathbf{C} \quad (1.9)$$

$$\mathbf{C} = (\mathbf{B}_0 \cdot \nabla) [(\delta \mathbf{x} \cdot \nabla) \mathbf{B}_0 + \mathbf{B}_0 (\nabla \cdot \delta \mathbf{x})] - (\delta \mathbf{B} \cdot \nabla) \mathbf{B}_0 \quad (1.10)$$

Where $\mathbf{v}_A = \mathbf{B}_0 / (\mu_0 m_i n_0)^{1/2}$ is the Alfvén velocity and the vector C contains the remaining terms. By taking the divergence of Equation (1.9) and assuming that $\nabla \cdot \mathbf{B} = 0$ and $\nabla \cdot \delta \mathbf{B} = 0$, another equation can be derived for the total pressure variation:

$$\nabla^2 \delta p_{\text{tot}} = -m_i \nabla \cdot (n_0 d^2 \delta x / dt^2) + 1/\mu_0 \nabla \times (\delta \mathbf{B} \cdot \nabla \mathbf{B}_0 + \mathbf{B}_0 \cdot \nabla \delta \mathbf{B}) \quad (1.11)$$

Now, by assuming that the plasma density and the magnetic flux density are uniform except at the boundary surface and that the perturbation can be regarded incompressible so that $\nabla \cdot \delta \mathbf{V} = \nabla \cdot \delta \mathbf{x} = 0$, the right hand side of Equation (1.11) vanishes. That derives the necessary wave equation for the pressure perturbation as a simple Laplace equation:

$$\nabla^2 \delta p_{\text{tot}} = 0 \quad (1.12)$$

Because this is a Laplace equation, if we assume a wave-like perturbation along the boundary surface, the solution exponentially decays away from the surface and is called a surface wave:

$$\delta p_{\text{tot}} = p_0 \exp(-k|y|) \exp[-i(\omega t - k_x x - k_z z)] \quad (1.13)$$

Where $k^2 = k_x^2 + k_z^2$. Let consider the boundary to be in the (x, z) plane and assume plane wave solutions for both δx and δp_{tot} with wave number $\mathbf{k} = k_x \mathbf{e}_x + k_z \mathbf{e}_z$ and frequency ω . Then, the plasma displacement δx corresponding to this pressure perturbation is derived from Equation (1.9). The quantity C in Equation (1.10) that represents the coupling between the surface wave and Alfvén wave vanishes in uniform plasma and δx then can be expressed as

$$\delta \mathbf{x} = \frac{\delta p_{\text{tot}}}{m_i n_0 [\omega^2 - (\mathbf{k} \cdot \mathbf{v}_A)^2]} \quad (1.14)$$

The boundary is considered as a tangential discontinuity, i.e. a boundary through which there is

no plasma flow and $B_n = 0$, but where V_t , B_t , n , and p may jump. Therefore, the boundary conditions are taken to be the continuity of total pressure δp_{tot} and of the normal component of displacement δx . The two sides of the boundary are considered by 1 and 2 and let the plasma stream with velocity V_0 in region 1 and let the fluid in region 2 be in rest. We should note that ω_1 is Doppler shifted with respect to ω_2 , $\omega_1 = \omega_2 - k \cdot v_0$. Because the total pressure $p + B^2 / 2\mu_0$ is continuous, the continuity of the normal component of the displacement yields the dispersion equation for the KH waves:

$$\frac{1}{n_{02}[\omega^2 - (\mathbf{k} \cdot \mathbf{v}_{A2})^2]} + \frac{1}{n_{01}[(\omega - \mathbf{k} \cdot \mathbf{V}_0)^2 - (\mathbf{k} \cdot \mathbf{v}_{A1})^2]} = 0 \quad (1.15)$$

This equation is quite similar to the equation for hydrodynamic instability but instead of plasma oscillations the unstable modes are Alfvén waves. The dispersion equation has an unstable solution:

$$\omega = \frac{n_{01} \mathbf{V}_0 \cdot \mathbf{k}}{n_{01} + n_{02}} \pm i \sqrt{\frac{(n_{01} + n_{02})[n_{01}(\mathbf{V}_{A1} \cdot \mathbf{k})^2 + n_{02}(\mathbf{V}_{A2} \cdot \mathbf{k})^2] - n_{01}n_{02}(\mathbf{V} \cdot \mathbf{k})^2}{n_{01} + n_{02}}} \quad (1.16)$$

The real root for ω is

$$\omega_{kh} = \frac{n_{01} \mathbf{k} \cdot \mathbf{V}_0}{n_{01} + n_{02}} \quad (1.17)$$

Corresponding to the complex root for ω

$$(\mathbf{k} \cdot \mathbf{V}_0)^2 > \frac{n_{01} + n_{02}}{n_{01}n_{02}} [n_{01}(\mathbf{k} \cdot \mathbf{V}_{A1})^2 + n_{02}(\mathbf{k} \cdot \mathbf{V}_{A2})^2] \quad (1.18)$$

The KH instability occurs thus for sufficiently large V_0 . For small V_0 , and perpendicular magnetic field \mathbf{k} would have to be too large, i.e., the wavelength too short for the MHD description to be valid. This is for MHD fluid and it is ideal, incompressible, and with an isotropic pressure. The first term in Equation (1.18) represents the destabilizing effect by the velocity shears between the two sides of the boundary, while the second and third term implies the stabilizing effect of the magnetic field on the fluid's movement. The stabilizing effect of the magnetic field as the result of a force is clear, which attempts to resist ripples in the magnetopause maintaining straight magnetic field lines. The growth rate of the vortices depends on the \mathbf{B} , \mathbf{k} , and ΔV relative direction. If \mathbf{B}_1 and \mathbf{B}_2 are perpendicular to \mathbf{k} , then the right-hand side vanishes and $(V_0 \cdot \mathbf{k})^2 > 0$. This implies that the boundary is unstable to an arbitrarily small shear across the boundary (Parks, 2004).

An incompressible KH model that assumes a tangential discontinuity (TD) at the boundary interface predicts a growth rate that is an increasing function of the wave number, \mathbf{k} . This implies that a continuum of wavelengths will be excited and the smallest wavelength disturbances will grow the fastest. This theoretical result contradicts the magnetopause surface wave observations where monochromatic waves with well-defined wavelengths are typically seen (Takahashi et al. 1991; Chen et al. 1993).

Since Equation (1.18) is only valid for incompressible plasmas separated by a tangential discontinuity, the next level of sophistication in KH models came from the effects of

compressibility and/or a boundary layer thickness. All the studies attempted to quantify the effects of compressibility and boundary layer thickness (Ong and Roderick, 1972; Walker, 1981; Pu and Kivelson, 1983a,b; Miura and Pritchett, 1982) have found that both compressibility and boundary layer thickness have stabilizing effect on KH waves growth.

1.4.2.2 Effect of boundary layer thickness

The importance of treating finite thickness of the shear layer was emphasized by Lerche (1966). He showed that the Hydromagnetic analysis of the KH instability of shear layers of zero thickness leads to an inconsistency. The stability criterion depends on the phase velocity of the various modes, and therefore the highest growth rate occurs for the shortest wavelength disturbances. However, for very short wavelength perturbations the thickness of the shear layer should be taken into account. Also, Satellite observations of magnetopause crossings revealed a thin, viscous boundary layer at the magnetopause, called the Low-Latitude Boundary Layer (LLBL) (Hones et al. 1972; Eastman et al. 1976). The existence of a thin boundary layer near the magnetopause confirmed that modeling the magnetopause, as a tangential discontinuity was inaccurate.

In this section we will discuss briefly the result of the study completed by Ong and Roderick (1972) who consider a shear layer of thickness $2d$ in the y - z plane of a Cartesian coordinate system as shown in 1.6. The layer separates two regions of infinitely conducting fluids. In these regions, the fluid and electromagnetic field properties are constant. The magnetic field is tangential to the layer and its variation is arbitrary. The fluid velocity has been transformed in a way such that the constant flow velocities in regions III and I are given by

positive and negative V_{0z} respectively. Its variation through the layer is assumed to be linear.

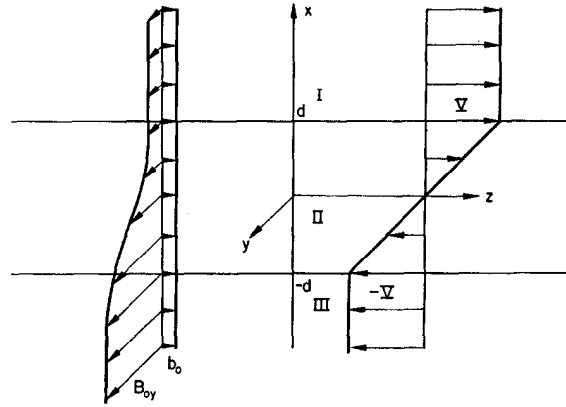


Figure 1.6: Shear Boundary layer Ong and Roderick (1972).

They started by linearizing the simple Laplace equation for the pressure perturbation across the boundary similar to Equation (1.12) but for three different regions including boundary thickness. In the equilibrium state the pressure balance across the layers is given by

$$\left(p_0 + \frac{B_0^2}{2\mu_0}\right)_I = \left(p_0 + \frac{B_0^2}{2\mu_0}\right)_{II} = \left(p_0 + \frac{B_0^2}{2\mu_0}\right)_{III} \quad (1.19)$$

The dispersion equation is calculated from a complete set of ideal MHD and equation 1,19 analytically, but the roots ω (the complex frequency), had to be evaluated numerically. The typical growth rate Υ versus the dimensionless wave number κ is shown in Figure 1.7. The growth rate curves shown are for a relatively large value of A , the Alfvén Mach number, based on the parallel component of the magnetic field. The well-known results for the case of a zero thickness shear layer are also shown for comparison. The results show the existence of a critical wave number κ_c , such that for $\kappa > \kappa_c$ the growth rate of the disturbance is zero. Furthermore, for

a shear layer of a certain thickness the parallel component of the magnetic field tends to stabilize the flow with respect to long wavelength disturbances. In summary, the finite thickness of the shear layer stabilizes the KH waves in regard to short wavelength perturbations. With respect to long wavelength disturbances, it limits the growth rate to finite values. A parallel magnetic field component b tends to stabilize the layer even further, yet it slightly extends the value of the critical wave number.

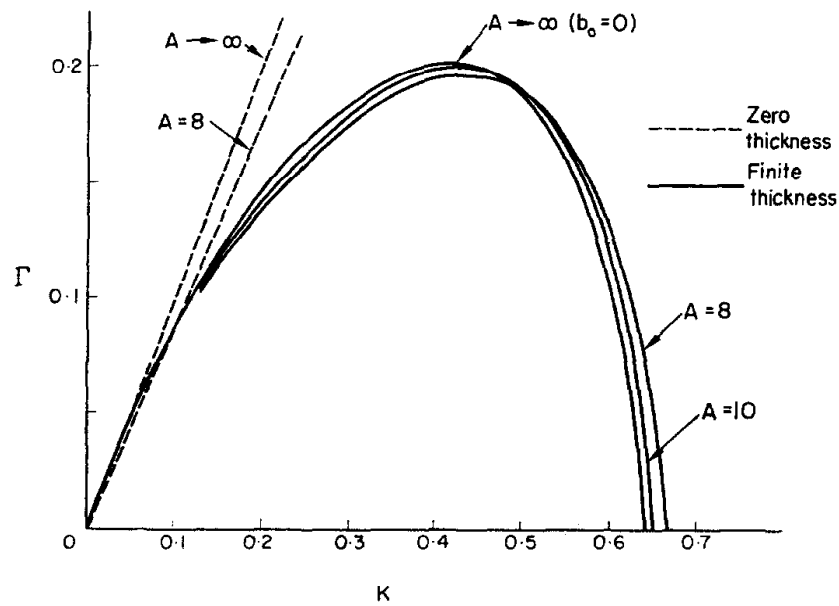


Figure 1.7: Growth rate versus wave number. Effect of the boundary layer thickness and parallel magnetic field. A is Alfvén Mach number from Ong and Roderick (1972).

1.4.2.3 Effect of compressibility

To solve Equation (1.19) in presence of compressibility (the density is variable), the full form of the continuity equation has been used. The adiabatic equation of state has also been used to complete the set of equations. The dispersion relation has been solved numerically by

Ong and Roderick (1972). The growth rate of the instability is shown in Figure 1.8 as a function of the dimensionless wave number k for a fixed value of M (Magneto sonic) Mach number. The result shows that the compressibility effects ($M=0.05$ and $M=0.1$) tend to lower the growth rate of the instability from that of the incompressible case ($M=0$), and it also reduces the value of the critical wavenumber k_c .

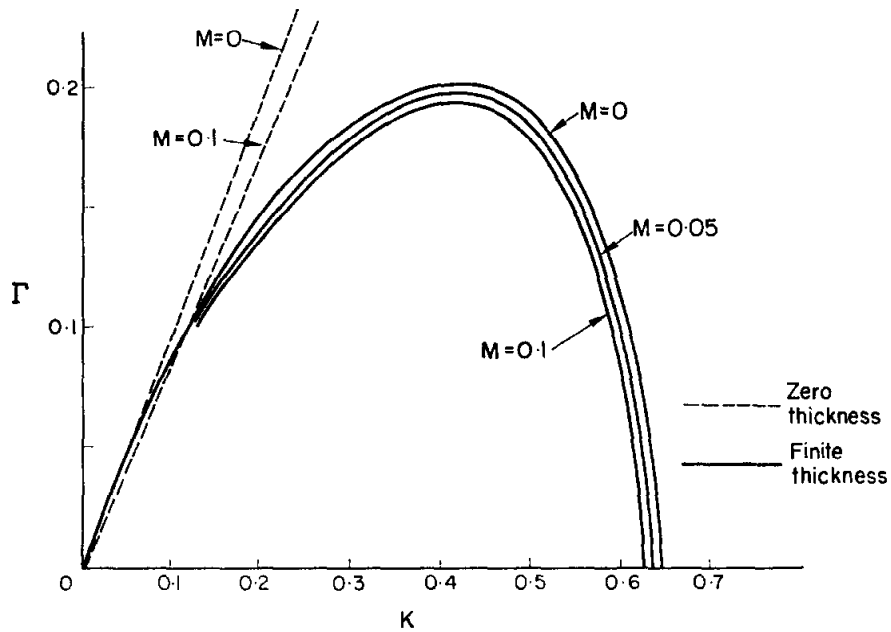


Figure 1.8: Growth rate versus wave number. Effect of the boundary layer thickness and compressibility. M is Magnetosonic Mach number from Ong and Roderick (1972).

The previous analysis of Ong and Roderick (1972) was restricted to the small compressibility with $M \ll 1$ which is not applicable in earth's magnetospheric boundary. Miura and Pritchett (1982) carry out the general stability analysis for sheared MHD flow of finite thickness in compressible plasma. They use arbitrary orientations of the magnetic field B_0 , velocity flow v_0 , and wave vector k in the plane perpendicular to the velocity gradient with no

restrictions on the sound or Alfvén Mach numbers. Therefore, the results of this general analysis is more realistic to discuss the stability of sheared plasma flow in astrophysical situations such as the solar wind flow at the earth's magnetospheric boundary. Here we will discuss briefly some of the key points of their results by discussing dispersion curves for the growth rates shown in Figure 1.9.

Figure 1.9 shows the growth rate for the transverse case as a function of wave number for different flow speeds. The growth rate is normalized in terms of $V_0/2a$, and the wave number is normalized by the shear scale length $2a$. Dashed line represents for incompressible flow with a shear layer of zero thickness and the uppermost solid curve represents incompressible case ($M_f = 0$) with finite thickness. The growth rate for the incompressible case reaches a maximum for $2k_y a \sim 0.9$ and reaching zero for $k_y a = 1$. As the Mach number M_f increases from zero and the compressibility becomes important the normalized growth rate is reduced considerably. In addition, the wave number of the fastest growing mode, k_{ym} , and the critical wave number, k_{yc} , are shifted toward smaller values. This behavior of k_{ym} and k_{yc} is consistent with the results obtained by Ong and Roderick (1972) in the small compressibility limit ($M_f \ll 1$). When $M_f > 2$, the shear layer is no longer unstable. Therefore, the substantial part of the dayside magnetopause should be unstable to the KH instability except near the stagnation point of the solar wind flow where the velocity is not large enough to overcome the stabilizing effect of the magnetic field line tension and the far downstream boundary, where the magnetosonic Mach number is much larger than one. Moreover, the figure shows for a wide range of Mach numbers, the fastest growing mode occurs at $k_y \Delta = 0.5-1$. The figure also shows that decreasing magnetosonic Mach number leads the growth rate to increase. Decreasing magnetosonic Mach number implies that

perpendicular magnetic field magnitude increases. Therefore, the perpendicular magnetic field has a destabilizing effect.

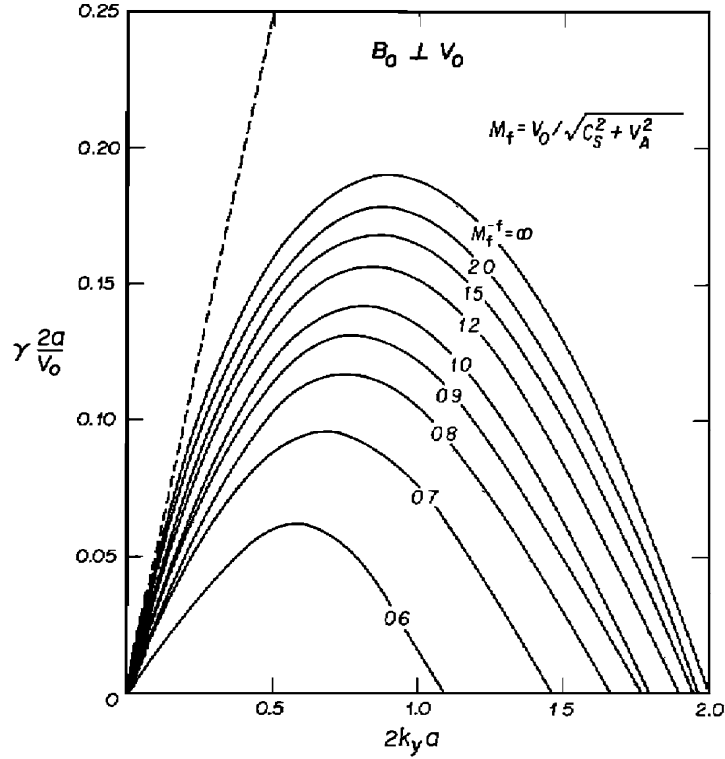


Figure 1.9: Normalized growth rate for KH instability with flow perpendicular to magnetic field. Maximum growth occurs when, $k_y \Delta \sim 0.5 - 1$, where k_y is the wave-vector along the flow direction and $\Delta = 2a$ is the width of the shear layer from Miura and Pritchett (1982).

In the magnetosphere, the compressible effects cannot be ignored at the low-latitude boundary layer region because the plasma β can be near unity (Fairfield, 1979). Moreover, the compressibility has a stabilizing effect on the instability when the relative shear flow speed sufficiently exceeds the magnetosonic speed. Thus a compressible MHD approximation is needed to describe the solar wind plasma within and out of the magnetosphere.

1.4.3 Ubiquity of Kelvin-Helmholtz Instability throughout Universe

Kelvin-Helmholtz waves are apparently everywhere, from our sky to solar system as shown in Figure 1.10. There have been many observations evidencing the existence of KH waves in our universe from the breaking wave patterns made in clouds (Figure 1.10d), the ocean's surface, our earth's magnetopause, to the swirling atmosphere of Jupiter (Figure 1.10b). KH instability in its MHD form is believed to be important in a variety of space and astrophysical contexts: At the magnetopause of Saturn (Masters et al. 2009) as shown in (Figure 1.10c), Jupiter's red spot (McComas and Bagenal, 2008), waves at the Earth's flank magnetopause (Fairfield et al. 2000, 2003; Hasegawa et al. 2004b, 2006), the leading and trailing edges of high-speed solar wind streams (Neugebauer and Buti, 1990), auroral arcs (Asamura et al. 2009; Chaston and Seki, 2010), the Heliopause boundary (Wang and Belcher, 1998), at the magnetopause of Mercury (Slavin et al. 2008; Boardsen et al. 2010), and around unmagnetized planets, for example at the Ionopause of Venus (Pope et al. 2009) and in the induced magnetosphere of Mars (Gunell et al. 2008).

The KH instability is also considered to play important roles in many solar physical systems, such as at a surface of a coronal mass ejection (Nykyri and Foullon, 2013) as shown in (Figure 1.10a), in the pulsar wind (Bucciantini et al. 2005), and in various astrophysical jets (Lobanov and Zensus, 2001). These observations have shown that this instability plays a key role in the solar wind interaction with many of the planetary environments.

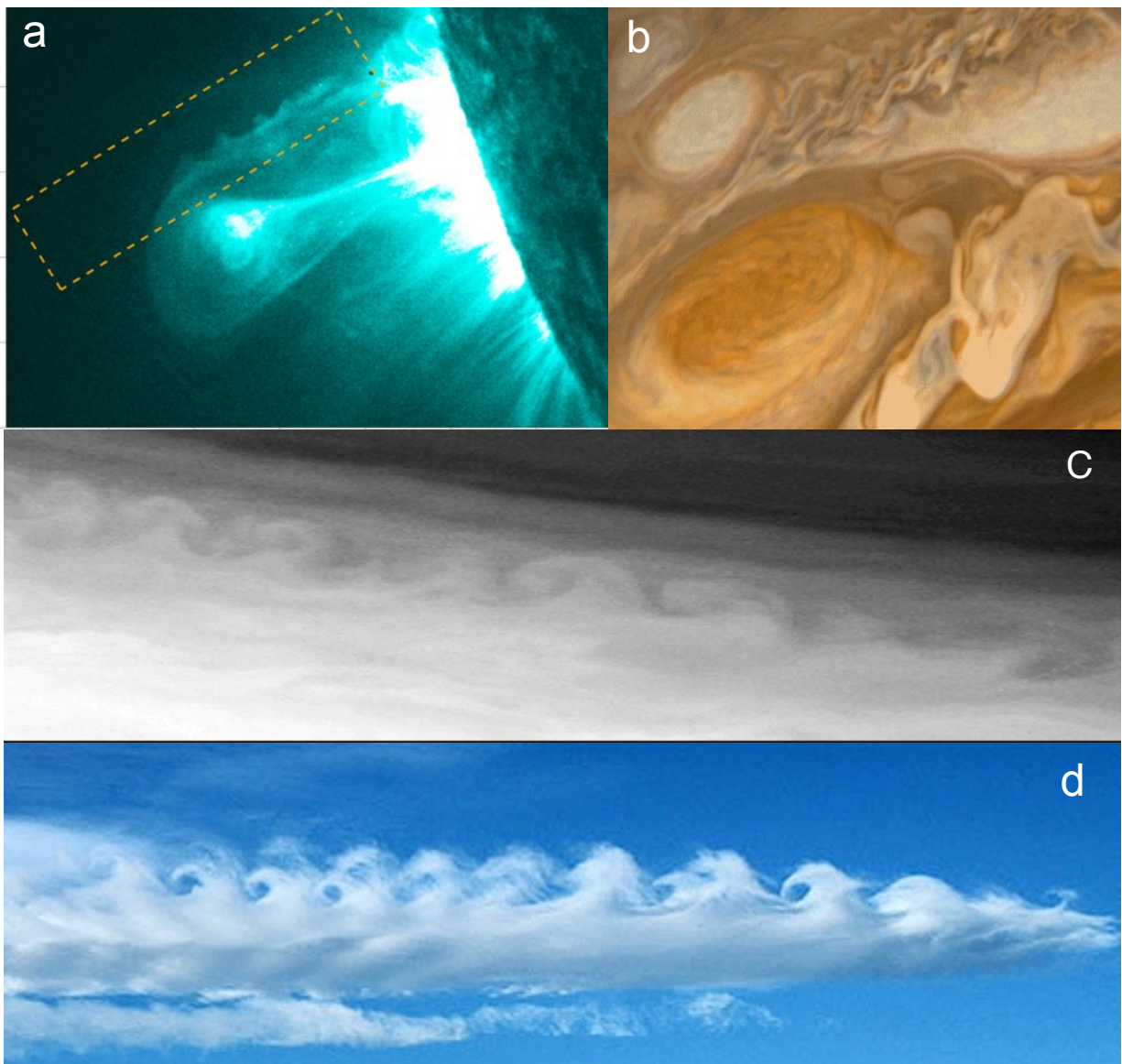


Figure 1.10: (a) KH waves observed at Sun. (b) observed at atmosphere of Jupiter (c) observed at Saturn (d) breaking wave pattern made in clouds.

1.5 Outline of Thesis

The main focus of this thesis is the observational statistical study of magnetopause crossings looking for KH wave signatures through the entire THEMIS mission.

Chapter 2 describes in detail the criteria, which we have used to identify the KH events at the flank magnetopause as well as our methods of distinguishing them from other possible mechanisms such as FTEs.

Chapter 3 presents the statistical results from our seven years of THEMIS (2007-2013) magnetopause crossings and KH database. A part of this chapter is published in Nature Commn (Kavosi and Raeder, 2015).

In Chapter 4, results of Global MHD simulation of KH instability using Open Geospace General Circulation (OpenGGCM) model is presented. The first part of this chapter presents the results of OpenGGCM simulation from constant solar wind input and the second part presents OpenGGCM simulation of a KH event observed by THEMIS.

Finally, Chapter 5 concludes the thesis by summarizing the most important conclusions and their potential applications to future missions.

Chapter 2

Kelvin-Helmholtz vortices at Earth's Magnetopause

2.1 Introduction

Kelvin-Helmholtz waves grow along a velocity shear layer on the flank magnetopause and eventually develop to nonlinear rolled up vortices (Fairfield, 2000) as shown in Figure 2.1. KH waves at the magnetopause can significantly change the energy levels of Earth's radiation belts (Elkington, 2006). The KH waves also can stimulate magnetospheric ultra-low frequency waves and transfer energy into the magnetosphere (Walker, 1981; Rae et al. 2005). To better understand how they have an impact on the radiation belt, excite the ULF waves, and transfer mass and energy into the magnetosphere, we need to rely on spacecraft data. The observational data provide the necessary facts to address these key questions. The identification of rolled-up vortices by in-situ measurements is therefore an important task towards establishing the mechanisms by which solar wind plasmas enter the magnetosphere, and to understand the conditions under which the vortices form.

In the first part of this chapter we review the numerical and observational studies, which have been done on detections, properties, and behavior on KH vortices at the magnetopause. Then we give a brief review on mechanisms by which energy and plasma transfer via KH vortices into the magnetosphere.

In the second part of this chapter we focus on methodology to identify KH waves at the magnetopause from spacecraft observations. Also, how the waves can be distinguished from other possible phenomena that oscillate the magnetopause such as waves driven by solar wind fluctuations and Flux Transfer Events (FTEs). This chapter also includes several examples of THEMIS observations of KH waves and FTEs at the magnetopause. All the examples presented in this section can be found in the supplementary materials of the author's recent paper (Kavosi and Raeder, 2015).

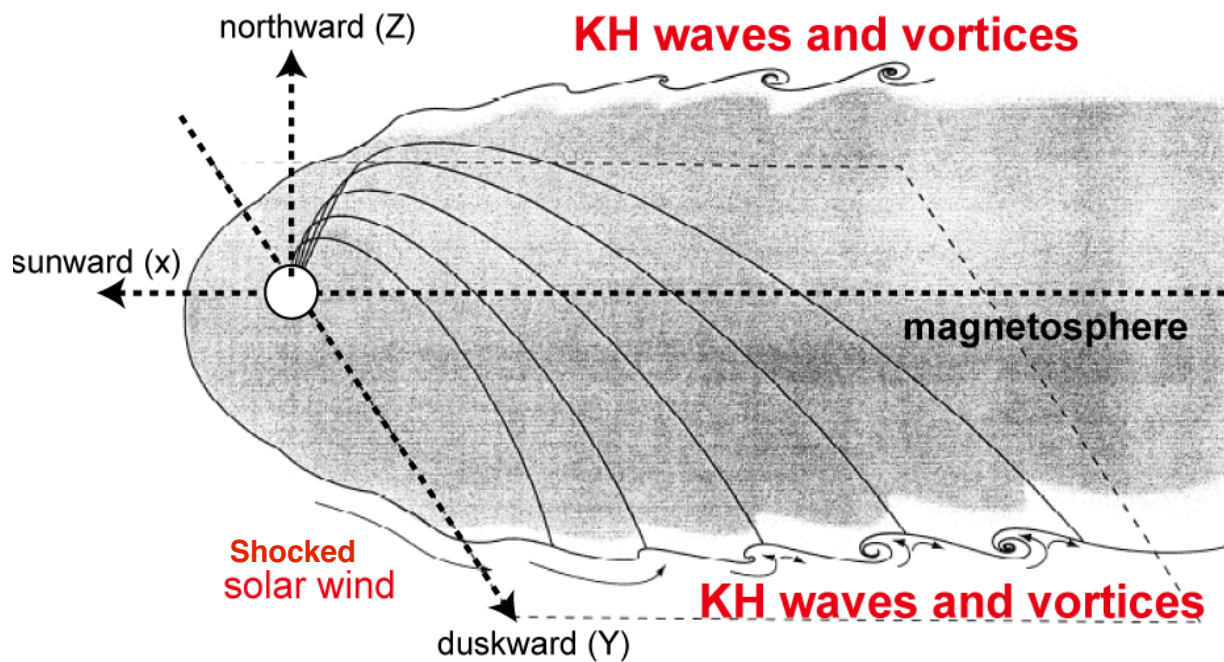


Figure 2.1: KH vortex at the Earth's magnetopause adapted (Fairfield, 2000).

2.2 Earlier studies: Simulations and Observations

The KH instability has been widely studied with several types of computer simulations all with their respective advantages: MHD (Miura and Pritchett, 1982; Miura, 1984, 1987, 1992; Otto and Fairfield, 2000; Nykyri and Otto, 2001; Matsumoto and Hoshino, 2004, 2006) and Hall-MHD (Huba, 1996), which are useful to study the instability on large spatial scales. Hybrid and kinetic codes, which are needed to resolve the small-scale behavior and to study the plasma transfer mechanisms (Umeda et al. 2010; Thomas et al. 1991,1993; Fujimoto and Terasawa, 1994; Nakamura et al. 2011, 2013). Also, various in-situ satellite observation signatures of the vortices have been found on the dusk and dawn flanks of the magnetosphere (Farrugia et al. 2000; Hasegawa et al. 2004; Hasegawa et al. 2006; Hwang et al. 2011).

Additionally, a combination of observations from single and multiple spacecraft with numerical simulations have frequently been used to explore and understand the KH instability (Takagi et al. 2006; Fairfield et al. 2007). Some studies explored the parameters favoring development of the instability, some focused on the properties and characteristics of the waves, and some addressed the plasma entry mechanism by the instability (Smet et al. 2002; Song and Russell, 1992) Ogilvie and Fitzenreiter (1989) used ISEE spacecraft observations in the magnetosheath, boundary layer to test instability criteria. Their results showed that the magnetopause is generally stable except for certain values of the k vector. Fairfield et al. (2000) used a Geotail observation of KH vortices under northward IMF condition. They showed nonlinear steepening of the waves on the leading edge of the wave rather than on the trailing edge consistent with MHD simulations of magnetic field fluctuations and plasma properties of

KH vortices reported by Otto and Fairfield (2000).

Hasegawa et al. (2004) employed multipoint Cluster observations to provide direct evidence for rolled-up vortices on the flank magnetopause during an interval of northward IMF. They interpreted the results as evidence for transport of plasma via vortices that formed in the magnetotail boundary layer. Hasegawa et al. (2006) showed that the rolled-up vortices are detectable even from single-spacecraft measurements by using this feature of vortices: The fraction of low-density, magnetospheric plasmas exceeds that of the magnetosheath flow. They searched for events consistent with the rolled-up vortices among 18 Geotail observations under northward IMF. They showed that such rolled-up vortices do occur on both dawn and dusk flanks and are not rare for northward IMF. Hasegawa et al. (2009) studied an event on 20 November 2001 of the equatorial magnetopause boundary layer simultaneously at ~1500 magnetic local time (MLT) by the Geotail spacecraft and at ~1900 MLT by the Cluster spacecraft. Cluster detected rolled-up vortices generated by the KH instability under northward interplanetary magnetic field conditions. The observed KH wavelength was longer than predicted by the linear theory from the thickness (~1000 km) of the dayside velocity shear layer. Their analyses suggested that combined effects of the formation of the LLBL presumably through high-latitude magnetopause reconnection and compressional magnetosheath fluctuations on the dayside facilitate the KH wave excitation. They reported an excitation of current sheet at the trailing edges of the vortices with signatures of local reconnection.

Fairfield et al. (2007) interpreted Geotail observations of magnetosheath magnetic field fluctuations during an inbound passage through the dusk equatorial region as evidence for KH

vortices in the boundary region. They ran a global MHD simulation, which reproduced the observed counterclockwise, polarized low frequency waves in the magnetic field and a region of high-velocity magnetosheath flow outside the magnetopause. Claudepierre et al. (2008) reported KH waves under purely southward IMF conditions using the LFM (Lyon-Fedder-Mobarry) global three-dimensional magnetohydrodynamic simulations (Lyon et al. 2004). They found two outer and inner KH modes propagating tailward along the magnetopause boundary. Hwang et al. (2011) presented the first in-situ observations of nonlinearly developed KH waves during southward IMF. Their analysis implied that the observed KH waves under southward IMF appear to be irregular and intermittent. These irregular and turbulent characteristics are more pronounced than previously reported KH wave events under northward IMF conditions. Farrugia and Gratton (2011) have shown that changes in the azimuthal velocity of the solar wind occurring at a discontinuity under a period of northward IMF excited large motions at the magnetopause. They reported that soon after the oscillatory character changed dramatically, higher frequency and smaller amplitude motions appeared. They argued the second oscillations to be magnetopause surface waves. And, by using the numerical simulation they found that the non-linear development of KH waves apparently speeded by the previous perturbations causing large vortical structures.

Recently, Yan et al. (2014) reported THEMIS observations of KH vortices at the dusk flank of magnetopause under southward IMF conditions. Lin et al. (2014) collected Fourteen THEMIS events with rolled-up vortices signatures under northward IMF at the LLBL, and 42 events from previously reported observations of the Geotail, Double Star TC-1, and Cluster. They performed a statistical study of the KH wave properties and explored the relationship

between the KH wave period, the solar wind velocity, and the IMF clock angle. They discovered that the KH period tends to be shorter under a higher and longer with a larger IMF clock angle. In general, the main objective of all these studies was to understand the plasma entry process within the KH vortex and the conditions, which favor for the mixing caused by vortices.

2.3 Mass and Energy Transfer within Vortices

The nonlinear stage of the KH wave, i.e. large-scale rolled-up KH vortices, facilitates solar wind entry into Earth's magnetosphere. How this entry may be activated by rolled-up vortices is still unclear. Several different mechanisms have been suggested to be responsible for transfer of mass and energy. First, diffusive transport through the turbulent decay of KH vortices whose onset has been attributed to a secondary KH instability or Rayleigh-Taylor instability (Matsumoto and Hoshino, 2004, 2006). Second, reconnection between stretched field lines due to the vortex motion (Otto and Fairfield, 2000; Nykyri and Otto, 2001; Otto and Nykyri, 2003; Nykyri et al. 2006; Nakamura et al. 2006, 2008). And third, kinetic Alfvén waves (KAWs) through a mode conversion from KH surface waves (Chaston et al., 2007). These processes can trigger plasma transport and mixing within or at the edge of rolled-up vortices. They are believed to play a crucial role in the evolution of the KH vortices structure and ultimately to form a broad mixing layer at Earth's dawn/dusk flanks.

2.3.1 Magnetic Reconnection

The KH instability in its nonlinear stage can develop small-scale filamentary field and current

structures at the flank boundaries of the magnetosphere. It has been shown previously with MHD simulations that magnetic reconnection can occur inside these narrow current layers, resulting in plasma transport from the solar wind into the magnetosphere.

Hu and Liu (1986) were the first to suggest the idea of vortex-induced reconnection. They stated, “ If there is a strong velocity shear in the space plasma sheath the KH instability is excited to produced large scale fluid vortices. The magnetic field lines are twisted within the vortices generating local reconnection’’. Later in the simulations performed by Otto and Fairfield (2000) and Nykyri and Otto (2001), the rolled-up structure of the KH waves was shown to be associated with a twisting of the magnetic field lines.

The simulation results reported by Nykyri and Otto (2001) showed that the vortex motion eventually starts forming sheaths of anti-parallel magnetic field lines shown in Figure 2.2. They reported that internal reconnection is enabled inside the vortex with the consequence that packets of plasma and magnetic flux are transported between the two domains. Similar observations have been made by Nakamura and Fujimoto (2005, 2006, 2008). Hasegawa et al. (2009) confirmed that the vortex-induced reconnection (VIR) commonly appears at the Earth’s magnetopause because magnetic shear (current sheet) always exists at the magnetopause.

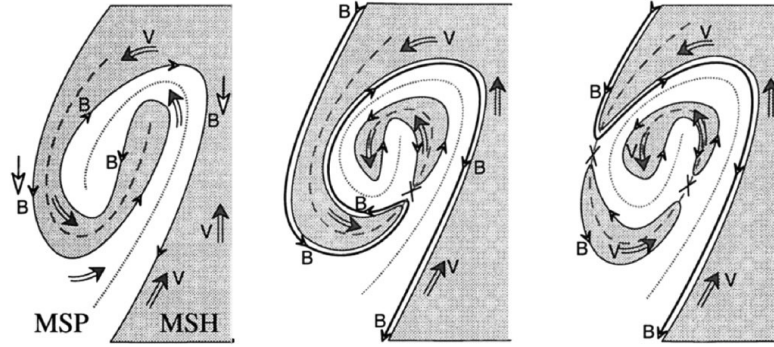


Figure 2.2: Schematic of reconnection in a K-H Vortex from Nykyri and Otto (2001).

2.3.2 Secondary Instabilities and Turbulence

Plasma mixing can also occur in the absence of reconnection. In the low latitude magnetopause context, another important secondary vortex instability is the Rayleigh Taylor (RT) instability (Matsumoto et al. 2004, 2006) which can develop inside the KH vortices and sometimes refer to vortex-induced Rayleigh-Taylor instability. As the vortex rolls up, the structure becomes highly disposed to turbulent flows and secondary instabilities (Nakamura et al. 2004). For example, as a consequence of the mass difference of the two regions and the centrifugal force exerted by the vortex motion, the boundary inside the rolled-up vortex becomes sensitive to the RT instability. This causes plasma transfer from dense to tenuous regions. The onset of secondary KH instability by the RT instability was reported by Sharp (1984). Secondary, short wavelength KH instabilities may develop at the boundary as well, which in turn leads to increased turbulence and additional RT instabilities (Matsumoto et al. 2004, 2006). Matsumoto et al. (2004) performed a two-dimensional MHD simulation of the KH instability in a non-uniform density medium. They showed turbulent mixing of plasmas by the KH instability as illustrated in Figure 2.3. Figure 2.3 shows in the nonlinear stage (Figure 2.3a) the secondary

instabilities start growing as shown in Figure 2.3b. Then, newly induced waves grow at the at the density interface at the outer edge and inside the normal K-H vortex. As a consequence of such developments of secondary instabilities, the normal vortex structure collapses and the system proceed to the turbulent flow stage (Figure 2.3c). In the final stage of the simulation run (Figure 2.3d) fine structures appear with turbulent flows and the mixing layer approaches the boundary.

Matsumoto et al. (2004) stated, “The onset of the turbulence is triggered not only by the secondary KH instability but also by the RT instability at the density interface inside the normal KH vortex. The secondary RT instability alters macroscopic structure by transporting dense fluids to the tenuous region, while the secondary KH instability is just a seed for the turbulence”. Matsumoto et al. (2006) compared the two-dimensional MHD simulations with full particle simulations of the KH instability with the transverse magnetic field. They found fast turbulent mixing and transport when there is a difference in density across the interface, which is triggered by secondary KH and RT instability. The strong electrostatic field caused by the secondary RT instability scatters ions and deforms the electron density interface and therefore the mixing area increases.

In summary, the large-scale vortex can lead to the secondary RT and Vortex Induced Reconnection (VIR) instabilities. These two secondary instabilities are primary mechanisms that cause mixing and turbulence within vortices. It should be noted that there is no clear distinction between the different mechanisms and they are all intimately coupled and partly describe similar effects from different perspectives.

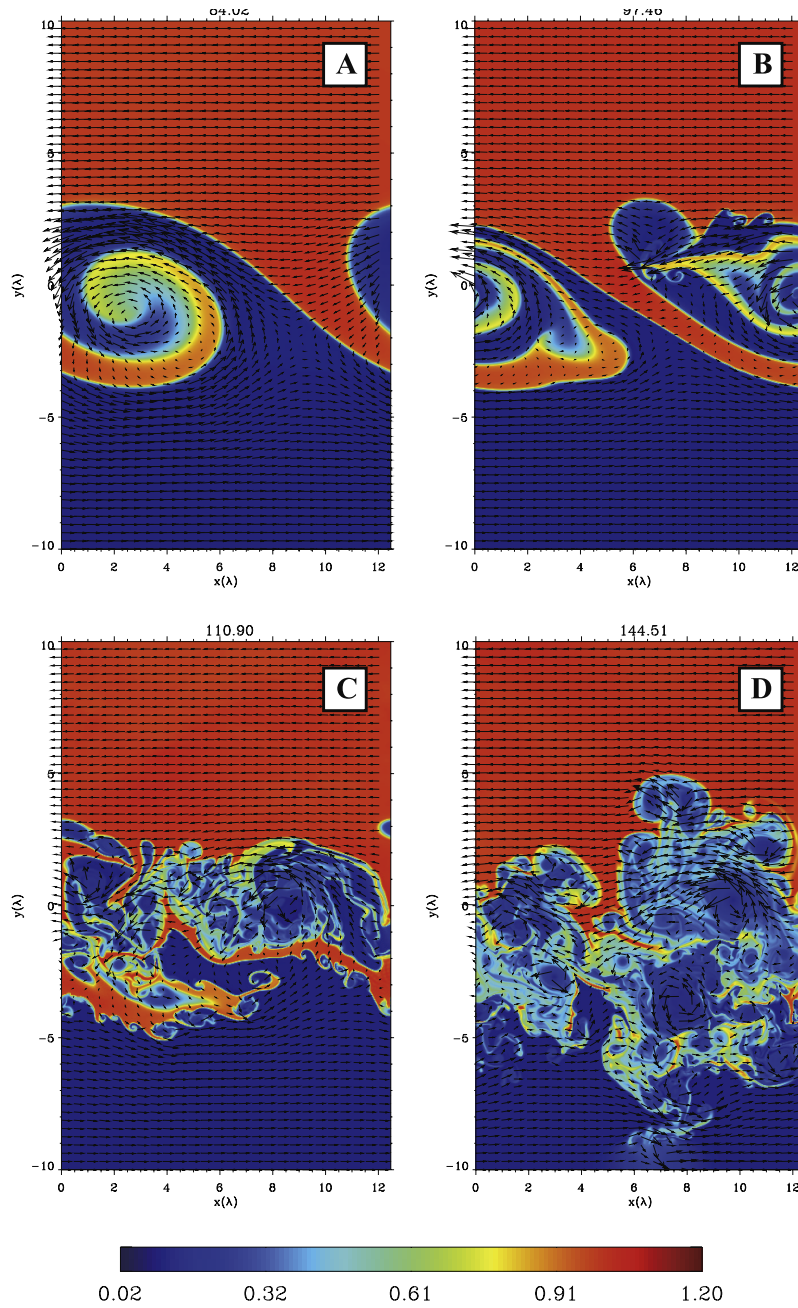


Figure 2.3: Number density profiles with flow vectors obtained by the ideal MHD simulation. The onset of secondary KH waves grow within the parent vortex is observed in Figure 2.2b. Turbulence is produced within the vortex in Figure 2.3c and Figure 2.3d. From Matsumoto, et al. (2004).

2.4 Kelvin-Helmholtz waves and Flux-Transfer Events (FTEs)

This section describes our methods to distinguish between FTEs and KH waves by providing a number of FTEs and KH wave examples observed by THEMIS. First, we describe the characteristics and signatures of FTEs and KH waves based on theoretical concepts and earlier observations. Second, we present examples of events from our data set to show how we differentiate between KH wave and FTEs. This section is part of the supplementary material provided for the author's recent paper (Kavosi and Raeder, 2015).

2.4.1 Flux Transfer Event identification

Flux Transfer Events (FTEs) are quasi-periodic reconnection events at the dayside magnetopause that produce flux ropes which subsequently move along the magnetopause flanks anti-sunward. The properties of FTEs are fairly well known, particularly the specific structure in magnetic field components, which is not present in KH waves (Southwood et al. 1988; Song et al. 1994). Russell and Elphic (1978) and Paschmann et al. (1982) identified the FTE phenomenon on the basis of certain distinctive features in plasma, magnetic field, and energetic particle data (Russell and Elphic, 1978; Lee and Fu, 1985). Russell and Elphic (1978, 1979) studied dayside low-latitude magnetopause crossings in magnetometer data from two of the ISEE mission satellites. They introduced boundary normal coordinates such that the unit vector \mathbf{N} was the outward pointing local magnetopause normal vector, \mathbf{L} lay parallel to the unperturbed

magnetospheric field (i.e. points approximately northward) and \mathbf{M} completed the right-handed set ($\mathbf{L} \times \mathbf{M} = \mathbf{N}$). This coordinate system revealed examples of a signature consisting of a bipolar variation in B_N with simultaneous variations of the components in B_L and B_M . The bipolar B_N signature was always in the same sense, positive then negative, subsequently termed a standard FTE (Rijnbeek et al. 1984,1987), and the B_L and B_M variations were not consistent with ordinary crossings of the magnetopause. The signatures were observed on both sides of the magnetopause. They concluded that these observations were signatures of reconnection and called them Flux Transfer Events (FTEs).

Figure 2.4 from Paschmann et al. (1982) and Elphic (1995) illustrates the magnetic field and plasma signatures in boundary normal coordinates (B_L , B_M , B_N) for magnetosheath and magnetosphere FTEs. There are four main classes: A, B, C, and D, which differ by the distance of the observing spacecraft from the magnetopause. Class A is the farthest from the magnetopause, and class D is the closest to the magnetopause. In class B, there is more evident energetic particle flux increase and B_N signature than in class A. Class B represents a full crossing of the flux tube. Class C is commonly known as the ‘crater’ FTE (Farrugia et al. 1988). The B_N signature is of larger amplitude than class A and class B, and there are often local minima in $|B|$ at one or both edges of the FTE (the ‘crater’). The taxonomy proposed by Paschmann et al. (1982) included only classes A, B, C classifications in magnetosheath FTEs. Elphic (1995) extended this taxonomy to equivalent magnetospheric events and added an additional class D of an FTE observed on the magnetopause itself. Class D corresponds to an FTE, which is observed at the same time as a magnetopause crossing.

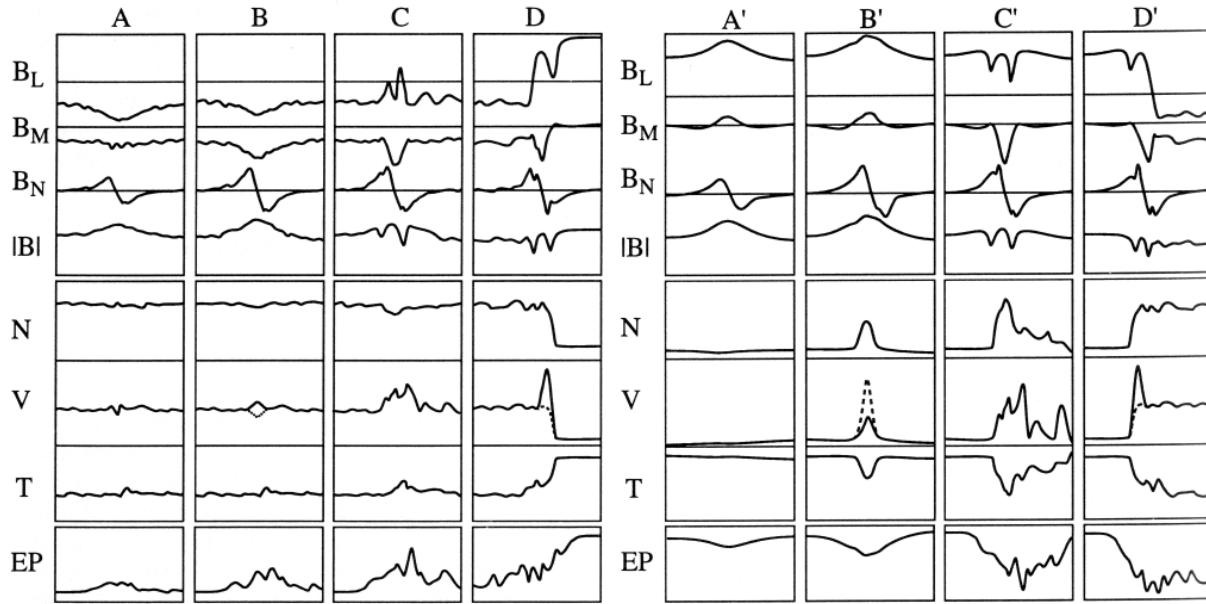


Figure 2.4: Taxonomy of magnetosheath (left) and magnetospheric (right) FTEs by Paschmann et al. (1982) and Elphic (1995). B is observed magnetic field, N is plasma density, V is bulk speed, T is temperature, and EP is energetic particle flux.

Rijnbeek et al. (1982) reported the first observations of reverse polarity FTEs. The bipolar B_N was reversed ($-/+$) compared to the $(+/-)$ standard polarity signature observed by Russell and Elphic (1978). The negative/positive B_N signature combined with the southward deviations in the plasma flow, and parallel flowing energetic magnetospheric particles led them to conclude that these FTEs were connected to the southern hemisphere.

In summary, the magnetic signature is the most important feature of a FTE in order to be detected by spacecraft measurements. These signatures include a distinctive bipolar signature in the component normal to the magnetopause surface (Roughly, the direct bipolar signature $(+/-)$ is found north of the equator, while the reverse bipolar $(-/+)$ is found south of the equator), either

enhancements or crater-like variations of the magnetic field strength at the event center, deflection in B_L and B_M , and the total pressure ($p_{\text{gas}} + B^2/2\mu_0$) maxima at the center of the event.

Table 2-1: Summary of FTE separation times

Reference	FTE characteristic times
Rijnbeek et al. (1984)	“The typical duration of FTEs was found to be ~1-2 min. FTEs observed in the magnetosheath and magnetosphere have similar recurrence times of “7 and “8 min, respectively.”
Elphic (1990)	"These disturbances (FTEs) are brief (1-2 minutes) and separated by a longer period of quiet (typically 6 - 9 minutes)."
Lockwood and Wild (1993)	"Magnetopause observation by the ISEE satellites shows that the distribution of the intervals between FTE signatures has a mode value of 3 min. The mean value is found to be 8 min."
Elphic (1995)	"In the case of FTEs possessing the requisite reconnection behavior the evidence points toward single x-line reconnection modulated at some characteristic (1-2 minute) time scale, with a recurrence interval of several times the modulation time scale (5-10 minutes)"
Kuo et al. (1995)	Obtained 10.5 min (median: 8 min) FTE separation time from their ISEE 1 FTE study.
Neudegg et al. (2000)	Using Equator-S data, found FTEs with an average FTE separation time of 8.8 min, assuming intervals larger than 20 min are not part of the same reconnection sequence.
Wang et al. (2005)	"We obtain an average FTE separation time of 7.09 min, which is at the lower end of the previous results."

Previous studies, which have been indicated in Table 2.1, have found that the typical duration of an FTE is about 1-2 minutes and the mean time interval between FTE signatures is of the order of a few minutes (Lockwood and Hapgood, 1998; Russell et al. 1996), which means one minute FTE and several minutes ambient field. Subsequently, by definition FTEs are signatures of bursty or time-dependent reconnection and do not occur right after each other. They are brief (~ 1 min) perturbations separated by a longer period of quiet time (no-perturbation), while KH waves are a continuous wave train. Table 2.1 summarizes the separation times of FTEs that have been proposed by different authors with references to the original publications.

2.4.2 Kelvin-Helmholtz Vortex identification

Not all B_N bipolar signatures are due to transient reconnection (FTEs). Solar wind pressure pulses and KH vortices can also explain the observation of a bipolar variation of magnetic field component normal to the magnetopause. The former only produces a single bipolar B_N event and are thus easily distinguishable from KH waves.

When a KH wave grows to the nonlinear stage it forms rolled-up vortices, as depicted in Figure 2.5. The development of such vortices has been demonstrated in many numerical simulations. In such vortices, the centrifugal force pushes plasma from the central part of the vortices radially out, thereby generating a local minimum in the total pressure at the center shown as “L” and a maximum at the hyperbolic point shown as “H” in Figure 2.5 between the vortices (Miura, 1997). Accordingly, it is expected that the spacecraft observes quasi-periodic oscillations in the density, total pressure, and N and M components of the velocity, and the approximate coincidence of total pressure maxima and density jumps from the magnetosphere to

the magnetosheath as depicted in Figure 2.6. Figure 2.6 shows KH vortices observed by Cluster from (Hasegawa, 2012). The Figure shows an example of nonlinear KH waves where the density jumps from magnetospheric to magnetosheath values closely coincide with total pressure maxima at the edges of the vortices.

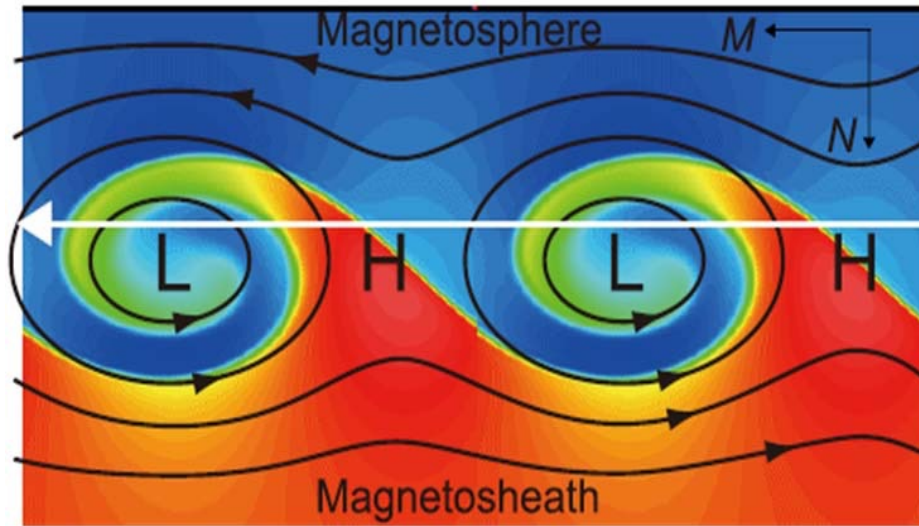


Figure 2.5: Schematic drawing of rolled-up KH vortices at the dusk-flank magnetopause. The relationship between the streamline pattern (black lines) and total (magnetic plus plasma) pressure and density (red, dense; blue, tenuous) distributions, when viewed in the vortex rest frame. The sub-solar region is to the left. The total pressure minimizes at the center (L) of the vortices, while it maximizes at the hyperbolic point (H), which is a flow stagnation point in the vortex rest frame, and around which the streamlines form hyperbolas (Miura, 1997). It is expected that magnetosphere-to-magnetosheath transitions be characterized by large and rapid density increases coincide with maxima in the total pressure (see example in Figure 2.6). From Hasegawa, (2012).

Fortunately, there is another distinct feature of KH waves in nonlinear stage: In a rolled-up KH vortex the magnetospheric plasma that extends into the magnetosheath and forms part of the breaking/overtaking wave becomes accelerated to speeds larger than the magnetosheath speed. This effect was first reported by Nakamura et al. (2004). Nakamura et al. (2004) and

Takagi et al. (2006) demonstrated in their simulations that at a certain radial distance from the center of a rolled-up vortex, the tenuous plasma sheet rotates faster than does the denser magnetosheath in response to an equal centrifugal force. Therefore, the low-density plasma flowing faster-than-magnetosheath plasma in V_x versus density N distribution is evidence of a rolled-up vortex. This theoretical argument has been verified by Hasegawa et al. (2006) who used in-situ data to show that only in the rolled-up vortices does the tailward speed of low-density, magnetospheric plasma exceed that of the magnetosheath. When the KH instability enters the nonlinear phase, at some distance from the vortex center, the centrifugal force must be nearly equal for both the denser magnetosheath plasma and the less dense magnetosphere plasma, because otherwise the vortex would break apart. Since the centrifugal force is proportional to ρv^2 the less dense part in the vortex rotates faster than the denser part. Such a behavior manifests itself as a very distinct signature when vortices rolled-up at the magnetopause and can be made visible by plotting V_x versus density in a scatterplot. Therefore, V_x versus density scatterplot exhibits a distinct pattern, depending on the phase of the KH instability growth (Takagi et al. 2006).

Figure 2.7 demonstrates this effect using a two-dimensional MHD simulation (adapted from Hasegawa et al. 2006). The top panel shows a significant fraction of low-density plasma ($N/N_0 < 0.5$) has an anti-sunward speed higher than that of the magnetosheath plasma a rolled up vortices. The middle panel shows low-density plasma ($N/N_0 < 0.5$) has an anti-sunward speed the same with the magnetosheath plasma and is not-yet-rolled-up. The bottom panel shows no low-density and high-speed plasma which means is in linear stage.

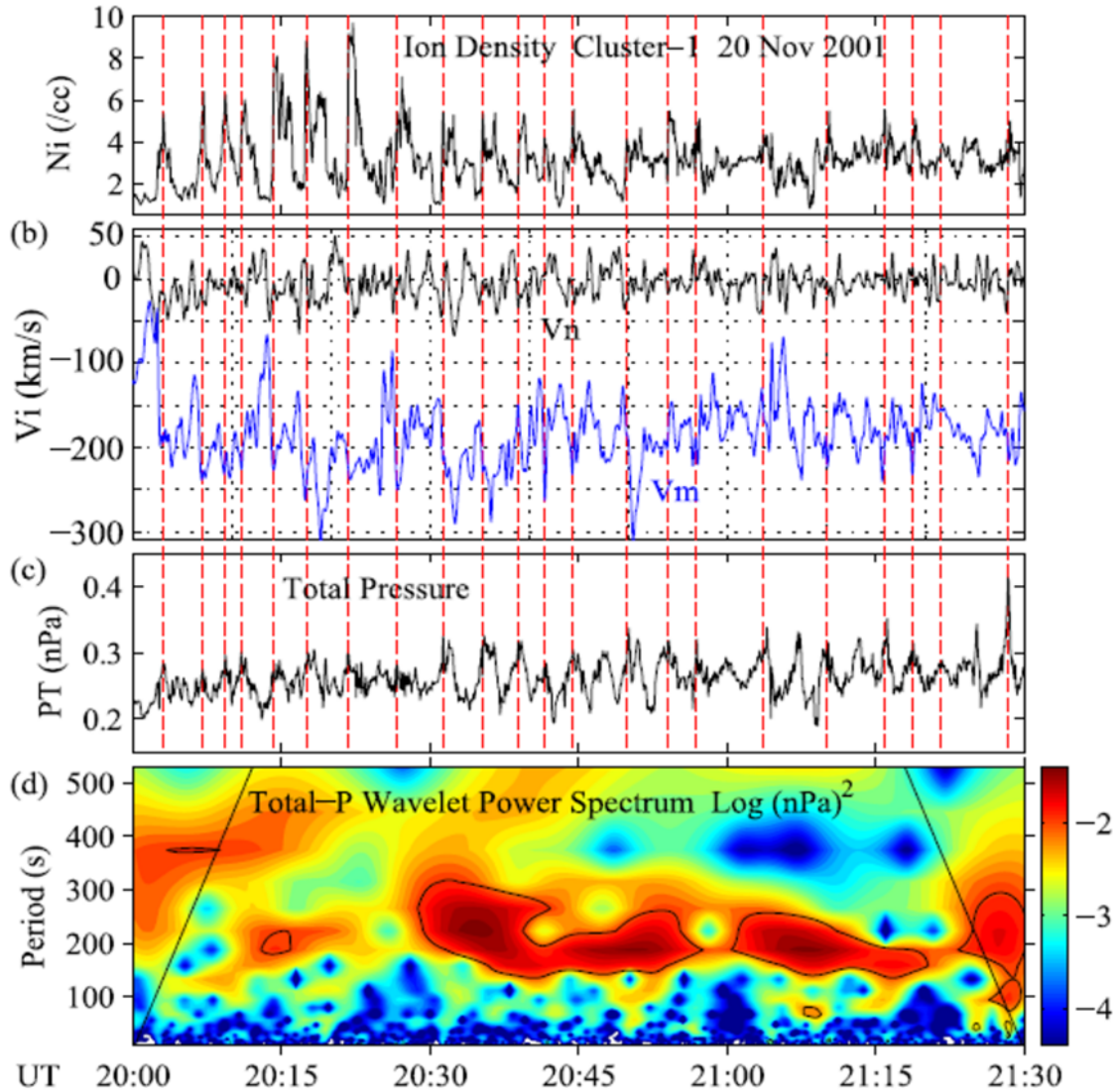


Figure 2.6: KH vortices observed by Cluster. Quasi-periodic fluctuations of the bulk plasma parameters during Cluster 1 (C1) observations of rolled-up KH vortices showing: (a) Ion density, (b) M and N components of the smoothed velocity (c) total pressure (magnetic plus ion pressure), and (d) wavelet spectra of the total pressure. Note that density jumps from the magnetospheric to magnetosheath values closely coincide with total pressure maxima (red vertical dashed lines), as expected in developed KH vortices and explained in Figure 2.5. From Hasegawa, (2012).

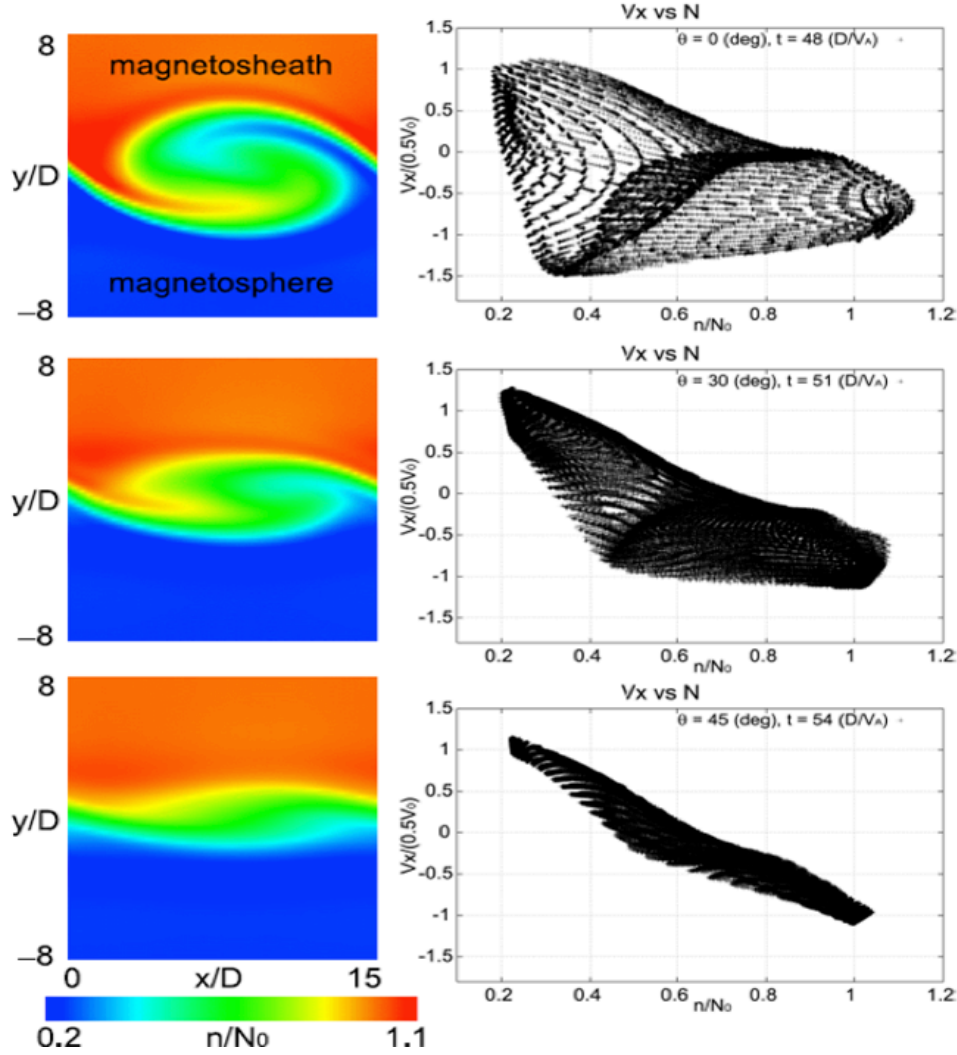


Figure 2.7: MHD simulation of KH waves. Plasma density (left column) and scatter plots of the x (sunward) component of the velocity V_x versus plasma density N/N_0 , at different stages of 3D MHD KH instability simulations generated from virtual spacecraft observations of the simulated KH wave or vortex. The left panels show the normalized density in the x - y plane in color. The initial values of V_x are -1 and $+1$ on the magnetosheath and on the magnetospheric side, respectively. Within the rolled-up vortex (top), a significant fraction of low-density plasma ($N/N_0 < 0.5$) has an anti-sunward speed higher than that of the magnetosheath plasma characterized by $V_x = -1$ and $N/N_0 = 1$. In the linear and not-yet-rolled-up stages (bottom two rows) no such relation exists (from Hasegawa et al. 2006).

2.5 THEMIS Observations of KH waves and FTEs

This section presents several examples of KH waves and FTEs observed by THEMIS. We then apply the KH waves and FTEs characteristics discussed in previous section to identify their signatures from in-situ data.

2.5.1 KH waves in linear stage on 01/13/2012

On 13 January 2012, THEMIS E observed quasi-periodic fluctuations at the dawn flank magnetopause during the interval 1640 - 1730 UT. The solar wind parameters are shown in Figure 2.8. The red vertical dashed lines show the event interval. Time delay between solar wind monitor, Geotail, and THEMIS E is approximately 30 minutes. The figure 2.8 shows some fluctuations in density and velocity, however, the frequency of the fluctuation is different from the oscillations observed by THEMIS E. THEMIS E was located at (8, -7.8, 3.0) Re at the GSM coordinate and was moving sunward. Figure 2.9 shows an example of a crossing where KH waves were present. THEMIS E observed continuous periodic fluctuations of the bulk plasma in density and N and M components of velocity and magnetic field parameters but no significant fluctuations in total pressure or magnetic field magnitude. Some of the crossings show B_N bipolar signatures and some do not. We therefore concluded that this wave train might be a KH wave in the linear stage that has not developed to a vortex yet. We then performed the V_x versus N scatterplot test shown in Figure 2.10. The figure confirms that there is no evidence for accelerated low-density plasma. Therefore, we concluded that the event present KH waves that is somewhere between the linear stage (bottom panel of Figure 2.7) and “not-yet developed” stage

similar to the plot depicted in the middle panel of Figure 2.7.

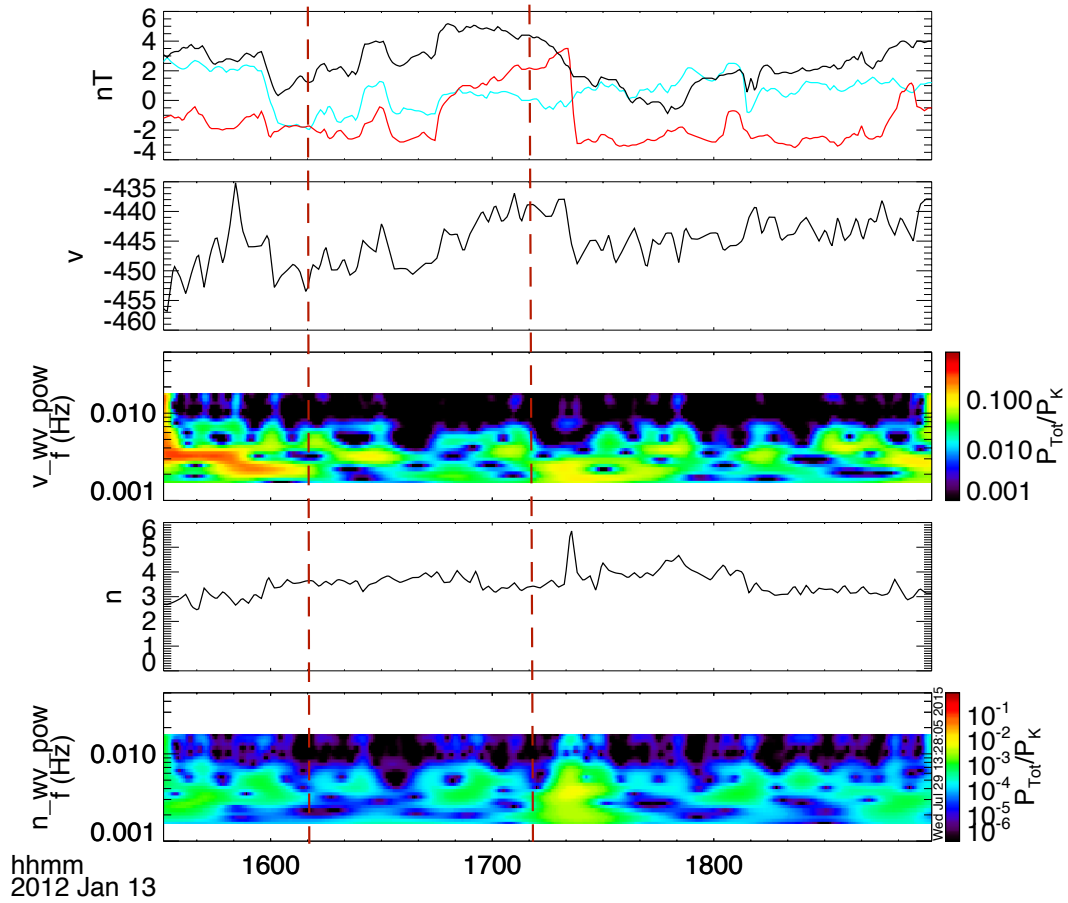


Figure 2.8: Geotail observation of solar wind parameters on 13 Jan 2012. From top to bottom: magnetic field components by (red), b_x (blue), b_z (black), X component of the velocity V_x , (c) wavelet spectrum of V_x , n density, and wavelet spectrum of the density, n . The red vertical lines shows the event interval. The frequency of oscillations in solar wind is ~ 0.004 Hz ($T \sim 250$ s).

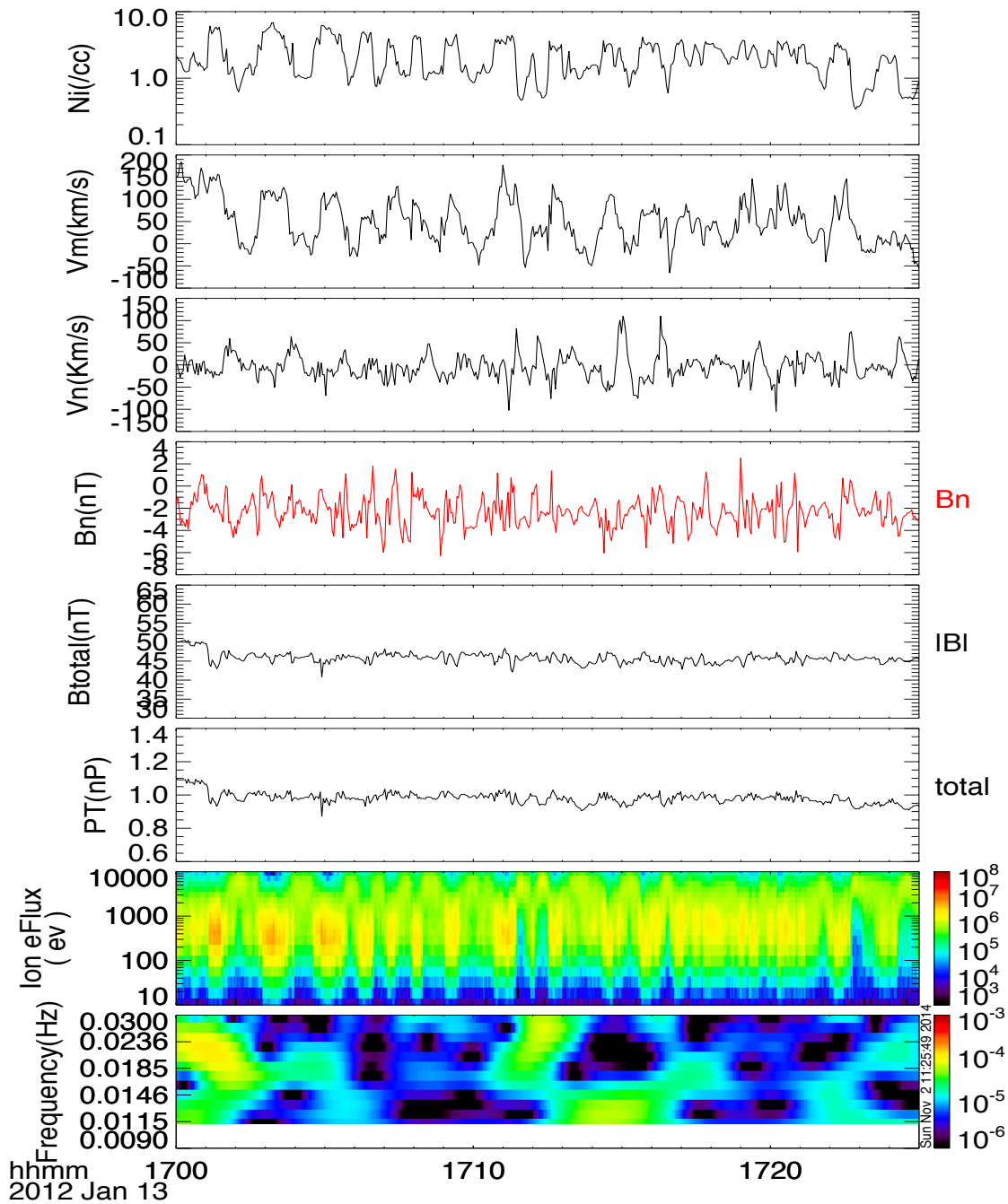


Figure 2.9: Time series data from THEMIS E on 13 Jan 2012. From top to bottom: (a) Ion density, (b) M component of the velocity V_m , (c) N components of the velocity V_n , (d) N component of magnetic field B_n , (e) Magnetic field magnitude B_{tot} , (f) total (magnetic plus ion) pressure, (g) Omnidirectional ion energy flux spectrogram, and (h) wavelet spectrum of the total pressure. The wave period is approximately 90 s.

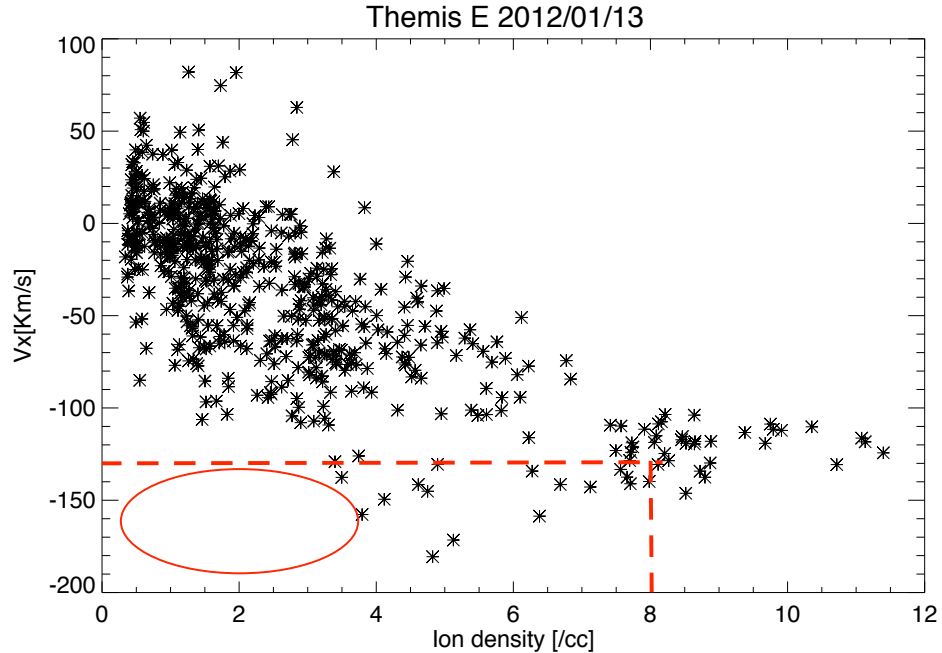


Figure 2.10: Scatter plot of the velocity component, V_x , tangential to the nominal magnetopause, versus ion density for the event shown in Figure 2.9. The $-X$ direction is roughly along the $-M$ direction, i.e., tangential to the magnetopause and anti- sunward. The plot confirms that there has no low-density plasma with anti-sunward speed higher than that of the magnetosheath plasma. The horizontal dashed line is the velocity of magnetosheath plasma and the red circle shows where we expect low density and high speed plasma. No particles depicted as black star in red circle indicates that the KH waves are in linear stage.

2.5.2 KH waves in nonlinear stage on 04/19/2008

On 19 April 2008, THEMIS C observed quasi-periodic fluctuations at dusk flank magnetopause during the interval 0500 - 0600 UT. We show the THEMIS magnetic field and velocity components in boundary normal coordinates (L, M, N). The solar wind had a flow speed 550 km/s, density $N = 5 \text{ cm}^{-3}$ and IMF vector of $(-1.5, 1, 2.5) \text{ nT}$. There were no significant solar wind dynamic pressure variations before or during the event. THEMIS C was located at $(-6.8, 18, -1.0) \text{ Re}$ and was moving anti-sunward. Figure 2.11 shows quasi-periodic fluctuations of the bulk

plasma and magnetic field parameters during the interval. The vertical red dashed lines demonstrate that the density and V_m (velocity in M direction) that jumps from the magnetosphere to magnetosheath values coincide with maxima of the total pressure. These loci correspond to the hyperbolic points ‘H’ depicted in Figure 2.5. Also, as discussed above, we expect the total pressure to minimize at the vortex centers, which is indeed the case in this event, evident from the total pressure minima halfway between the red lines. Furthermore, the bipolar B_n signatures are centered on the red lines, i.e. the ‘H’ points. This is consistent with Figure 2.5 schematic, which shows that the field lines should bend at those points with a vanishing B_n component.

Figure 2.12 shows V_x - N scatter plot generated from THEMIS C observations of the KH wave example presented in Figure 2.11. Concurrent THEMIS B observations in the magnetosheath showed plasma with ~ 350 km/s velocity and ~ 8 cm $^{-3}$ density. The figure shows that for part of the low-density (< 4 cm $^{-3}$) boundary layer ions, $|V_x|$ is larger than that of the high-density magnetosheath ions ($V_x \sim -350$ km/s), which is due to the vortex rotation. The result confirms that the event observed by THEMIS C on 04/19/2008 is KH rolled-up vortices.

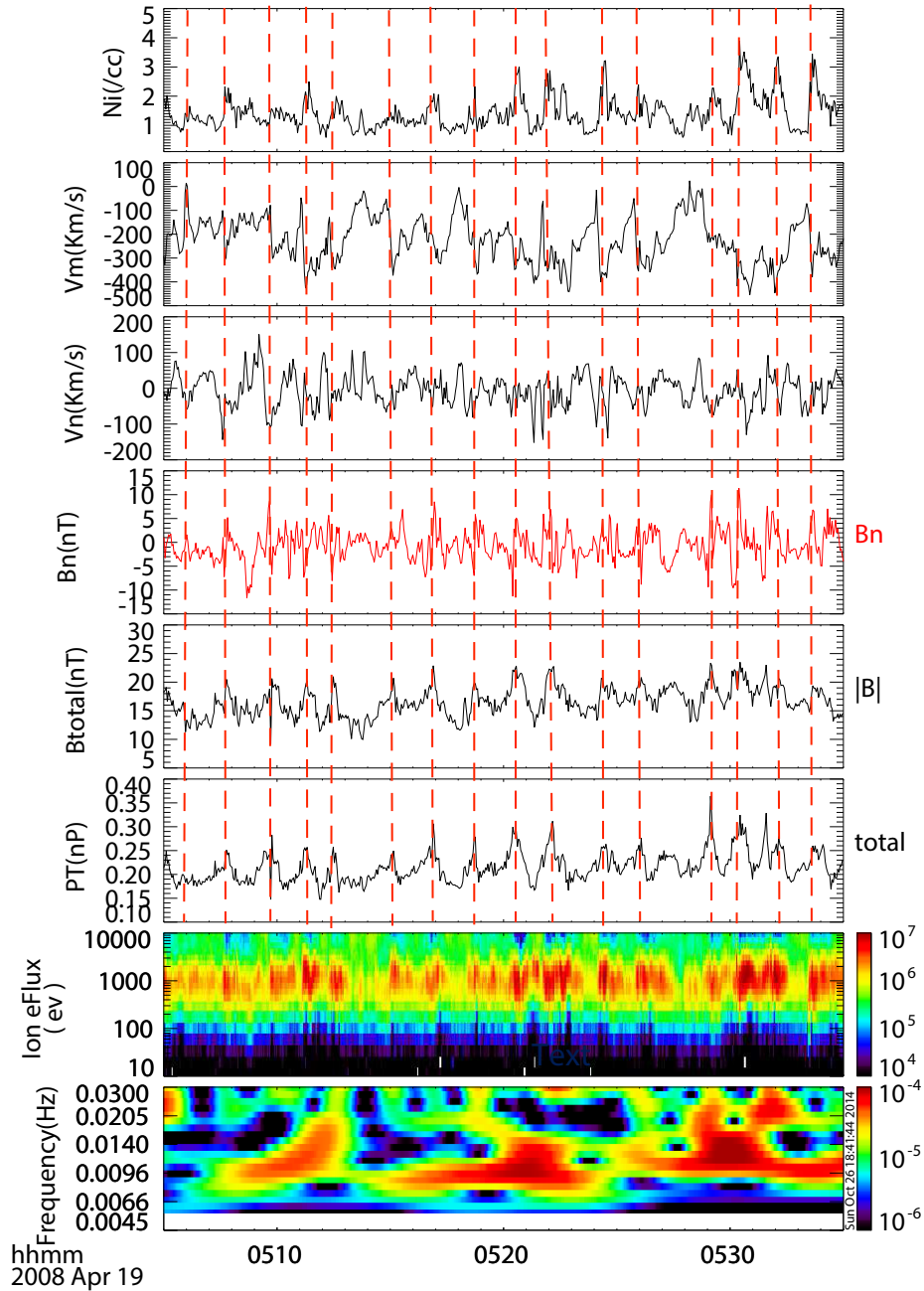


Figure 2.11: Time series of data for THEMIS C on 19 April 2008. Kelvin–Helmholtz waves observed at the dawn flank magnetopause by THEMIS C on 19 April 2008. The panels show, from top to bottom: (a) the ion number density, (b) the M component of ion velocity, (c) normal component of the ion velocity vector, (d) normal component of magnetic field, (e) total magnetic field, (f) total (magnetic plus ion) pressure, (g) omnidirectional ion energy spectrogram, and (h) wavelet spectra of the total pressure. The wave period is approximately 100 s.

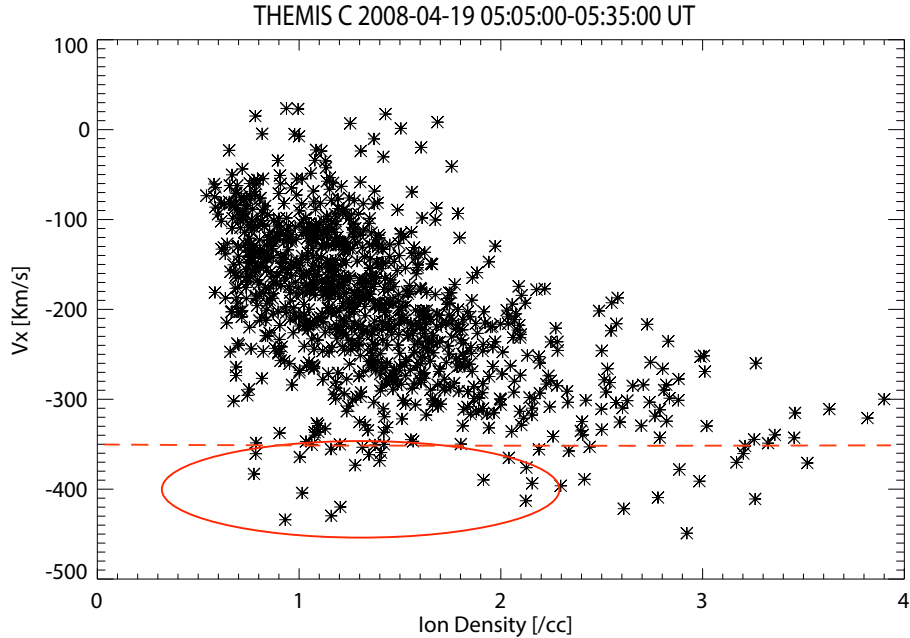


Figure 2.12: Scatter plot of the ion velocity V_x component versus ion density. The data are from THEMIS C for the 19 April 2008 event. Each symbol represents one of the samples, which were taken at 5 min cadence. Negative V_x values indicate anti-sunward flow. The plot confirms that this event consists of rolled-up KH vortices, because a fraction of the low-density magnetospheric plasma, indicated by the red ellipse, flows faster than the magnetosheath plasma ($> 350 \text{ km s}^{-1}$, shown by the dashed red line).

2.5.3 KH waves under southward IMF on 02/27/2012

On 27 Feb 2012, THEMIS A observed quasi-periodic fluctuations at the dawn flank magnetopause during the interval 1235 - 1300 UT. Figure 2.13 shows the solar wind parameters observed by Wind for the event. The red vertical dashed lines show the event interval. Time delay between solar wind monitor, Wind, and THEMIS A is approximately 25 minutes. Therefore, the interval 12:10 -1235 approximately shows the solar wind parameters for the event observed by THEMIS A during the interval 12:35-1300 UT.

The figure 2.13 shows some fluctuations in density and velocity. However the frequency of the fluctuations (as shown in wavelet spectrum of the density and velocity) is quite different from the oscillations observed by THEMIS A (as shown in Figure 2.14).

Figure 2.14 shows continuous fluctuations in the magnetic field components, the velocity components, and the ion density. THEMIS A was located at $(-0.2, -10.6, 2.8)$ Re, i.e. near the dawn terminator, and was moving anti-sunward. The fluctuations during the interval 1240 – 1250 UT are irregular, high frequency. Although, some of the B_n fluctuations look bipolar like in FTEs, they are not associated with significant maxima in the total pressure. Additionally, the total magnetic field does not have the maxima or crater-like signatures centered on the $B_n=0$ traversals which are typical for FTEs. On the contrary, the field magnitude has very distinct deep minima, which are not seen in conjunction with FTEs. Therefore, in this case, we ruled out FTEs because there are no distinct pressure maxima, and neither are there maxima or crater-like structures in the magnetic field magnitude. Instead, the magnetic field magnitude shows distinct minima, which would not be present at FTEs. The B_n signature also shows high frequency, (approximately 60 s) and continuous fluctuations, which also would not be present at FTEs.

As pointed out by Hasegawa (2012), the V_x versus N scatter method should only be used to identify rolled-up vortices in the case of northward IMF, because in the case of southward IMF low-density, high-speed flows can also result from reconnection. Thus, we have not applied this test here; however, the other criteria rule out FTEs. We considered the interval 1240-1250 UT in our survey as a KH waves during southward IMF. However, The interval 12:50-13:00 UT was considered as magnetopause crossings with no KH signatures. This interval shows some of FTEs

signatures such as Bipolar V_n and B_n and short bipolar fluctuations separated by quite.

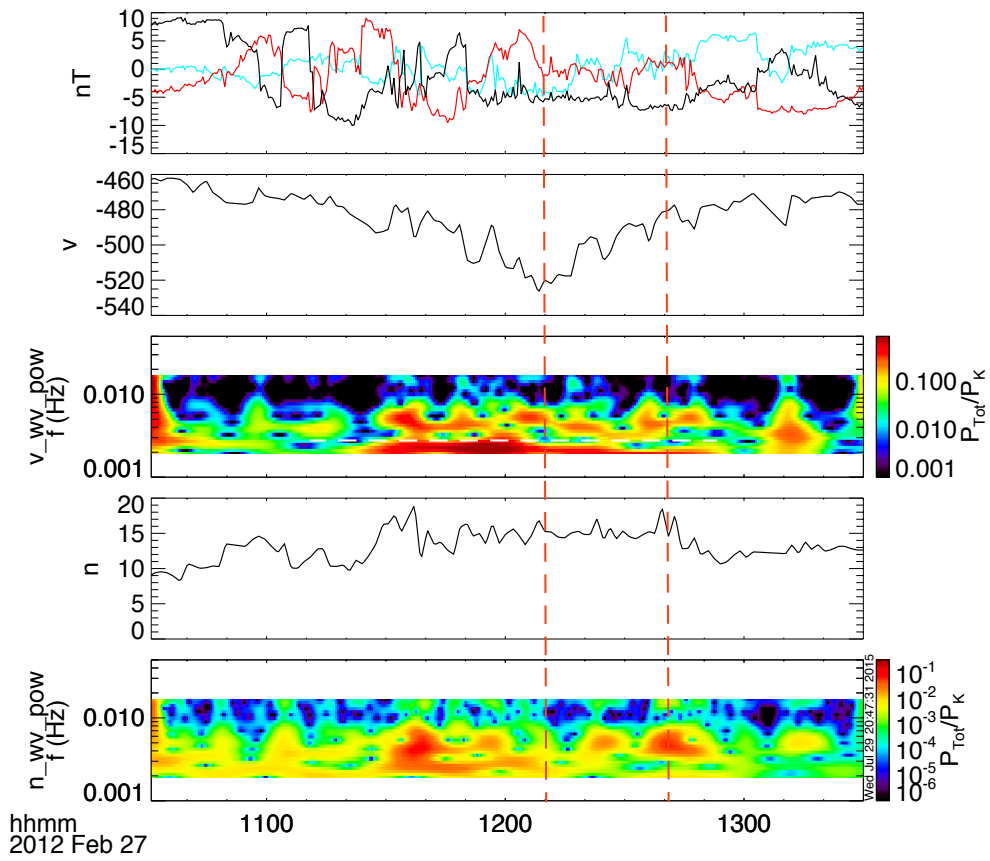


Figure 2.13 Wind observations of solar wind parameters on 27 Feb 2012. . From top to bottom: magnetic field components by (red), B_x (blue), B_z (black), X component of the velocity V_x , wavelet spectrum of V_x , density, n , and wavelet spectrum of the density. The red vertical lines shows the event interval. The frequency of oscillations in solar wind is ~ 0.025 Hz ($T \sim 400$ s).

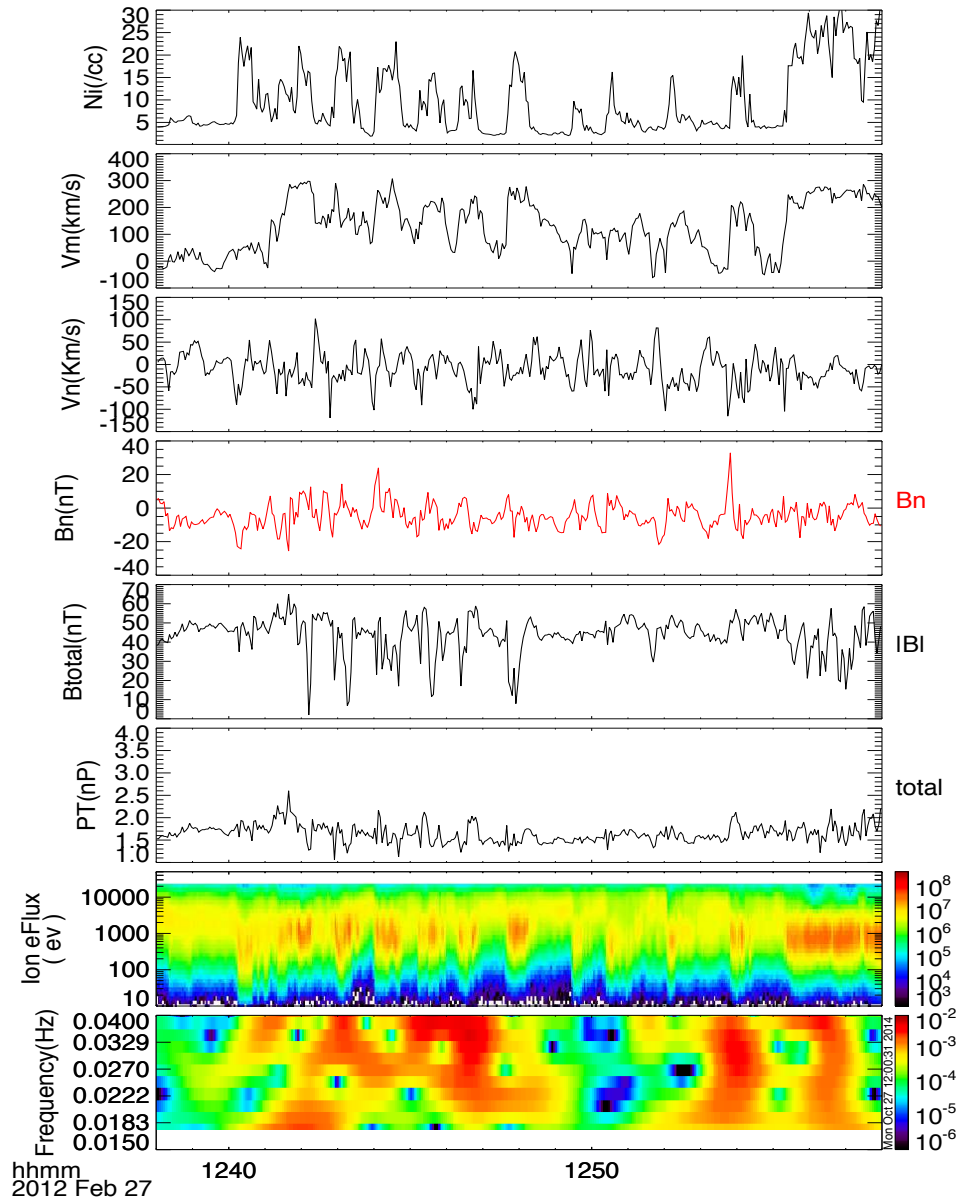


Figure 2.14: Time series of data in GSM THEMIS E observations on 27 Feb 2012. From top to bottom: (a) Ion density, (b) M component of the velocity V_m , (c) N components of the velocity V_n , (d) N component of magnetic field B_n , (e) Magnetic field magnitude B_{tot} , (f) total (magnetic plus ion) pressure, (g) Omnidirectional ion energy flux, and (h) wavelet spectra of the total pressure. For the interval 1240-1250 the wave period is approximately 60 s.

2.5.4 FTEs Event 1 on 11/30/2012

On 30 Nov 2012, THEMIS A observed quasi-periodic fluctuations at dusk flank magnetopause during the interval 1850-1950 UT. The solar wind had a flow speed 330 km/s; density of 9 cm^{-3} and the IMF vector was (0, 2, 1) nT. Thus, the IMF was very weak and slightly northward, but with B_y larger than B_z . THEMIS A was located at (7.2, 8.5, 2.6) Re, i.e. on the dayside near 15 MLT, and was moving anti-sunward. Figure 2.15 shows the event in the same format as previous events. Bipolar B_n excursions occur approximately every 4 to 5 min and are separated by periods when B_n is essentially flat. The bipolar excursions are accompanied by total pressure and magnetic field strength maxima at the center of the events, marked by red vertical dashed lines in the plot. Thus, this event has all the characteristics of a series of FTEs.

Figure 2.16 shows a scatter plot of velocity versus density for the FTEs event illustrated in Figure 2.15 to represent how different the profile would be in FTEs in compared with KH waves. The V_X -N scatter plot confirms that there are no low-density plasma flows faster than magnetosheath plasma and thus no rolled-up vortices. As expected, The V_X -N profile is completely different from the three panels in Figure 2.7 for KH waves in different stages.

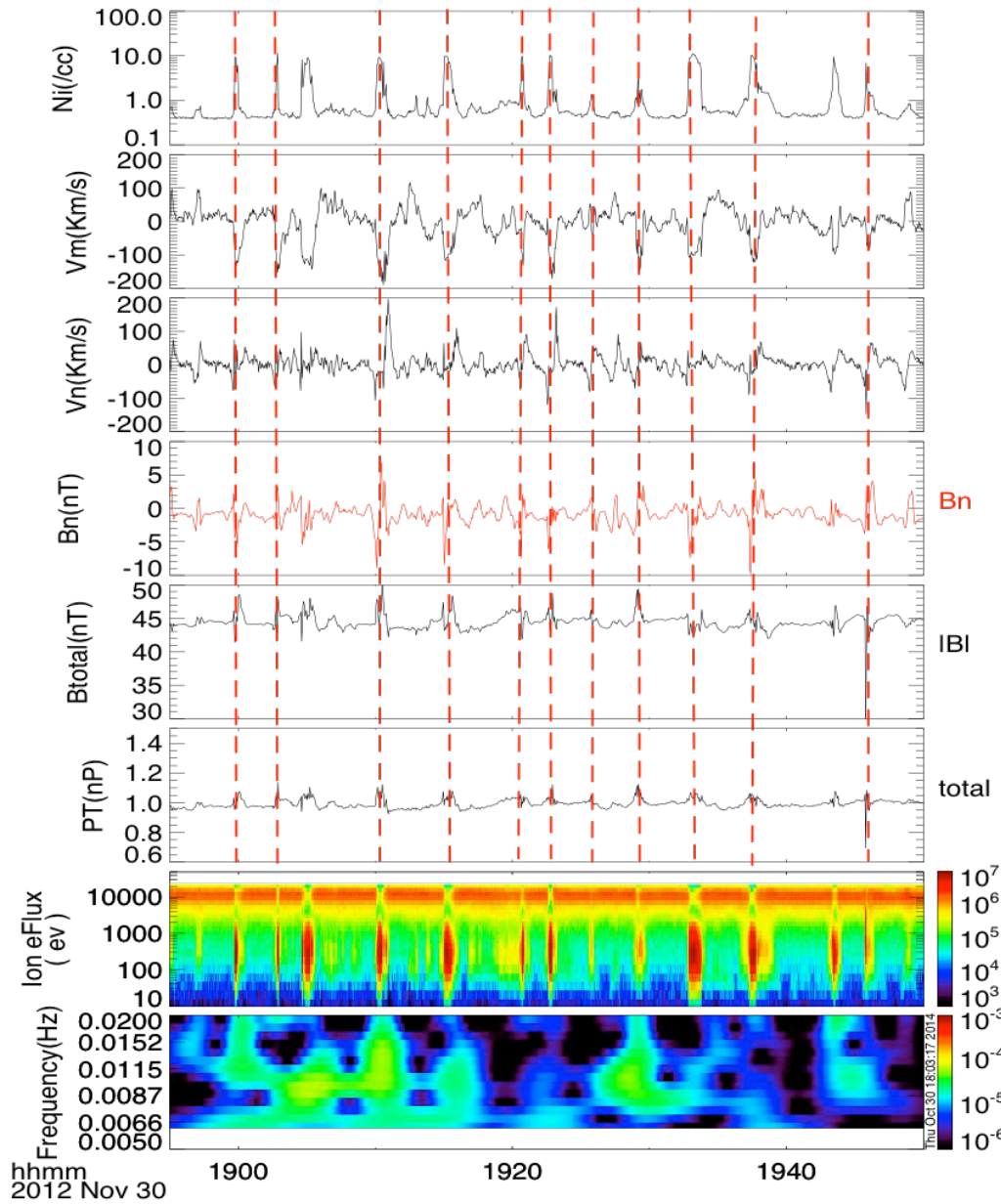


Figure 2.15: Time series of data in GSM THEMIS A observation on 30 Nov 2012. From top to bottom: (a) Ion density, (b) M component of the velocity V_m , (c) N components of the velocity V_n , (d) N component of magnetic field B_n , (e) Magnetic field magnitude B_{tot} , (f) total (magnetic plus ion) pressure, (g) Omni-directional ion energy flux, and (h) wavelet spectrum of the total pressure. The red vertical dashed lines mark the approximate centers of the FTEs.

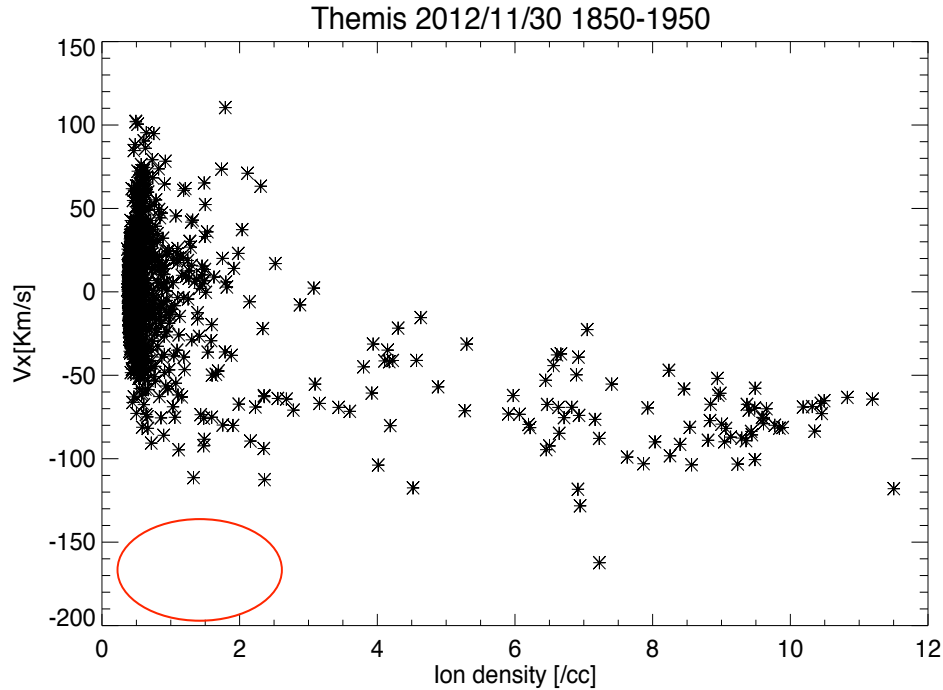


Figure 2.16: V_X - N scatter plot in the same format as previously shown, for the 11/30/2012 event. The data are from THEMIS A for 30 Nov 2012 event. Each symbol represents one of the samples, which were taken at 5 min cadence. Negative V_X values indicate anti-sunward flow. The red circle designates the area where one would expect data points if rolled-up KH vortices existed. The V_X - N profile is clearly different than the KH waves profile illustrates in Figure 2.5.

2.5.5 FTEs Event 2 on 12/16/2012

This event is similar to the previous one, but with negative IMF B_z in solar wind. On 16 Dec 2010, THEMIS D observed quasi-periodic fluctuations at the dawn flank magnetopause during the interval 1409 – 1425 UT. The solar wind had a flow speed of 500 km/s and a density of 9 cm^{-3} while the IMF vector was $(-1, -2, -2) \text{ nT}$. THEMIS D was located at $(7.5, -7.8, 4.3) \text{ Re}$, i.e. near 9 MLT and was moving anti-sunward. Figure 2.17 shows bipolar B_n pulses and all other expected FTE signatures. There is no doubt that these structures are FTEs. Nevertheless, we

show this event because it should be contrasted with Figure 2.14, which is an event that occurred under very similar southward IMF conditions. The differences between these two events demonstrate that a clear distinction can be made between FTEs and KH waves, even under southward IMF conditions. Although both produce bipolar B_n signatures, in the case of FTEs these are isolated pulses, whereas for KH wave they make up continuous waves. Also, both produce pressure and field maxima, but they align differently with the B_n pulse. Lastly, a FTE will always fail the V_X - N scatterplot test. The FTEs in this example are very strong. They have ~ 20 nT B_n peak-to-peak field, and the V_n amplitude is ~ 200 km/s. There are also significant tangential flows associated with the FTEs, but these occur mostly at the edges of the FTEs. These flows show that FTEs can essentially be viewed as solid structures that plow through the background plasma along the magnetopause. However, despite these strong flows, the tangential flow speed never exceeds the magnetosheath flow speed. This is demonstrated in Figure 2.18, which shows no accelerated flows beyond magnetosheath velocity for this event. The scatterplot pattern for this event also looks very different from those produced by the KH waves. More specifically, the FTE pattern shows more sunward flows, which arise from the flow of plasma around the FTE.

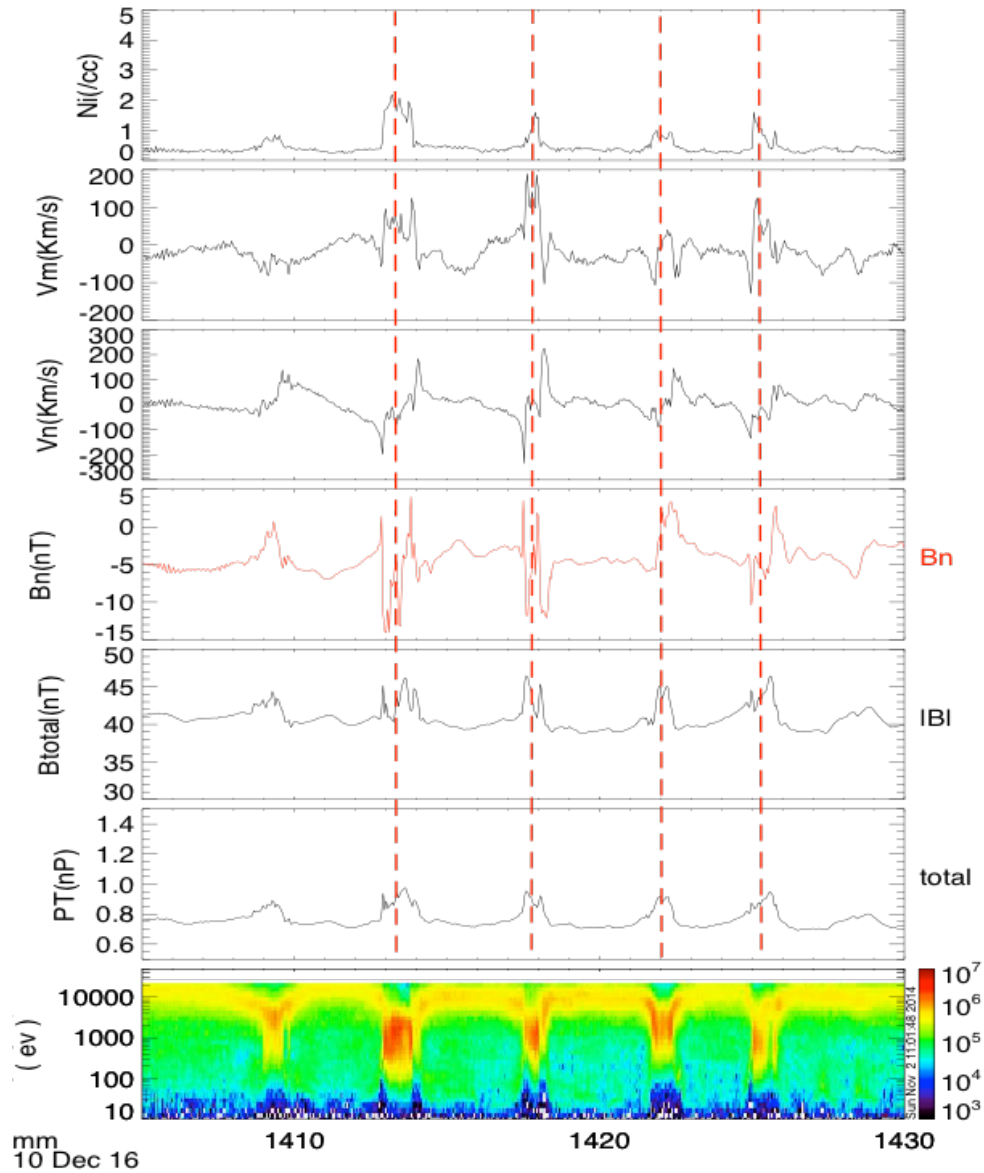


Figure 2.17: Time series of data in GSM taken by the THEMIS D on 16 Dec 2010. From top to bottom: (a) Ion density, (b) M component of the velocity (in the Earth's rest frame) V_M , (c) N components of the velocity V_N , (d) N component of magnetic field B_N , (e) Magnetic field magnitude B_{tot} , (f) total (magnetic plus ion) pressure, (g) Omnidirectional ion energy flux spectrogram. The red vertical dashed lines mark the approximate centers of the FTEs

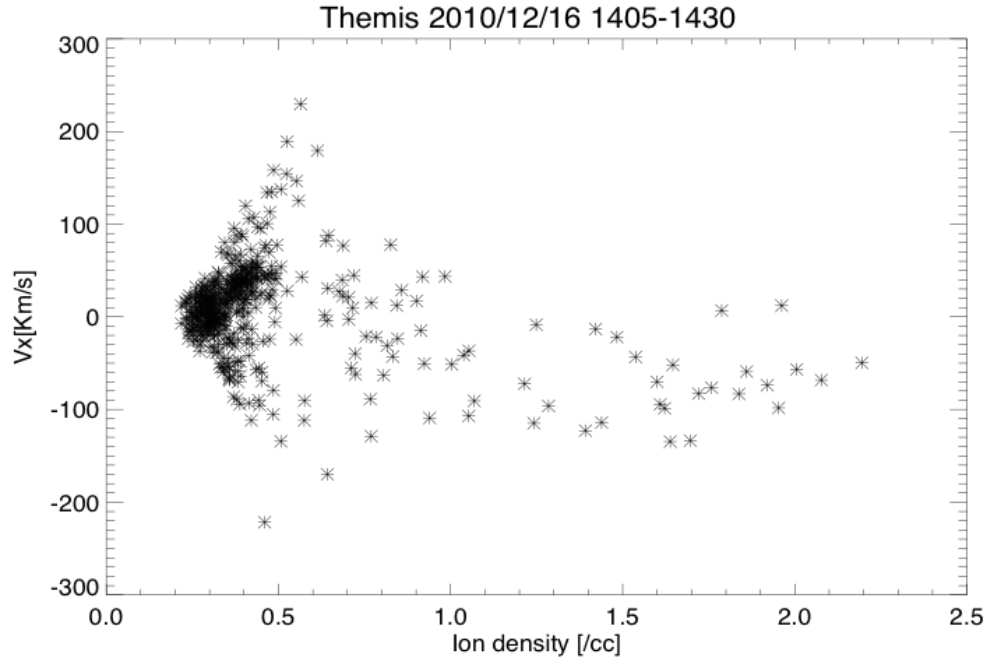


Figure 2.18: $V_x - N$ scatter plot for the 11/30/2012 event. The data are from THEMIS D on 16 Dec 2010. Each symbol represents one of the samples, which were taken at 5 min cadence. This is from a series of FTEs and shows a distribution that is distinctively different from KH wave.

2.6 KH vortices or FTEs

KH waves in nonlinear stage have similar characteristics with FTEs, for example bipolar B_n and the sometime similar periods of minutes, which make them hard to distinguish. Fortunately, there have been some differences in their observed signatures according to characteristics of FTEs and KH waves described in previous sections and summarized in Table 2.2. These different signatures would be helpful to distinguish between these two different mechanisms in observational study. The most important signatures are revealed in magnetic field perturbations and total pressure (magnetic + plasma pressure). The FTEs have specific structures in B magnetic field components explained in section 2.4.1, which are not present in the KH

waves, particularly the bipolar B_n separated by several minutes. This means when the spacecraft is crossing the magnetopause it should observe the magnetic field fluctuations followed by an ambient field. Additionally, the total pressure and total magnetic field magnitude maximized at the center of FTEs while it minimized at the center of the vortices.

Moreover, one of the most distinct signatures of KH wave in nonlinear stage is the low-density and faster-than-sheath feature, which to our knowledge has never been seen in FTEs. Accordingly, for events which the observed signatures do not clearly demonstrate all the features listed in Table 2.2, a scatterplot of the velocity component, V_x versus ion density would distinguish KH waves from FTEs. If the scatter plot confirmed that a fraction of the low-density magnetospheric plasma flows faster than the magnetosheath plasma (nonlinear stage, e.g. bottom panel in Figure 2.7) or flows with velocity similar to magnetosheath plasma (not-yet developed stage, e.g. middle panel in Figure 2.7) the event is considered as a KH event in our database.

2.6.1 FTEs and KH waves on 01/02/2011

On 2 January 2011, THEMIS A observed quasi-periodic fluctuations at dawn flank magnetopause during the interval 11:30 - 12:10 UT. The solar wind had a flow speed 330 km/s; density of 12 cm^{-3} , and the IMF vector was (4, 4, 2) nT. There were no significant solar wind dynamic pressure variations before or during the event. THEMIS A moved from (3.3, -9.9, 3.3) to (3.8, -10, 3.4) during this interval, i.e., it crossed the magnetopause about 3 R_e sunward of the dawn terminator. As shown in Figure 2.19, the characteristics of fluctuations changed from the 11:30 - 11:55 UT interval to the 11:55-12:10 UT intervals.

Table 2-2: Comparison between the properties of FTEs and non-linear KH wave.

Signature	Kelvin-Helmholtz Vortex	FTE
Magnetic field	<ol style="list-style-type: none"> 1. Bipolar B_N 2. Often has a maximum in magnetic field strength at the edge of the vortex, with less than 10 nT magnitude. 3. Continuous bipolar B_N. 	<ol style="list-style-type: none"> 1. Bipolar B_N 2. Has a magnetic field strength maximum at the core of FTE, usually larger than 10 nT magnitude. 3. Bipolar B_N separated by a few minutes quiet.
Plasma	<ol style="list-style-type: none"> 1. Substantial pressure perturbations, minimum at the vortex center and maximum at the edge. A large and rapid density increase coincides approximately with a maximum in the total pressure at the edge of the vortex. 2. Usually small perturbation in V_N. 3. Low density plasma flowing faster than sheath velocity. 	<ol style="list-style-type: none"> 1. Total pressure maxima at the FTE center. 2. Typically bipolar V_N. The V_N perturbation is usually larger than those seen in KH wave. 3. No accelerated low-density plasma.
Duration and Period	<ol style="list-style-type: none"> 1. Continuous wave trains. 2. 1-4 minute periods. 	<ol style="list-style-type: none"> 1. Short (1-2 min) bipolar B_N signatures separated by quiet. 2. Repetition period typically longer than 4 minutes.

Specifically, during the first sub interval the fluctuations are separated by several minutes of quiet each, while the second part of the event is characterized by continuous fluctuations, which also have shorter periods, i.e., ~200–250 s versus ~100 s. The first part of the event clearly consists of FTEs; it also has all the other FTE signatures listed in Table 2.2, such as the maxima of total pressure and magnetic field strength at the centers of the bipolar B_n excursions, indicated in the plot by vertical red dashed lines. Some of the FTEs can be characterized as crater-FTEs, exhibiting a W-shaped structure of the field magnitude. For the second part the event the density

jumps, indicating that traversals from the magnetosphere to the magnetosheath (marked dashed red lines) closely coincide with total pressure maxima, which are much less pronounced than the total pressure maxima of the first sub interval. Also, these maxima are located right at the edges of the density structures, which is expected for rolled-up KH vortices. The existence of B_n excursions that look somewhat bipolar also supports the interpretation that these are rolled-up KH vortices. In contrast to the FTEs of the first sub interval, however, these B_n signatures are smaller and more irregular. Figure 2.20 shows the V_x versus N scatterplot for this event. There are a few data points showing flows of low density plasma faster than the magnetosheath flow speed (~ 200 km/s), indicating rolled-up vortices. These flows all occur during the KH wave interval. During the FTE interval, the tangential flows are all less than 100 km/s, but the normal flow component is much larger than during the KH wave interval. The normal flow component (V_n) is much larger for the FTEs than for the KH waves. Note that THEMIS A is on the dawn flank during this event, thus positive V_m is tailward.

THEMIS E and THEMIS D also observed this event. THEMIS E was located at (3.2, -10.0, 3.4) at the beginning of the interval, that is, very close to THEMIS A. It observed essentially the same signatures as THEMIS A. THEMIS D on the other hand, which is shown in Figure 2.21, was located at (3.9, -9.8, 3.7), that is, further on the magnetosheath side, and only observed the FTEs, but not the KH waves. This implies that the fluctuations in each sub-interval are of different natures. In particular, the amplitude of the KH wave must be smaller than the size of the FTEs.

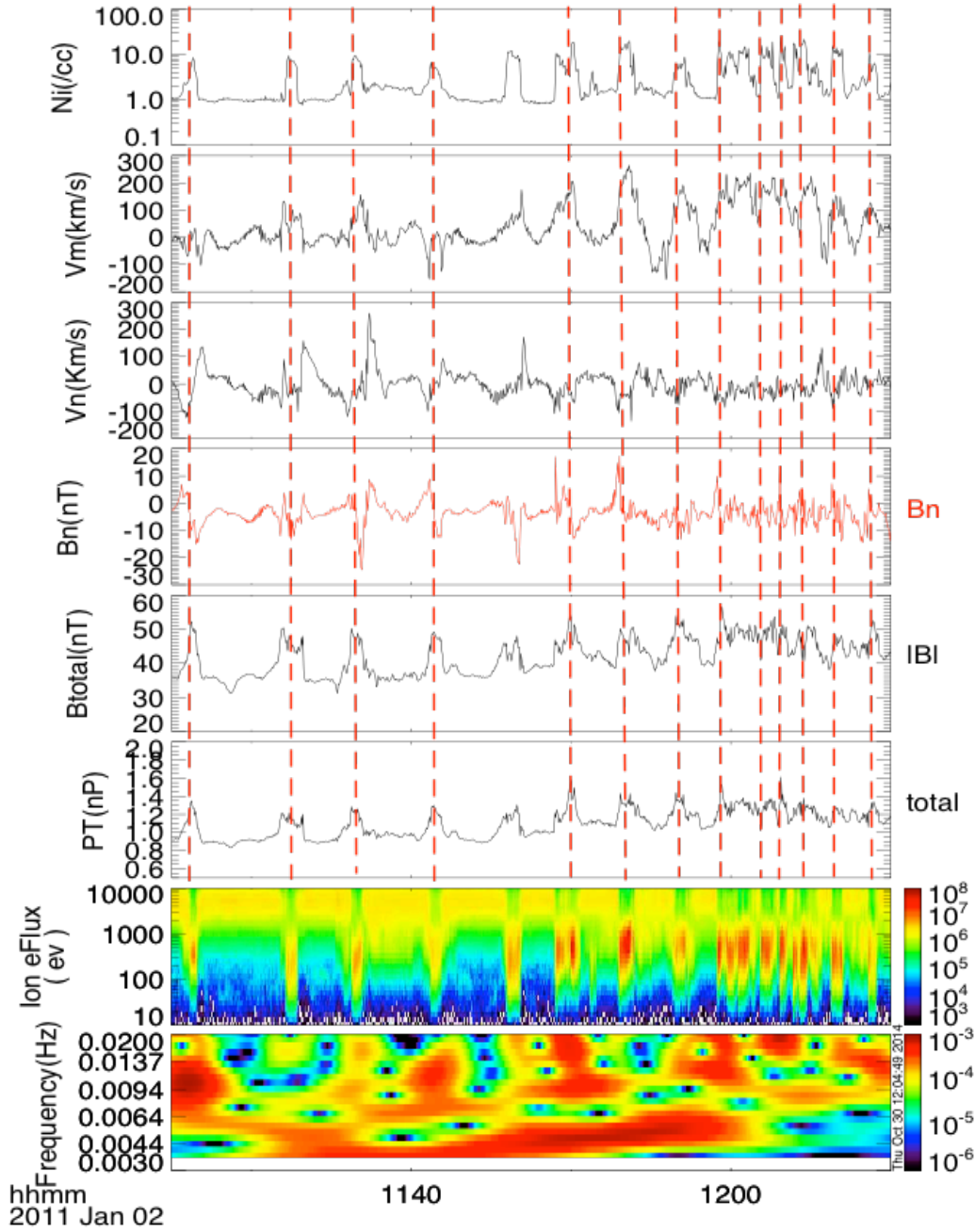


Figure 2.19: THEMIS A observations on 2 January 2011. From top to bottom: (a) Ion density, (b) M component of the velocity V_m , (c) N components of the velocity V_n , (d) N component of magnetic field B_n , (e) Magnetic field magnitude B_{total} , (f) total (magnetic plus ion) pressure, (g) Omni-directional ion energy flux, and (h) wavelet spectrum of the total pressure. The red vertical dashed lines mark the approximate centers of the FTEs during the first part of the interval 1125-1155 and passes through the edge of KH waves during 1155-1215.

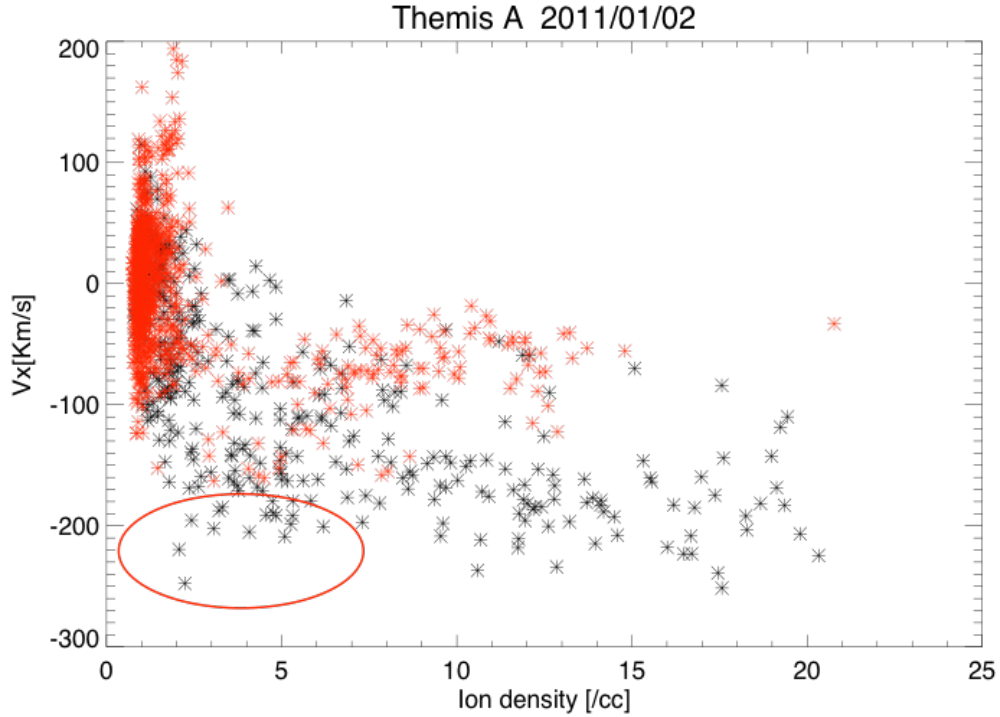


Figure 2.20: Scatter plot of the velocity component, V_x , tangential to the nominal magnetopause versus ion density seen in the rolled-up vortices detected by THEMIS. The event is the same as the one shown in Figure 2.19. Here, the $-x$ direction is defined to be along the ion velocity (in GSM) averaged over the interval under investigation (1130 - 1215 UT), and is roughly along the $-M$ direction (anti-sunward) in LMN coordinates. The red stars have shown the first part of the event (1130-1150), FTEs. The black stars have shown the second part of the event (1155-1215), KH waves. There is some low-density plasma (circled in red) that flows faster than magnetosheath plasma, confirming that rolled-up vortices are present. These data points all come from the second part of the event, i.e., 1155 – 1215 UT illustrated as a black stars as shown in the red circle.

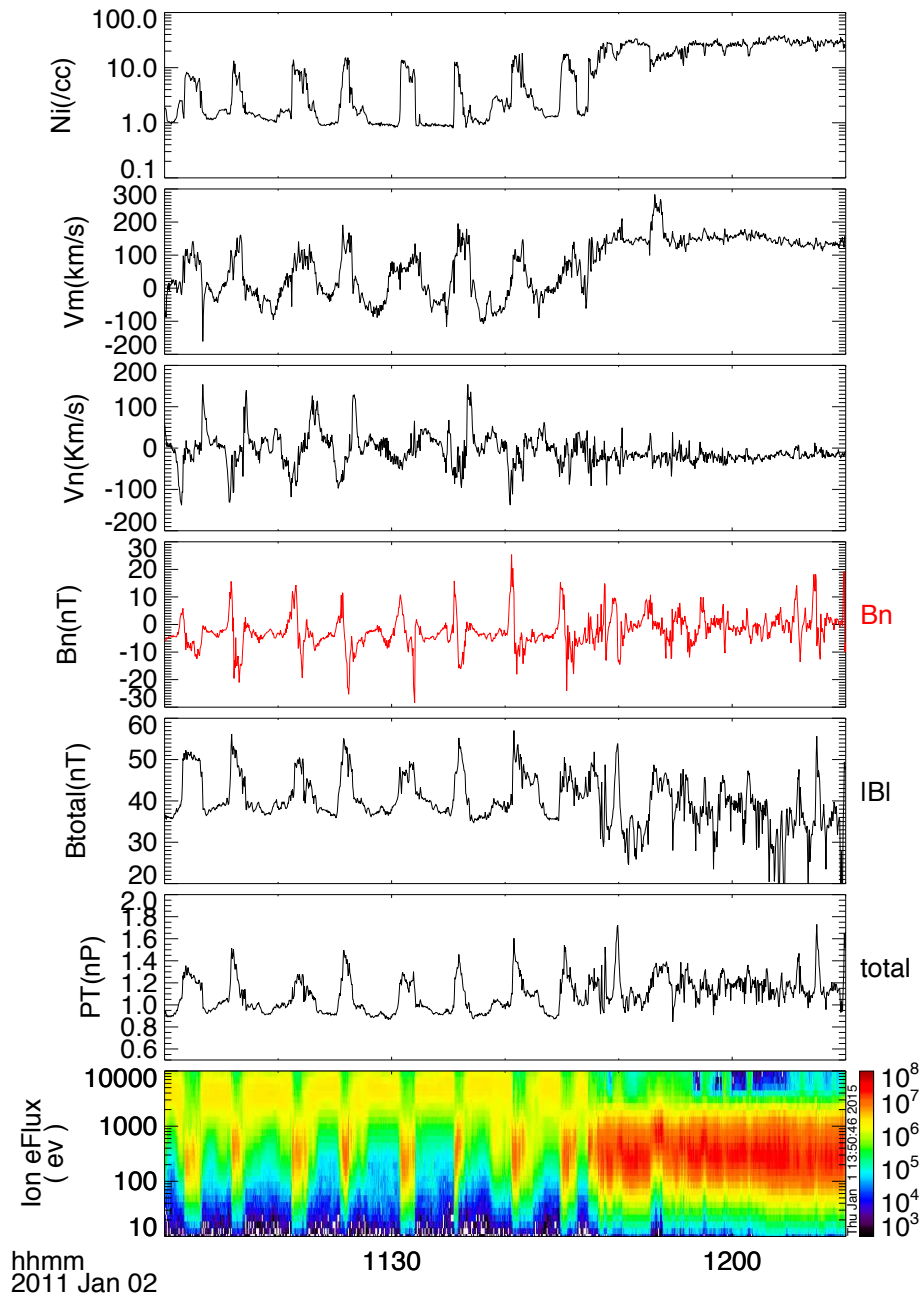


Figure 2.21: THEMIS D observations on 2 January 2011. From top to bottom: (a) Ion density, (b) M component of the velocity V_m , (c) N components of the velocity V_n , (d) N component of magnetic field B_n , (e) Magnetic field magnitude B_{total} , (f) total (magnetic plus ion) pressure, (g) Omni-directional ion energy flux, and (h) wavelet spectrum of the total pressure. The interval 1120-1150 shows FTEs signatures.

2.7 Summary

The first part of this chapter briefly reviews several numerical and observational studies on KH vortices at the flank magnetopause, as well as two important mechanisms within vortices, which are responsible for the plasma mixing: The vortex-induced reconnection, and Rayleigh–Taylor instability.

The second part of this chapter explained our methods to distinguish the KH waves in the nonlinear stage from FTEs. The properties of FTEs are well known (Elphic, 1990,1995). FTEs are magnetic flux ropes whose magnetic signatures include a distinctive bipolar excursion in the magnetic field component B_N normal to the magnetopause surface, either enhancements or crater-like variations of the magnetic field strength at the event center (Farrugia et al. 1988; Southwood et al. 1988) and a deflection of the tangential B_L and B_M components, as shown in Figure 2.4. The bipolar FTE signature is brief (0.5–2 min) and sequences of FTEs are separated by longer periods of quiet, typically 3–8 min (Elphic, 1990,1995; Farrugia et al. 1987, 1988; Southwood et al. 1988; Paschmann, 1982) as summarized in Table 2.1 whereas KH waves are continuous wave trains. In addition, the total (thermal and magnetic) pressure in a FTE typically maximizes at the center of the event (Elphic, 1995). By contrast, in a KH wave in the nonlinear stage, that is within a rolled-up vortex, the total pressure is expected to have a minimum at the center and a maximum at the edge of the vortex (Hasegawa, 2012; Miura, 1999,1997) as can be seen in Figure 2.6 and Figure 2.11. The pressure minimum occurs because the centrifugal force of the rotating vortex pushes the plasma radially outward, as depicted in Figure 2.5. The above criteria, which are summarized in Table 2.2, were not always sufficient to differentiate FTEs

from KH waves. Therefore we also exploited the fact that a rotating KH wave vortex accelerates the plasma. Thus, the less dense part of the vortex rotates faster than the denser region. Such low density, accelerated magnetosphere plasma can be exposed in a ρ (or number density N) versus V_x scatter plot, where the KH wave or vortex exhibits a distinct pattern (Hasegawa et al 2006; Taylor et al. 2012; Plaschke et al. 2014). This is demonstrated in Figure 2.7 where simulations conducted by Takagi have been used to create the expected scatter plot patterns. Figure 2.10 shows that no such signature occur for linear KH waves, that is, the case shown in Figure 2.9. The V_x - N scatter plot for the FTEs presented in Figure 2.16 and Figure 2.18 is clearly different from that produced by KH waves in the nonlinear stage, and can be used to distinguish them. However, this method could only be used for cases with northward IMF, because during southward IMF low-density, high-speed flows can also result from reconnection (Hasegawa, 2012). Figure 2.14 shows an example of KH waves under southward IMF. The figure shows irregular and high frequency oscillations with different signatures compared to northward IMF. The event was also short approximately 10 minutes.

Chapter 3

Ubiquity of Kelvin–Helmholtz waves at Earth’s Magnetopause

3.1 Introduction

Despite the progress in understanding the properties of KH waves and their effect on plasma entry, little is known about their occurrence rate. Linear theory (Talwar, 1964) suggests that KH waves are most unstable at high-flow shear; for example, high solar wind speed, as well as when the IMF is approximately northward, nearly parallel to the magnetosphere field. As these conditions rarely occur together, KH waves have often been considered infrequent events.

In the past only intermittent observations of the magnetopause were available. Because, satellite orbital dynamics makes it impossible to monitor the magnetopause over long time periods. However, with the THEMIS (Time History of Events and Macro scale Interactions during Substorms) mission originally designed to study substorms (Angelopoulos et al, 2008), which has nearly ideal equatorial orbits to study KH waves, we now have a much richer data set.

Thus, we have conducted a survey of the THEMIS mission to create a database of magnetopause crossings throughout the entire mission in order to investigate the occurrence frequency of KH waves at the Earth' magnetopause. In this chapter, we present the statistical results of our THEMIS magnetopause crossings and KH wave survey using very conservative criteria to positively identify KH waves, which have been discussed in the previous chapter. The statistical analysis shows KH waves are present at the magnetopause approximately 19% of the time and might be more important for plasma transport across the magnetopause than was previously thought, and that they frequently drive magnetospheric ULF waves. The results of this chapter have been published in Nature Communication (Kavosi and Raeder, 2015).

3.2 Event selection

We surveyed data from 2007 to 2013 when the THEMIS spacecraft frequently crossed the Magnetopause flanks during the dawn and dusk orbital phases (Sibeck, 2008) as shown in Figure 3.1. In the dusk science orbital phase the apogee of the orbits are on the dusk side of the magnetosphere, and in the dawn science orbital phase the apogee of the orbits is on the dawn side of the magnetosphere. From 2007, Probe 1 (THEMIS B) apogee was at 30 Re, probe 2 (THEMIS C) at 20 Re, probe 3 (THEMIS D), probe 4 (THEMIS E), and probe 5 (THEMIS A) were at 12 Re (Figure 3.1a,b). Since 2011, the P3, P4, and P5 have remained Earth-orbiting probes with apogees at 12-13 Re, while P1 and P2 have become ARTEMIS and orbit the moon as shown in Figure 3.1c, d. With orbit apogees between 12 Re and 30 Re, the spacecraft frequently cross the magnetopause flanks. As the orbits precessed around the Earth we examined the plasma and magnetic field data to catalogue magnetopause crossings with the motivation to

identify the KH waves. Magnetic field measurements were provided by the FGM instrument (Auster, 2008) and plasma measurements were taken from the ESA spectrometer (McFadden, 2008). We have considered periodic magnetopause crossings between a dense, cold, rapidly flowing magnetosheath plasma and interior region characterized by slower velocities and lower but substantial densities and hotter ions, or vice versa as a surface waves. However, not all magnetopause surface waves are the result of KH instability. Other mechanisms can also lead to the excitation of surface waves, such as dynamic pressure variations in the solar wind or magnetosheath (Kepko, 1972, 2002; Sibeck, 1990), non-steady magnetopause reconnection that can generate bulges in the magnetopause, or Flux Transfer Events (FTEs) (Russell, 1978). We thus needed to discriminate all magnetopause wave observations between FTEs and the buffeting of the magnetosphere by solar wind. We inspected solar wind data for every event, where possible, to confirm that the event was not preceded by rapid or periodic pressure changes in solar wind (Sibeck, 1990; Lockwood, 1991; Fairfield, 1990) that may have caused buffeting. Such events only produce a single bipolar B_n , and are thus easily distinguishable from surface waves and ruled out by our requirement of at least four wave periods. They can also often be ruled out by their irregular structure, because KH waves are to large degree monochromatic wave trains.

It was mentioned in Chapter 2 that KH waves in the linear stage can be easily distinguished from FTEs by the absence of bipolar B_n signatures and by the absence of maxima in $|B|$ and the total pressure. Also it was discussed in detail our methodology to distinguish the KH waves in nonlinear stage from FTEs.

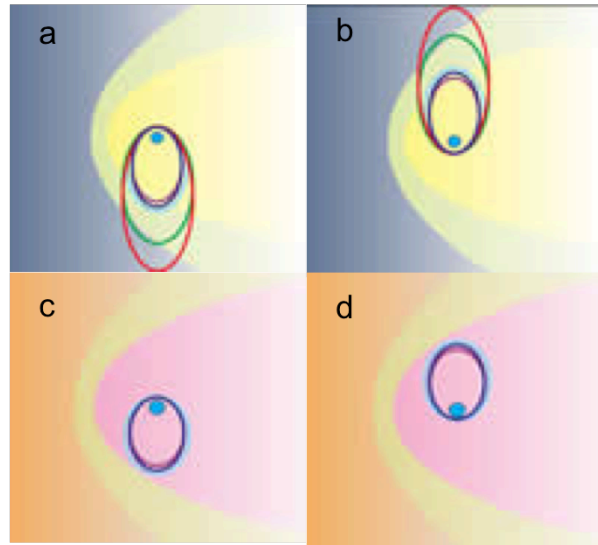


Figure 3.1: THEMIS orbita phases. Dusk phase(a) the apogee of the orbits is on the dusk side of the magnetosphere. Dawn phase (b) the apogee of the orbits is on the dawn side of magnetosphere. Probe 1 apogee (red) is at 30 Re, Probe 2 (green) at 20 Re, Probes 3 (dark blue), 4 (pink) , and 5 (light blue) at 12 Re. Dusk phase and dawn phase (c),(d). Since 2011, probes 3 and 4 apogees have changed to 12 Re, and Probe 5 apogee (light blue) has changed to 13 Re. P1 and P2 have now become ARTEMIS.

3.3 Statistical Results

We recorded solar wind conditions for each individual magnetopause crossing during the survey in order to address the correlation of KH waves with the solar wind parameters and IMF conditions. The duration of magnetopause encounters can last from minutes to hours. In order to do statistical analysis and to obtain occurrence rates, we divided each encounter into 5-min intervals. Each interval is classified as KH wave or not, and tagged with ancillary data, such as time-shifted five minute resolution OMNI solar wind and IMF data. Our database consists of 11,500 5-min samples covering 960 hours of dwell time at the magnetopause. The samples are nearly evenly divided between northward (500h) and southward (460 h) IMF conditions. The

data are thus unbiased with respect to solar wind and IMF conditions, but not with respect to the 11-year solar cycle, as they are mostly from solar minimum conditions. We find that about half of the crossings show waves or quasi-periodic variations, although not all of them are KH waves. The overall occurrence rate of KH waves is approximately 19% regardless of solar wind and IMF conditions. This is a substantially higher rate than the linear dispersion relation would suggest.

3.3.1 Occurrence rate

Scatterplot of velocity versus clock angle of all KH waves and magnetopause crossings for the entire THEMIS mission is plotted in Figure 3.2. Five-minute resolution OMNI data that provide the time-shifted IMF and solar wind parameters have been used. Each dot shows five minutes of magnetopause crossing. Each orange dot shows five minutes of KH waves and each gray dot indicates five minutes magnetopause crossing. The figure shows the KH events occurring for all range of velocity and clock angle. The occurrence rate and the total events (total five minutes magnetopause crossings) for each year from 2007 to 2013 are presented in Figure 3.3.a. Figure 3.3a shows that the average occurrence rate of KH waves for the entire THEMIS mission survey is approximately 19%; however, the occurrence rate changes from the minimum occurrence ~12% in 2009 and 2010 to maximum occurrence ~ 23% in 2011.

Figure 3.3b shows the number of sunspots for each year from 2001 to 2015. This Figure represents that there was minimal activity until early 2010. This is the lowest recorded sunspot activity since accurate records began in 1750. The Figure 3.3b shows sunspot numbers starts decreasing from 2007 to 2009. In 2009, Sun reached to its minimum activity and then the sun

spot numbers start increasing again. This is in good agreement with our result presented in Figure 3.3a, which Minimum KH occurrence rate occurs during the year with the minimum sunspots (2009 and 2010), and maximum occurrence rate occurs during the year with maximum sunspots (2011).

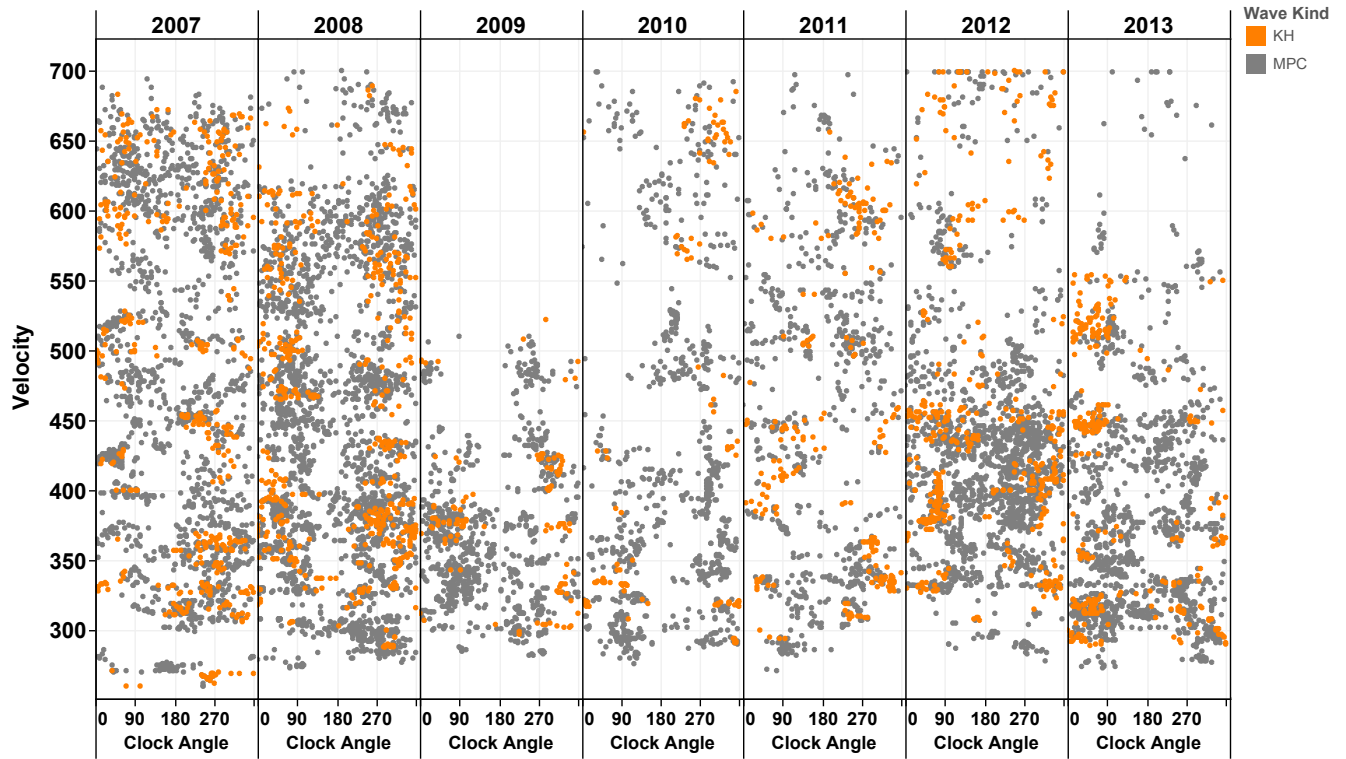
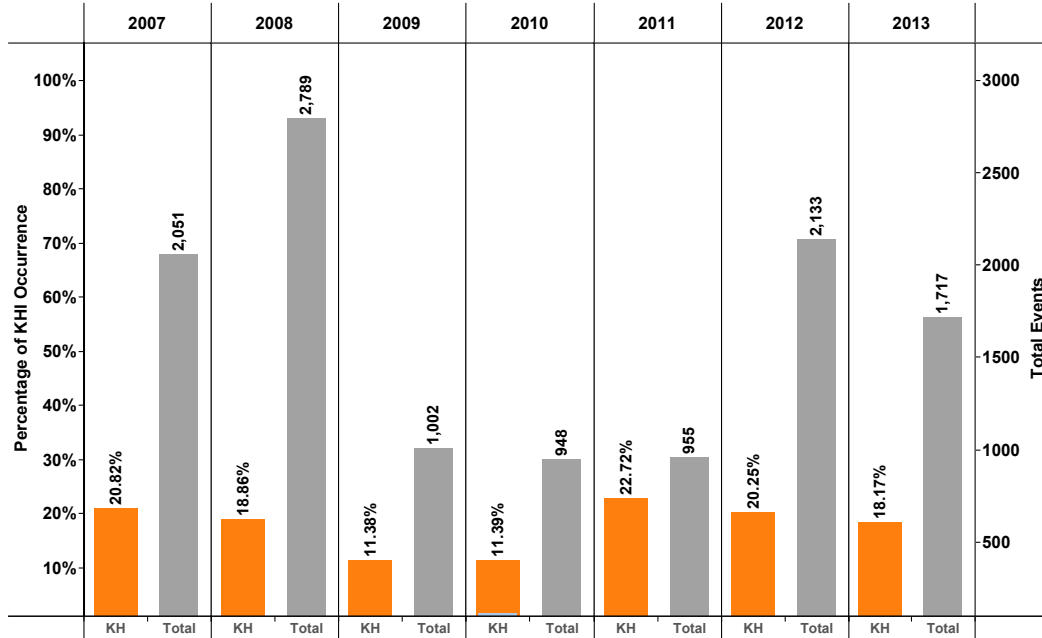


Figure 3.2: Scatterplot of occurrence of KH waves and total magnetopause crossings, for different years from 2007 to 2013. The distribution of occurrence of all events (KHI and total magnetopause crossings) is plotted for different clock angle and velocities. Each dot shows five minute of magnetopause crossing. Color shows details about wave kind KH waves (orange) and total events (gray).

(a)



(b)

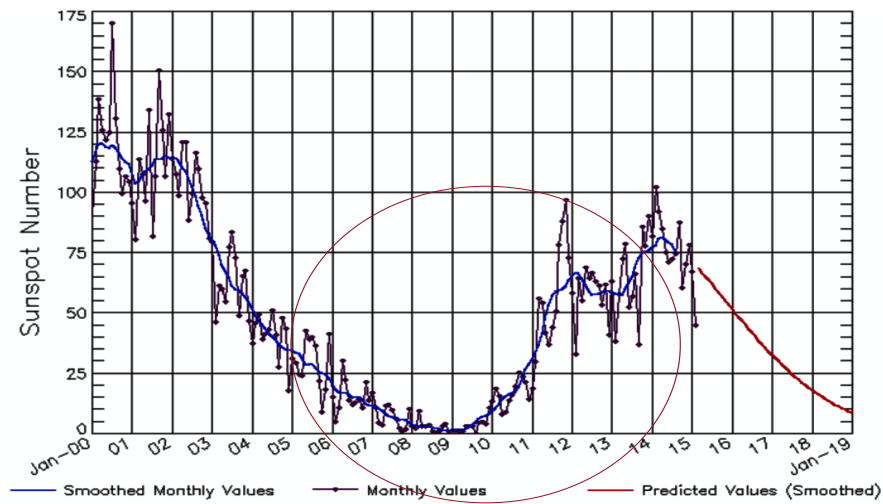


Figure 3.3: Top panel (a) shows occurrence rate of KH wave for different years 2007-2013. Orange bins show the relative KH wave occurrence rate and grey bins show the number of 5-min KH wave intervals in that bin. Bottom panel (b) shows sunspot number from 2001-2018. The red circle shows the interval of our THEMIS survey 2007-2013.

3.3.2 IMF dependence

Figure 3.4 shows the KH waves occurrence rate as a function of IMF clock angle and IMF cone angle. As a function of clock angle (a), the occurrence rate is 35% for near northward IMF, near 20% if the IMF lies in the equatorial plane, and about 10% for southward IMF. KH wave occurrence maximizes for northward IMF, but is still significant during southward IMF. The fact that KH waves occur during southward IMF at a significant rate is not expected; because it is generally thought that magnetic reconnection dominates over KH instability during such conditions and prevents KH wave's growth.

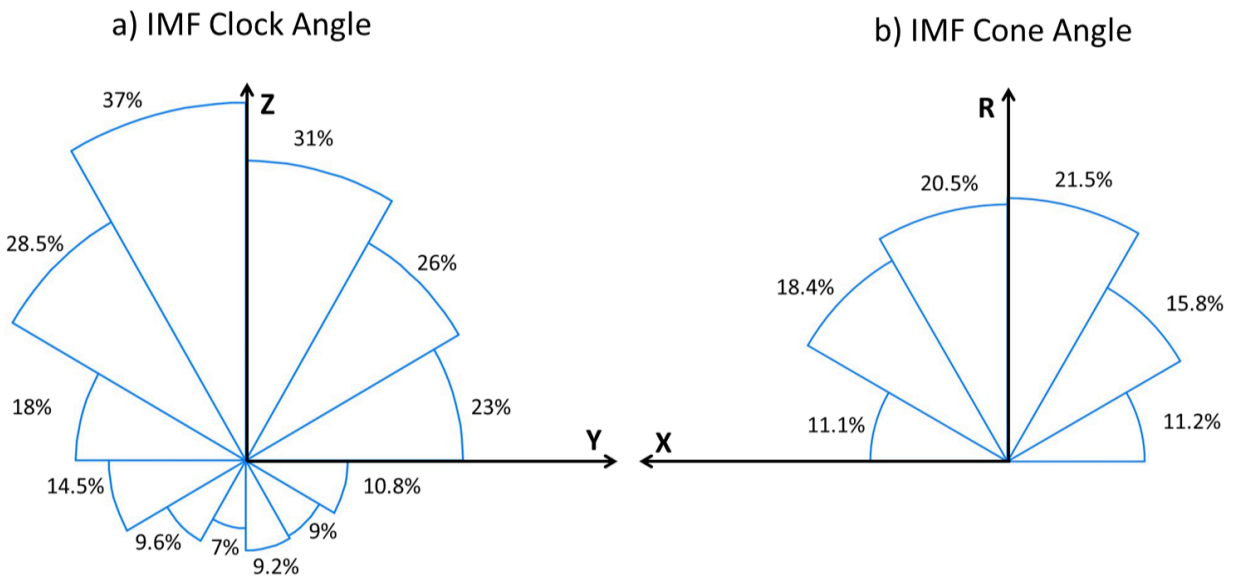


Figure 3.4: KH waves occurrence rate as a function of IMF clock angle (a) and cone angle(b). The clock angle is defined as $\text{atan}(B_y/B_z)$, and the cone angle is defined as $\text{acos}(B_x/B)$. X points towards the Sun, Y points duskward, Z points north, and $R = (Y^2 + Z^2)^{1/2}$.

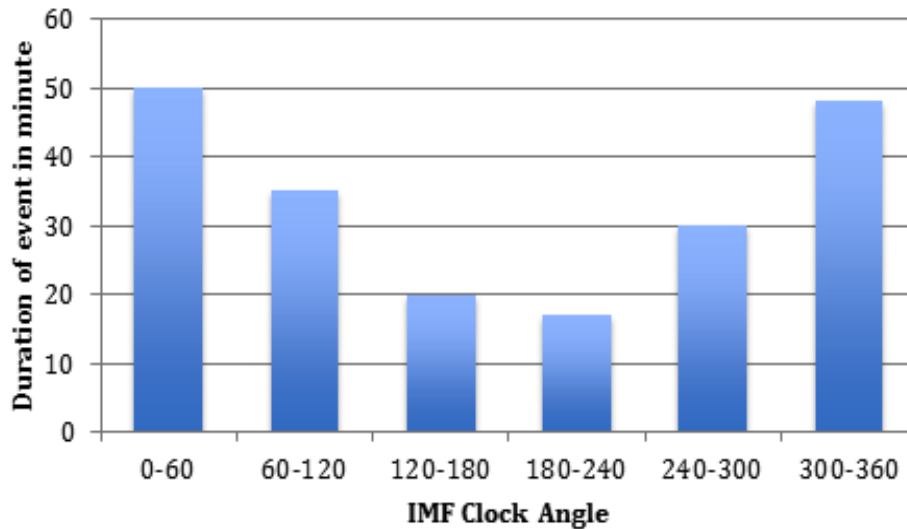


Figure 3.5: The duration of KH waves event versus different clock angles.

The IMF cone angle dependence (b) is as expected from the linear dispersion relation of KH waves (Talwar, 1964) which predicts that the instability maximizes when the magnetic field on either side of the shear layer is close to collinear, which occurs for 90° cone angle. The IMF is more effective generating KH wave when it is oriented perpendicular to the Sun–Earth line.

The dependence of the KH event’s duration on the IMF clock angle is shown in Figure 3.5. The average duration of KH events during southward IMF with clock angle from 120-240 degrees is approximately 20 minutes, while the duration of the event under northward IMF is more than two times longer at approximately 50 minutes. We can conclude that southward IMF cases have only short durations and may be ineffective in shaping the global character of the magnetosphere.

3.3.3 Solar wind parameter dependences

Occurrence rate of KH wave as a function of solar wind plasma parameters, velocity, density, Mach number, and magnetic field magnitude are plotted in Figure 3.6. Figure 3.6a shows the occurrence percentage of KH waves (orange bins) and the corresponding number of 5 min intervals (grey bins) as a function of solar wind speed. The latter is shown to assess the statistical significance of the data. As expected, the occurrence frequency increases with solar wind speed. However, the occurrence of KH waves at very low solar wind speed is unexpected. There appears to be no low-speed cutoff for KH waves; KH waves are still observed at 270 km/s solar wind speed. The KH wave dependence on solar wind density (Figure 3.6b) is weak. At low densities, there is a positive correlation, which tapers out for densities larger than 10 cm^{-3} . There is also a positive correlation with the solar wind Alfvén Mach number (Figure 3.6c), which also tapers out at high (>16) Mach numbers. The IMF magnitude (Figure 3.6d) appears only to have an effect for unusually high values of more than 16 nT. It is tempting to compare the KH wave dependencies with the KH dispersion relation; however, the solar wind parameters are not the same as the plasma and field parameters on the magnetosheath side of the magnetopause flanks. In particular, the solar wind is slowed down by the bow shock and then re-accelerates along the flanks of the magnetosphere. Therefore, the magnetosheath velocity is generally slower than the solar wind, but it is also possible that the draped IMF accelerates the magnetosheath plasma to speeds larger than the solar wind speed. However, the trends shown in Figure 3.6 are in agreement with linear theory, including the increase of the KH wave rate with solar wind speed, and the apparent suppression of KH waves for strong IMF, which was predicted by theory (Miura, 1984).

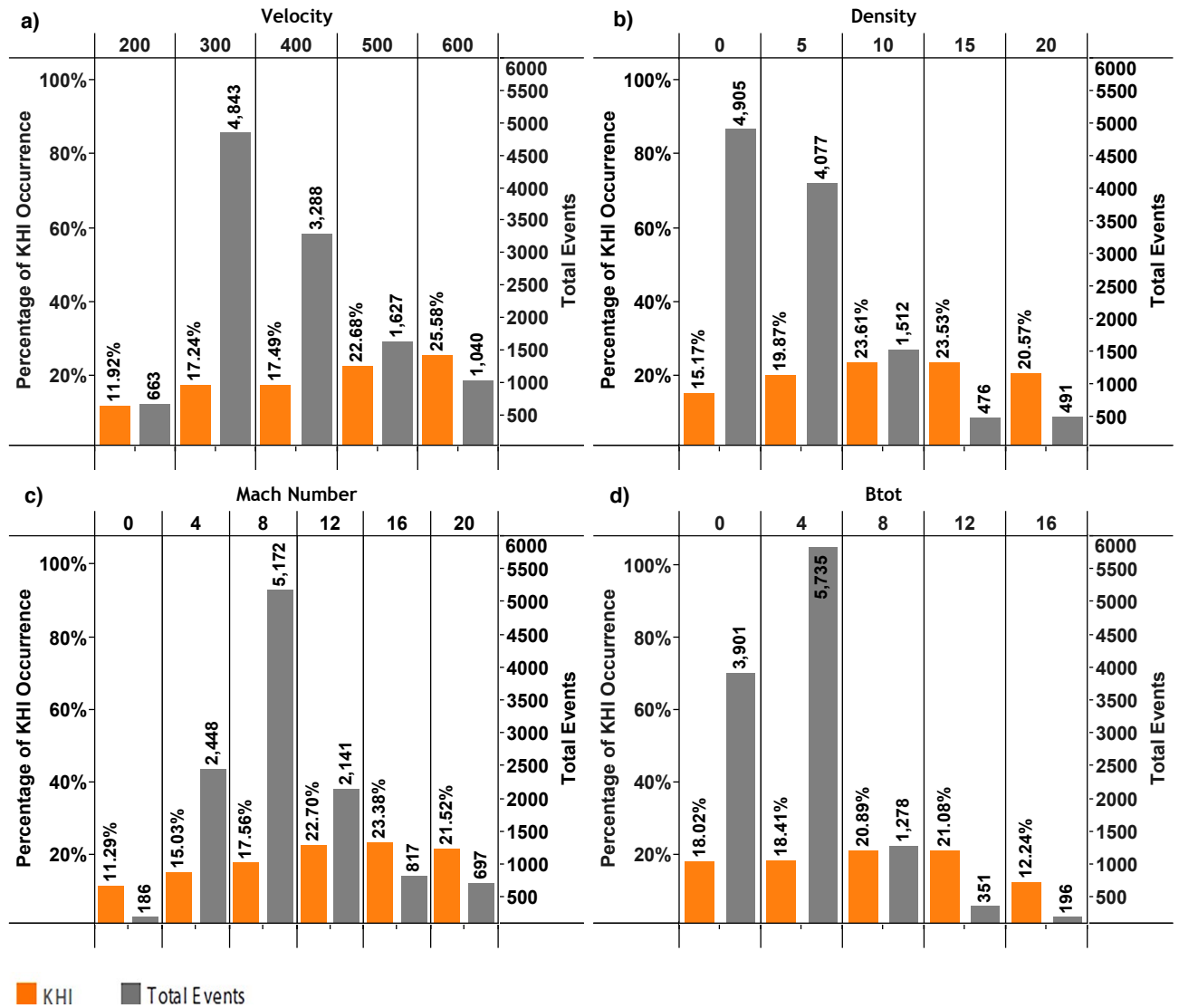


Figure 3.6: Occurrence rate of KH wave as a function of solar wind plasma parameters. Orange bins show the relative KH wave occurrence rate and grey bins show the number of 5-min KH wave intervals in that bin. The panels show, respectively, the dependence on the solar wind velocity (a), the solar wind density (b), the solar wind Mach number, and (c) the IMF magnitude. The parameter dependence is mostly as expected from the KH dispersion relation, but the significant occurrence rate at low velocity (<300 km/s) is not expected.

3.4 Discussion and Conclusions

Linear MHD theory predicts that KH waves are most unstable when the magnetic field on either side of the shear layer is perpendicular to both the flow direction and the direction of the velocity gradient. Furthermore, the growth rate increases with flow shear. Thus, it has commonly been assumed that KH waves at Earth's magnetopause are restricted to times of nearly northward IMF and high solar wind speed. This would make them rare events with little importance for magnetospheric dynamics. Although the dispersion relation does not distinguish between northward and southward IMF, that is, whether the magnetic field is parallel or anti-parallel across the shear layer, it was commonly assumed that during southward IMF period magnetic reconnection would dominate over KH wave generation. However, recent reports have shown that KH waves may also occur during southward IMF conditions (Hwang et al. 2011; Yan et al. 2014) but these were case studies that gave no indication as to whether these were singular events or whether they would occur more commonly.

Refined theoretical analysis that has taken into account the finite width of the shear layer and its structure has further narrowed the parameter range under which KH waves should occur (Gratton et al. 2004). However, the true occurrence rate of KH waves remained uncertain, and many researchers assumed they were rare events. Statistical studies have long been hampered by the lack of suitable data. Although Pc5 waves observed on the ground are often associated with KH waves (Rae et al. 2005), they may also have other causes and thus provide no suitable statistics. On the other hand, in-situ observations are restricted by satellite orbital dynamics.

Before THEMIS, most missions had orbits that would preclude frequent KH wave observations, or the missions were too short to obtain sufficient data for statistical studies. For the first time ever, THEMIS has provided a sufficiently large database of magnetopause crossings in the equatorial plane, together with suitable instrumentation, to allow for the study presented here.

Our results show that KH waves are much more ubiquitous and occur under most solar wind and IMF conditions. We confirm the presence of KH waves even during southward IMF conditions, in line with recent event studies (Hwang et al. 2011; Yan et al. 2014). During northward IMF, KH waves occur frequently, particularly during periods of low solar wind speed. Theoretical models suggest that the growth rate diminishes for small flow shear and that there may even be a cutoff velocity. By contrast, we find only weak velocity dependence and no indication of a cut-off.

It is not clear why the data are difficult to reconcile with linear theory, but the most likely reason seems to be that the dispersion relations are based on the assumption of a simply structured shear layer, i.e., either a jump-like discontinuity, or a smooth transition of finite thickness. In reality, however, the magnetopause often has a complicated boundary layer structure, which generally does not match these assumptions. The presence of such boundary layers makes it thus difficult to test the dispersion relations, because single spacecraft observations generally do not reveal their structure.

Because KH waves can facilitate the entry of solar wind plasma into the magnetosphere, they are thus more important for the magnetosphere mass budget than previously thought.

However, quantifying the importance of KH waves for mass transport across the magnetopause remains to be performed. KH waves are also thought to be significant drivers of magnetospheric ULF waves, which in turn can energize the particles in Earth's radiation belts (Walker, 1981; Rae et al. 2005; Elkington, 2006). Thus, KH waves may also be a more important factor for radiation belt dynamics than previously conceived.

Chapter 4

Simulation results: OpenGGCM

4.1 Introduction

Global modeling has been proven to be an extremely powerful tool to study the solar-terrestrial plasma interaction. During the last two decades a large body of numerical simulations have been carried out, including local magneto hydrodynamic (MHD) (Otto and Fairfield 2000; Nakamura and Fujimoto 2005; Nykyri and Otto 2001; Matsumoto and Hoshino 2004, 2006), hybrid (Thomas and Winske 1991, 1993; Fujimoto and Terasawa 1994; Cowee et al. 2009; Delamere, 2009) and full particle simulations (Nakamura et al. 2011, 2013). Although it has been shown that the KH wave has a global three-dimensional character (Merkin et al. 2013) it has remained difficult to define in global magnetospheric simulations because of their limited resolution. In this chapter we present results from global, three-dimensional magneto hydrodynamic (MHD) simulations the Open Geospace General Circulation Model (OpenGGCM) (Raeder et al. 1996, 1998, 2003). The OpenGGCM simulations are used to study KH instability at Earth's magnetopause.

The primary goal of this chapter is to investigate how solar wind plasma and IMF parameters can affect the instability criteria and the characteristics of the waves generated by the KH instability. The second goal of this chapter is to test how accurate the OpenGGCM model can resolve the instability and what controls this accuracy. To reach the first goal, we drive the simulations with idealized, constant solar wind input parameters for both southward and northward IMF conditions. Driving the simulations with constant solar wind parameters ensures that any discrete ULF pulsations in the simulation magnetosphere are not the result of perturbations in solar wind. Thus, any magnetopause surface waves that are generated in the simulations cannot be the result of perturbations in the solar wind. Although the OpenGGCM reasonably produces KH waves under idealized constant solar wind conditions, its accuracy to generate the instability under real solar wind data is more important. Thus, in the remaining sections of this chapter we present the simulation result for the event on 7 June 2014 observed by THEMIS, which is an interesting event under both southward and northward IMF conditions. The outline of this chapter is as follows. First part discusses the OpenGGCM simulation of KH instability under constant solar wind parameters for both southward and northward IMF conditions. In the second part, we compare THEMIS Observations with the OpenGGCM simulations of the KH waves.

4.2 The OpenGGCM

The simulation code required for this study already exists. The OpenGGCM global MHD model simulates the interaction of the solar wind with the magnetosphere-ionosphere-thermosphere

system. This model has been developed and continually improved for over a decade. The OpenGGCM has been implemented for a variety of studies; magnetopause reconnection (Berchem et al. 1995a, b), FTEs (Raeder, 2006), the plasma depletion layer (Wang et al. 2003, 2004), and plasma entry due to double lobe reconnection (Li et al. 2005, 2008a, 2009a). A more detailed description of the code and the methods used can be found in Raeder et al. (2008). The OpenGGCM model has been used to simulate and study the KH waves at the flank magnetopause. In principle, KH waves are difficult to simulate with a global magnetosphere code because the scale size of the waves is much smaller than the size of the entire magnetosphere, and the surrounding regions upstream of the bow shock and several 100 R_e of the tail that need to be part of the simulation. In particular, the presence of the Low Latitude Boundary Layer (LLBL), which is usually only a fraction of one R_e thick, makes this a difficult task. However, because of ever increasing computer power and the stretched Cartesian grid design of the OpenGGCM, we can now easily achieve a resolution of 0.03 - 0.1 R_e or better near the dayside and near-tail magnetopause, which greatly facilitates the analysis of magnetospheric processes such as KH waves.

4.3 Generic Runs: Constant Solar Wind

To study KH instability based on basic MHD physics, we need to create a solar wind data input file. This file describes the time-dependent solar wind boundary conditions at the sunward boundary of the simulation domain. Table 4.1 presents the solar wind input file that has been used for the generic run in this study. As shown in Table 4.1, the simulation is conducted with

idealized solar wind condition for KH instability such as high solar wind stream and average solar wind plasma parameters under pure southward and northward IMF conditions with no dipole tilt in order to concentrate fully on the effects of velocity shear. We ran three hours of simulation: The first hour was set to be under purely southward ($B_z < 0$ nT, $B_y = B_x = 0$ nT) and the last two hours under northward IMF conditions ($B_z > 0$ nT, $B_y = B_x = 0$ nT). The simulations have been conducted with high-resolution 600×400×300 version of the magnetospheric grid with the typical cell size of approximately 0.07 Re.

Table 4-1: Solar Wind input Parameters

Time (min)	IMF			SOLAR WIND				
	b_x (nT)	b_y (nT)	b_z (nT)	V_x (km/s)	V_y (km/s)	V_z (km/s)	N (cm ⁻³)	P (pPa)
-999.000	0.000	0.000	-5.000	700.000	0.000	0.000	6.000	6.000
60.000	0.000	0.000	5.000	700.000	0.000	0.000	6.000	6.000
120.000	0.000	0.000	10.000	700.000	0.000	0.000	6.000	6.000
180.000	0.000	0.000	10.000	700.000	0.000	0.000	6.000	6.000

4.3.1 Overview of simulation results

Figure 4.1 and Figure 4.2 both display the time series of virtual spacecraft observations of the simulated KH waves and vortices along the magnetopause. The figures track the evolution of KH waves from dayside past to dawn flank magnetopause. The oscillations are visible in the magnetic field components b_x , b_y , b_z , the velocity components V_x and V_y , and the ion number density which is shown with n . The oscillations of the velocity y -component, which are nearly identical with the velocity normal to the magnetopause, show that the magnetopause moves back

and forth. The V_x component oscillates because the magnetosheath plasma streams tailward, while the magnetosphere plasma does not. Figure 4.1 shows the time series of simulation results generated from virtual spacecraft observations located at the point (3, -9,0) Re close to the dayside magnetopause. The small amplitude waves during both southward and northward IMF conditions confirm that waves are just beginning to form, and still are in the linear stage. Figure 4.2 presents the time series of simulation results generated from virtual spacecraft observations located further down the flank magnetopause at point (-10, -15.5,0) where the waves are expected to grow to nonlinear stage. The figure shows high frequency oscillations in plasma parameters and irregular oscillations in magnetic field under southward IMF conditions. However, the waves under northward IMF are regular with sinusoidal and wavy structures. The waves under northward IMF present large oscillations in velocity components while during southward IMF the oscillations in velocity are small. These different structures of the waves under southward and northward IMF are more evident in Figure 4.3. The figure compares the KH wave structures under southward IMF (first hour of run in Figure 4.2) with the KH waves structures under northward IMF (second hour of run in Figure 4.2). The plot on the left shows irregular oscillations in x and y magnetic field components under southward IMF. On the other hand, the waves under northward IMF (panel) present regular and wavy oscillations in x and y velocity components, magnetic fields, and sometimes the bipolar signature in b_y similar to the KH waves signatures from in-situ studies. These differences all indicate how different the waves behave under southward and northward IMF conditions.

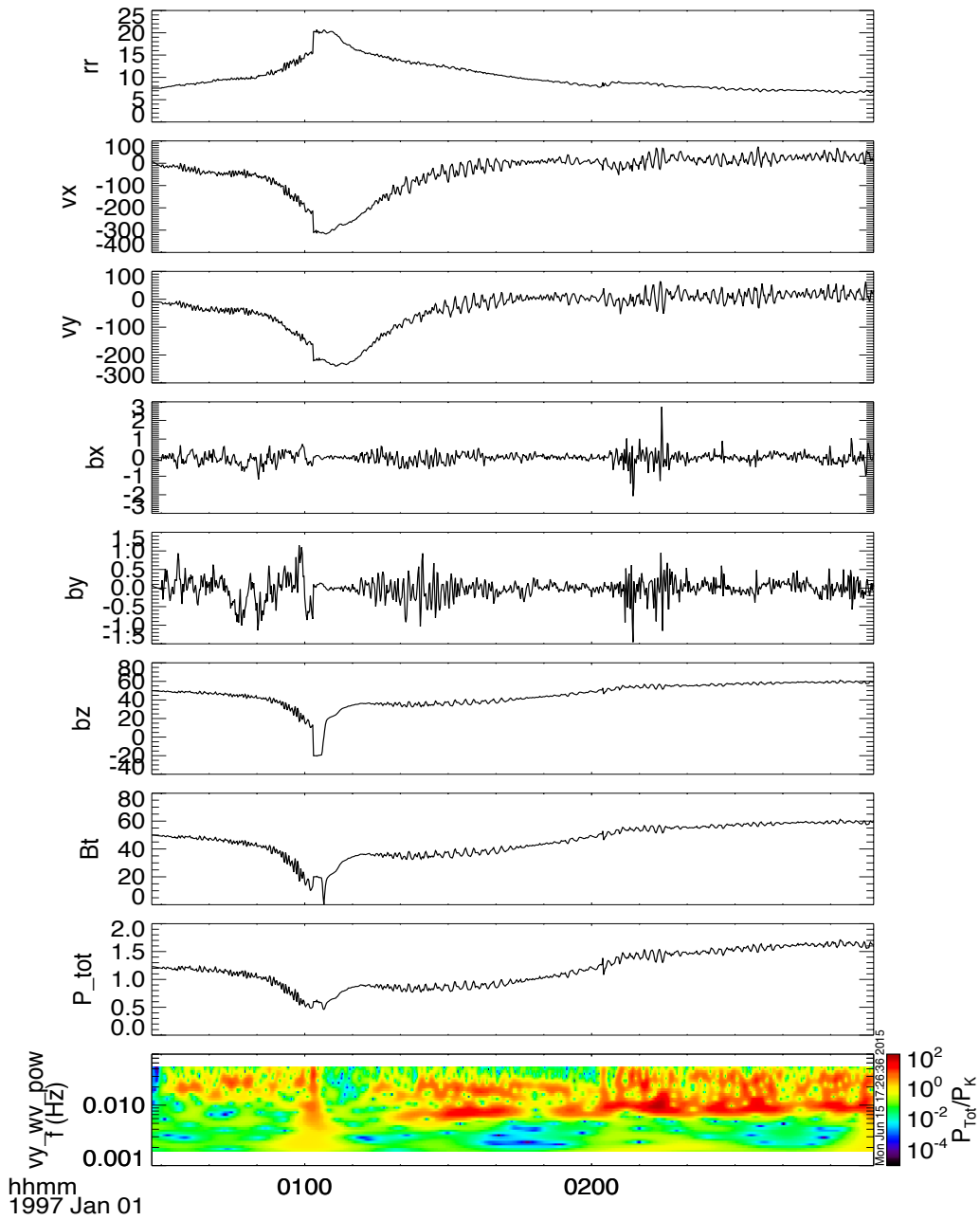


Figure 4.1: Time series of OpenGGCM simulation under constant solar wind at the point close to terminator (+3, -9, 0). From top to bottom: Ion density rr , x component of the velocity V_x , y components of the velocity V_y , x and y components of magnetic field B_x , B_y , Magnetic field magnitude B_{tot} , total (magnetic plus ion) pressure, and wavelet spectrum of the y component of velocity.

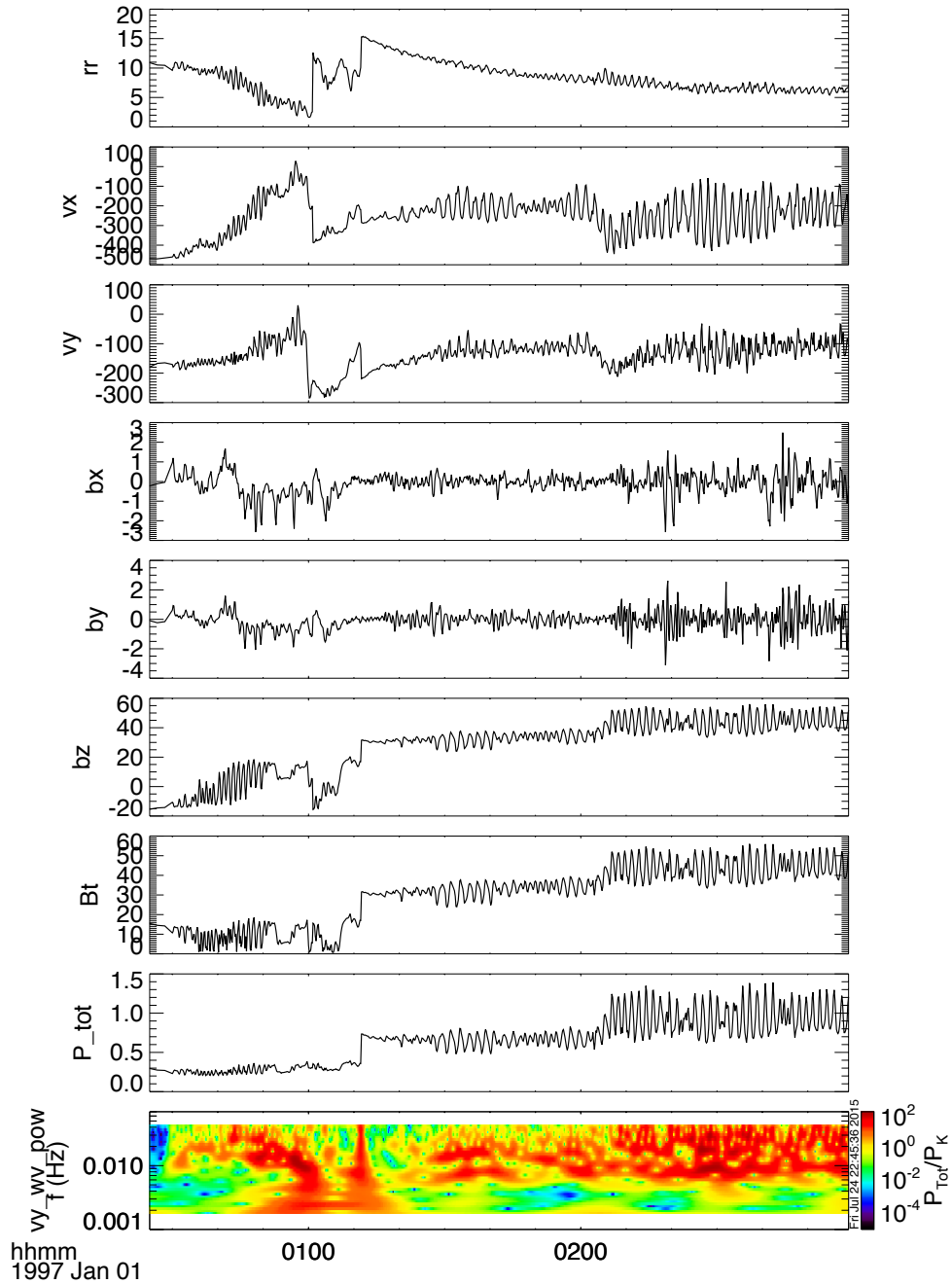


Figure 4.2: OpenGGCM simulation under constant solar wind at $(-10, -15.5, 0)$ downstream of the dawn meridian. From top to bottom: Ion density nr , x component of the velocity Vx , y components of the velocity Vy , x and components of magnetic field Bx , By , Magnetic field magnitude B_{tot} , total (magnetic plus ion) pressure, and wavelet spectrum of the y component of velocity.

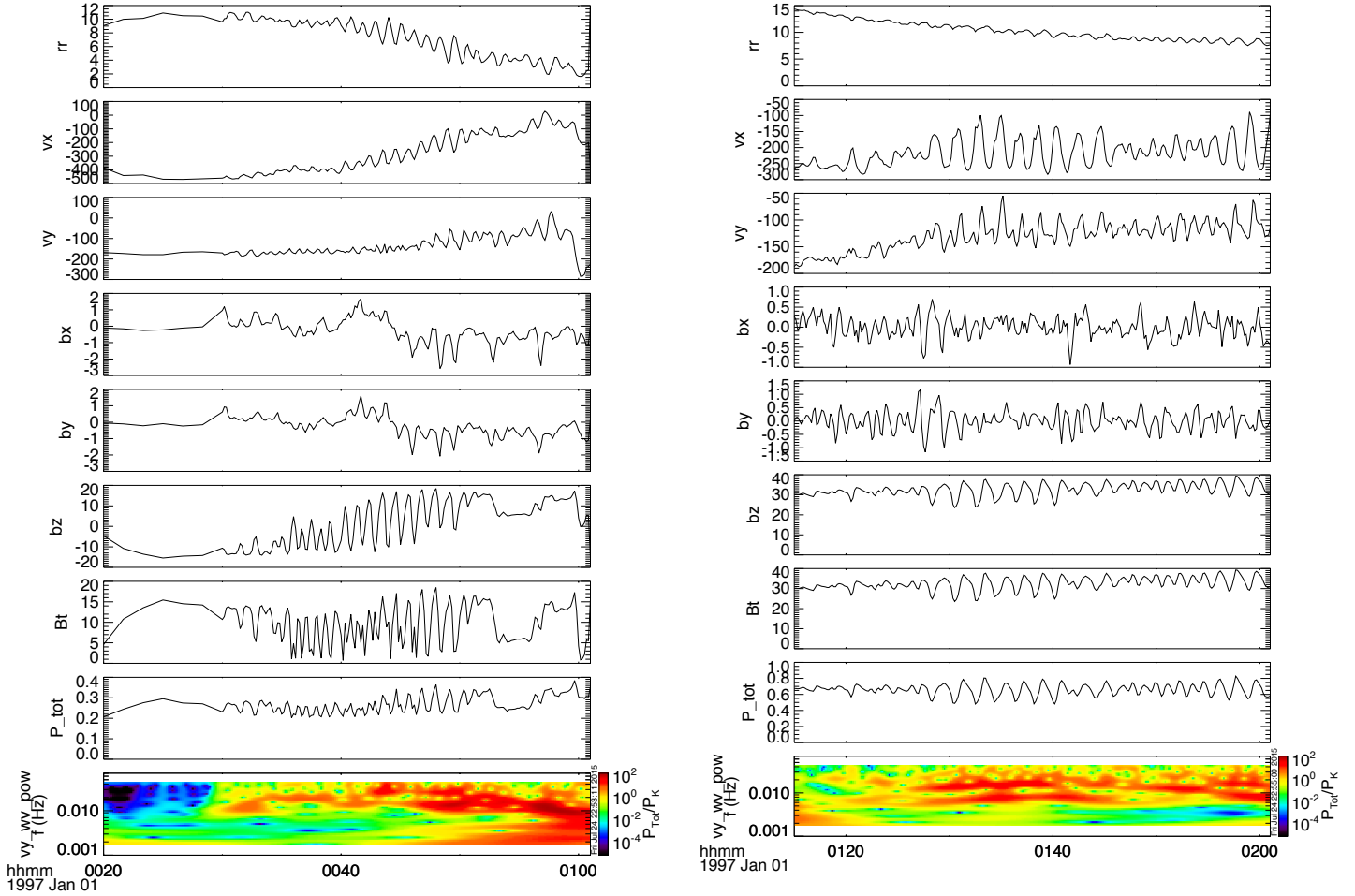


Figure 4.3: OpenGGCM simulations under constant solar wind condition at $(-10, -15.5, 0)$. Left panel is time series of simulation result under southward IMF (first hour of simulation). Right panel features the time series of simulation results under northward IMF (second hour of simulation result). From top to bottom: Ion density rr , x component of the velocity V_x , y components of the velocity V_y , x and components of magnetic field B_x and B_y , Magnetic field magnitude B_{tot} , total (magnetic plus ion) pressure, and wavelet spectrum of the y component of velocity.

In a rolled-up KH vortex the magnetospheric plasma extends into the magnetosheath plasma and becomes accelerated to speeds larger than the magnetosheath speed. This behavior of KH waves can be made visible by plotting V_x versus density. Figure 4.4 and Figure 4.5 (left panels) both show V_x versus density in a scatterplot for two different intervals, southward IMF, (first hour of simulation) and northward IMF conditions (Second hour of the simulation). Color-coded current density plot (right panels) show the characteristics of the KH waves at the equatorial plane. The blue dot shows the location of virtual spacecraft that observed the simulated KH wave or vortex.

Figure 4.4 presents the scatter plots for the waves under southward IMF (first hour of the simulation) at different stages. The top panel at the left is the scatter plot of V_x versus density generated from virtual spacecraft observations of the simulated KH wave located at (3, -8, 0) Re. The figure shows the profile expected for KH waves in linear stage. The bottom panel at the left is also a scatter plot for southward IMF generated from virtual spacecraft observation located further dawn at the magnetopause at (-10, -15.5, 0) Re where the KH waves are expected to develop into the vortices. As illustrated in the plot, there is no low-density plasma profile flowing faster than magnetosheath plasma. This might imply that KH waves under southward IMF in our simulation have not grown to the vortices. This V_x -N profile also shows another unusual behavior of the KH waves under southward IMF. However, the absence of rolled-up vortices signatures in the KH wave simulation for southward IMF might be related to simulation resolutions.

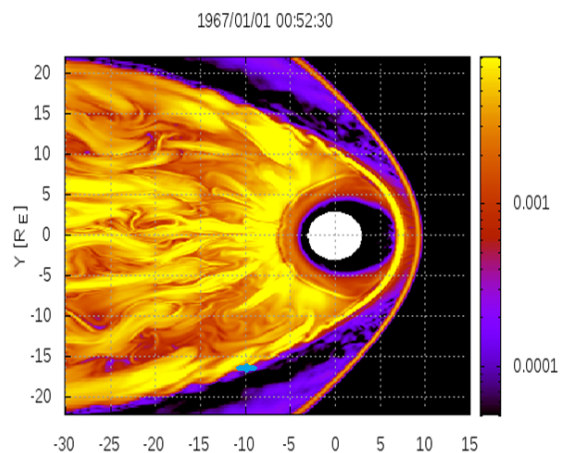
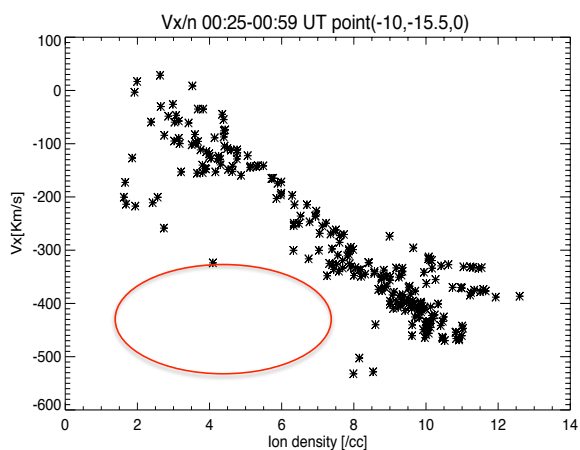
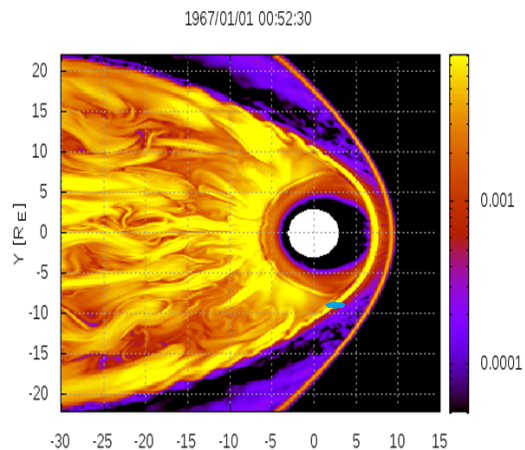
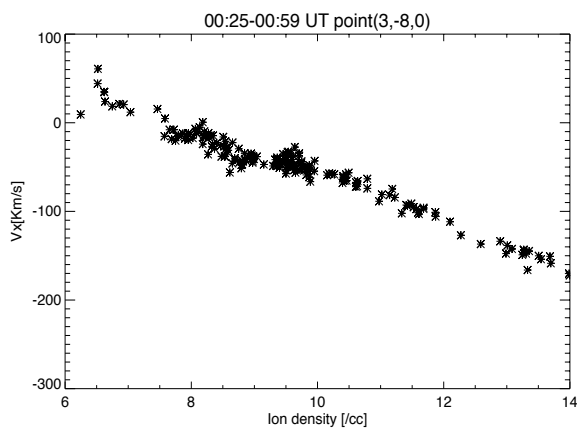


Figure 4.4: Scatterplots of the velocity V_X versus plasma density N from OpenGGCM simulation for southward IMF on the left and color-coded current density plots on the right. The blue dot in color-coded current density plots on the right shows the location of virtual spacecraft. The top left scatterplot confirms that the simulated KH waves are in linear stage. The bottom left scatterplot shows no low-density magnetospheric plasma, indicated by the red ellipse flowing faster than magnetosheath plasma.

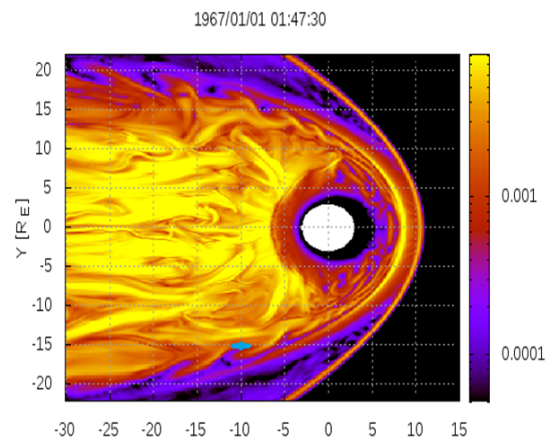
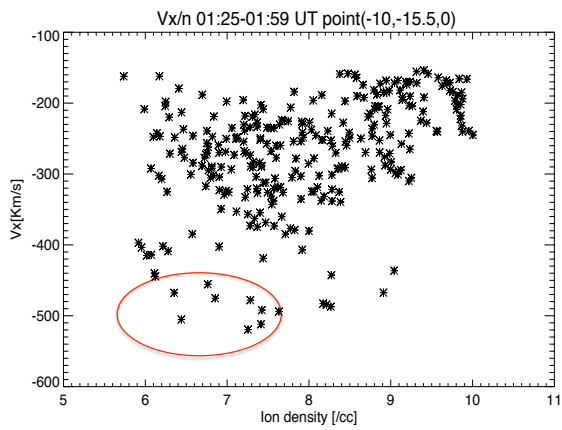
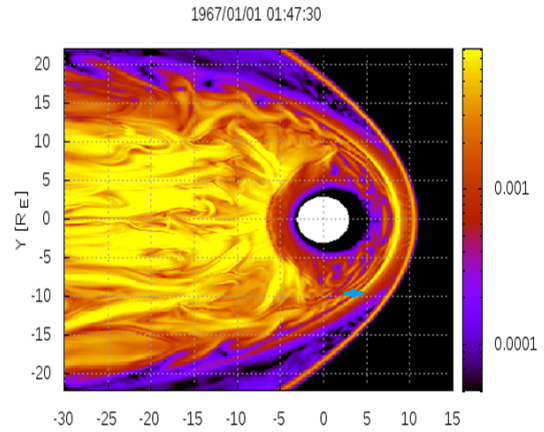
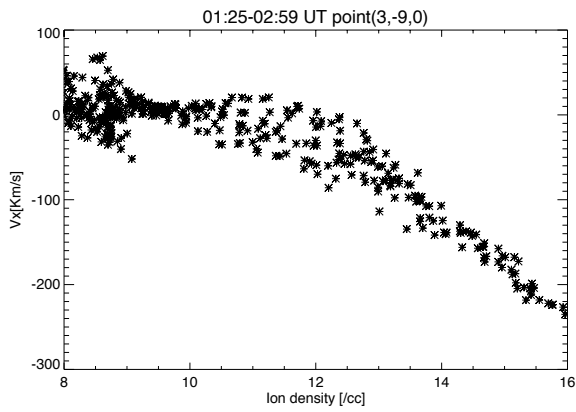


Figure 4.5: Scatterplots of the velocity V_x versus plasma density N from OpenGGCM simulation for northward IMF on the left and color-coded current density plots on the right. The blue dot in color-coded current density plots on the right shows the location of virtual spacecraft. The top left scatterplot confirms that the simulated KH waves are in linear stage. The bottom left scatterplot confirms that a fraction of the low-density magnetospheric plasma indicated by the red ellipse flows faster than magnetosheath plasma.

Figure 4.5 presents the scatterplots for the waves under northward IMF (second hour in simulation) for different locations at the magnetopause shown with the blue dot in color-coded current density plots (right panels). The top plot at the left is the V_x versus density scatterplot for the KH under northward IMF at (3, -9, 0) where the wave just began to form. The plot confirms the pattern expected for KH waves in linear stage. The bottom panel is also scatter plot for northward IMF simulation data for a point further dawn at the magnetopause (-10, -15.5, 0). This plot shows that a fraction of low-density plasma ($<8 \text{ cm}^{-3}$) flows approximately faster than the magnetosheath plasma, confirming that the KH waves developed into the rolled-up vortices.

4.3.2 Effect of magnetic field magnitude

Figure 4.6 presents the time series of simulation result for northward IMF (last two hour of the run) generated from virtual spacecraft observations located at the point (-10, -15.5, 0). The figure compares the second interval of simulation (01:20-02:00 UT) for northward IMF and $|B|=5 \text{ nT}$ with the third interval of the simulation (02:00-03:00 UT) for northward IMF but with increased magnetic field magnitude $|B|=10 \text{ nT}$. The figure shows periodic, regular oscillations in ion density n , x and y components of the velocity V_x and V_y , x and y components of magnetic field B_x and B_y , magnetic field magnitude, B_{tot} , and total (magnetic plus ion) pressure for both intervals. The wavelet spectrum of the y component of velocity V_y shows that the frequency of the waves is slightly increased during the interval with $|B|=10 \text{ nT}$. For northward IMF and $|B|=5 \text{ nT}$ (01:20-02:00 UT) the frequency of the waves is 0.008 Hz and for northward IMF with $|B|=10 \text{ nT}$ (02:00-03:00 UT) the frequency of the waves is 0.009 Hz. The amplitude of KH waves also have increased during 02:00-03:00 UT. During this interval which, the magnetic field magnitude

has been increased by a factor of two while holding the other solar wind parameters constant, the signatures of the KH waves also changed. More evident bipolar signatures in B_y , and larger oscillations in total pressure and velocity V_y , all together shows larger and more-developed KH vortices. Based on the signatures and larger amplitude waves it can be concluded that increasing the magnetic field magnitude for northward IMF condition increases the growth rate of KH instability.

Figure 4.7 shows scatterplots for KH waves for both northward IMF intervals. The left panel is a scatterplot for KH waves under northward IMF and $|B|=5$ nT, and the right panel is for KH waves under northward IMF and $|B|=10$ nT. The figure confirms the fact that the perpendicular magnetic field has a destabilizing effect and the growth rate of KH waves under northward IMF increases by increasing the magnetic field magnitude. Although, both panels show that a fraction of the low-density magnetospheric plasma indicated by the red ellipse flows faster than magnetosheath plasma and the KH waves are in nonlinear stage, the scatterplot for KH waves under stronger $|B|$, right panel, presents more low-density plasma flowing faster than magnetosheath plasma. This indicates that KH waves under stronger magnetic field magnitudes grow further into rolled-up vortices. This result might be ascribed to the $\mathbf{J} \times \mathbf{B}$ force due to increasing the magnetic field magnitude, which causes the accelerated flow in magnetosheath. The increased magnetosheath velocity cause by $\mathbf{J} \times \mathbf{B}$ force may explain the higher growth rate and destabilizing effect of the magnetic field magnitude. These results agree qualitatively with the theoretical studies obtained by Fejer (1964) and Miura et al. (1982) who showed that in a compressible flow a perpendicular magnetic field tends to be destabilizing. “Compressibility always reduces the stabilizing effect of the magnetic field” Fejer (1964).

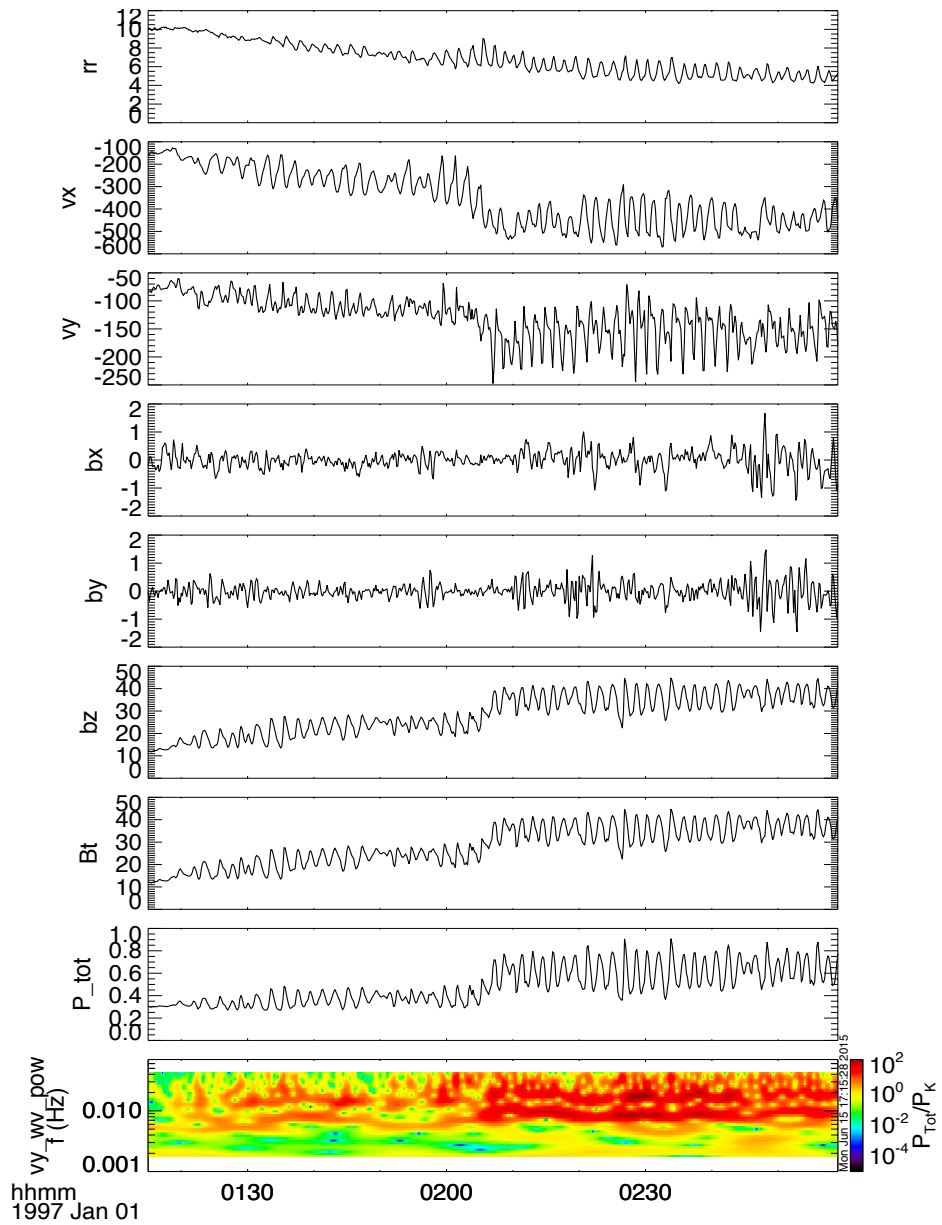


Figure 4.6: Time series of OpenGGCM simulations for northward IMF at $(-10,-15.5,0)$. The 01:20-02:00 interval is for magnetic field magnitude $|B|=5$ nT. The second interval 02:00-03:00 is for $|B|=10$ nT.

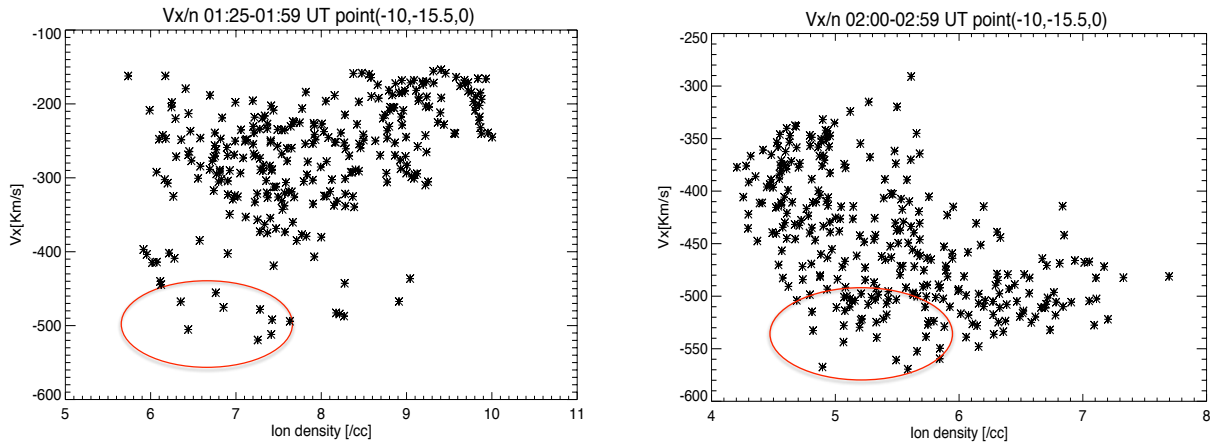


Figure 4.7: Scatter plots of the velocity V_X versus plasma density N for OpenGGCM simulation for northward IMF intervals. The left panel is a scatterplot for KH waves for northward IMF and $|B|=5$ nT (second hour in simulation) and the scatterplots on the right is for KH waves for northward IMF and $|B|=10$ nT. (Third hour in simulation). Both panels confirm that a fraction of the low-density magnetospheric plasma indicated by the red ellipse flows faster than magnetosheath plasma. The KH waves are in nonlinear stage.

4.3.3 Effect of boundary layer thickness

The linear hydromagnetic theory performed an instability analysis in idealized incompressible plasma with no boundary layer thickness, which is not true in the real magnetosphere boundary. Therefore, the more realistic case is when we consider the boundary layer thickness and compressibility of the magnetosphere in the theoretical analysis. As was mentioned in Chapter 1, the KH theory of Walker (1981) included a boundary layer of finite thickness and the compressibility of plasmas. He showed that when the wavelength of the disturbances became comparable with the thickness of the boundary layer, the instability was quenched. This implied that there is a particular wavelength for the fastest growing mode, and a particular frequency for the fastest growing mode ($f=V\rho/\lambda$). Consequently, the monochromatic

nature of the waves is an outcome of the presence of a boundary layer. From wavelength spectrum analysis as has been shown in the last panel in Figure 4.1 and Figure 4.2, the waves in our simulations are monochromatic. This implies the presence of thickness in our simulated magnetosphere boundary, which is demonstrated in Figure 4.8 for three different intervals: southward IMF, northward, and northward with increased magnetic field magnitude. The V_x versus Y plot in the GSM coordinate shows how the x component of plasma velocity changes along its perpendicular direction. Figure 4.8 from top to bottom display simulation boundary layer for southward IMF, northward IMF, and northward IMF with stronger magnetic field magnitude. The solid vertical line shows the location of the magnetopause. The vertical dashed line indicates the point where the velocity V_x transitions from positive to negative values. This is the location of the Inner Edge of Boundary Layer (IEBL). The distance between these two vertical lines is the simulation boundary layer thickness (d) shown by the black arrow. As shown in Figure 4.8 in top panel, the boundary layer for southward IMF is thin, and the V_x - Y profile shows a sharp transition between the magnetosphere and the magnetopause. The thickness of the boundary layer is approximately 1.1 R_e under southward IMF. The middle panel is for northward IMF and $|B| = 5$ nT. The V_x - Y profile shows a thicker boundary layer. The thickness of the boundary layer is approximately 1.5 R_e . The bottom panel is for northward IMF condition with increased magnetic field magnitude $|B| = 10$ nT. The plot shows the thickness of simulated boundary layer is approximately 1.0 R_e . The thickness of simulated boundary layer decreases by increasing the magnetic field magnitude.

The horizontal blue solid line shows the magnetosheath velocity for each simulation interval. Top panel shows the magnetosheath velocity for simulation under southward IMF is

approximately 400 km/s. The middle panel shows the magnetosheath velocity for northward IMF interval with $B=5$ nT is also approximately 400 km/s. The magnetosheath velocity in the bottom panel is about 500 km/s. This panel is for northward IMF interval with $B=10$ nT. This result confirms that increasing magnetic field magnitude causes a $J \times B$ force which lead to increase the magnetosheath velocity. The increased KH growth rate under stronger magnetic field magnitude may be result of the increased magnetosheath velocity. The accelerated flow caused by $J \times B$ force may also explain the bumps shown in IEBL and magnetopause boundary layer in bottom panel. These bumps can be related to the more developed vortices under this condition. Since it shows plasma flowing faster than magnetosheath plasma, which is the signature of rolled up vortices.

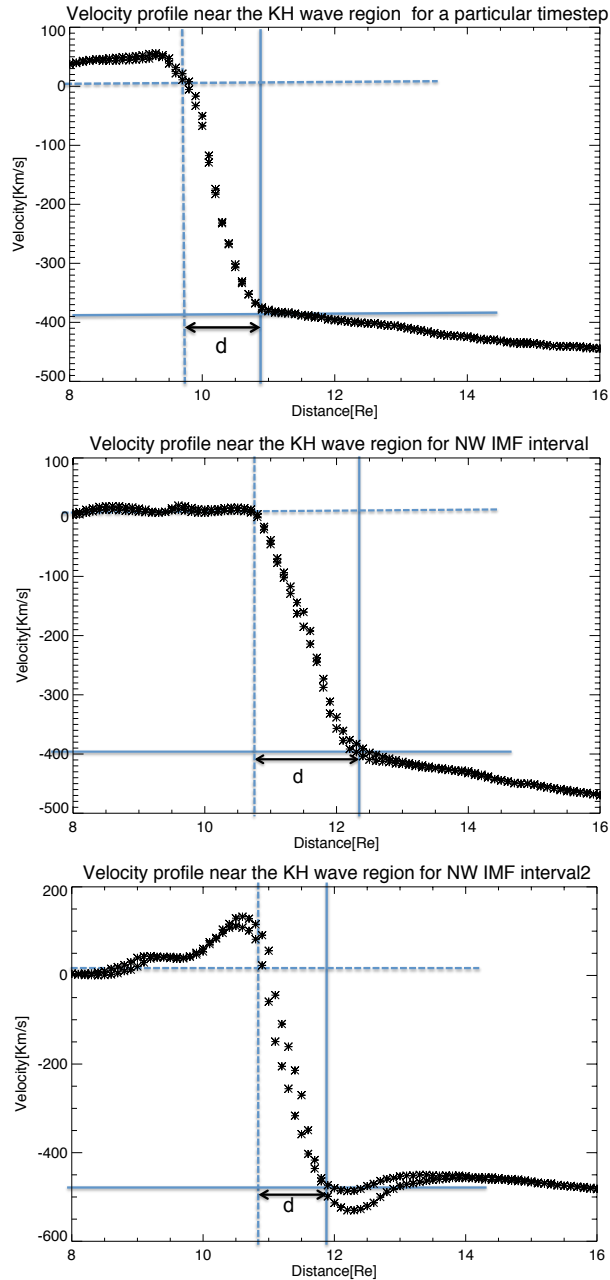


Figure 4.8: Velocity profile V_X -Y near the KH wave region for the OpenGGCM simulation. The top panel is from simulation results under southward IMF, the middle panel is for simulation result under northward IMF ($|B|=5$ nT) and the bottom panel is for simulation result under northward IMF ($|B|=10$ nT). The vertical dashed line is the location of the IEBL while the vertical solid line is the location of the magnetopause. The region between these two lines, d , is the simulation boundary layer.

4.3.4 Effect of numerical resolution

Resolution is important for numerical modeling. Spatial resolution specifies how large the grid cells in a model can be. Temporal resolution refers to the size of the time steps used in models which means that how often (in simulated or "model time") calculations of the various properties being modeled are conducted. Increasing spatial resolution means that more cells cover Earth's magnetosphere. Higher resolution models provide much more accurate and detailed information about the process being studied, although these take a much longer time to compute. While the details of the numerical techniques in the OpenGGCM simulation are beyond the scope of this thesis, there are some key aspects of the numerical techniques used in the OpenGGCM model which are indeed important and affect the simulation results such as spatial resolutions (the size and shape of cells within the grid). The OpenGGCM model has a stretched Cartesian grid as shown in the bottom panel of Figure 4.9. As previously mentioned in simulation studies (Claudepierre et al. 2008; Li et al., 2013) the simulation resolution and size of grids are crucial for studying the KH instability and the KH wave is sensitive to grid spacing. The grid resolution must be sufficient to resolve the boundary layer thickness. The low resolution in the numerical study of KH instability also might cause the waves start to form further away from the magnetopause. The reason is that the waves have to travel along the magnetopause some distance before they can grow to a sufficient size capable of being resolved in the simulation. Therefore, the simulation that has been discussed in this chapter has a high-resolution of $600 \times 400 \times 300$ grid points with a minimal grid spacing of $0.07 R_e$. The grid spacing of $0.07 R_e$ is small enough to identify the small displacement of the waveforms at the dayside magnetopause.

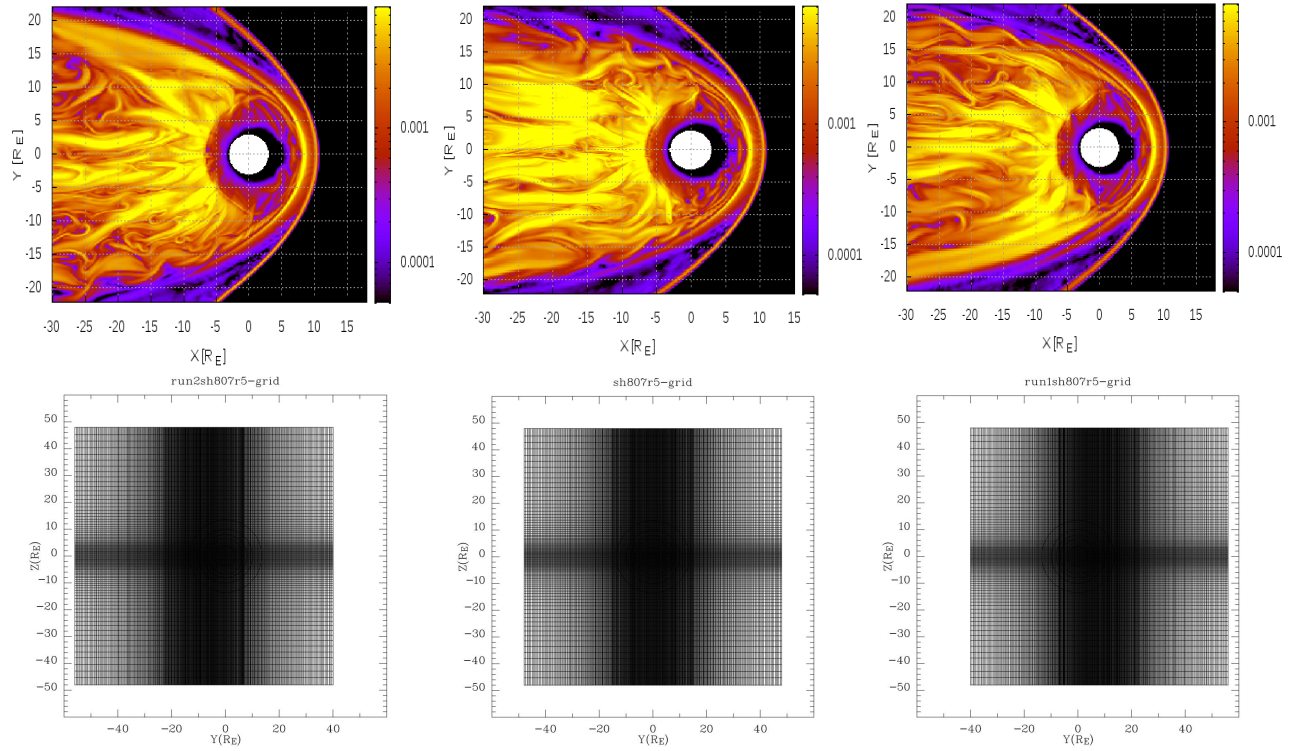


Figure 4.9: Color-coded current density plots from OpenGGCM simulation. The color-coding shows the current density in the equatorial plane. The plots on the left panel related to simulation with reduced resolution with center of grids shifted to dawn. The plots on the middle panel related to simulation with resolution with high resolution not center shifted. The plots on the right panel related to simulation with reduced resolution and center of grids shifted to dusk.

Figure 4.9 shows the result of OpenGGCM simulation with the same solar wind input data used in the generic simulation discussed in previous sections. However, the high-resolution part of the stretched Cartesian grid, the center, is shifted to the estimated location of the magnetopause to dawn side (left panel) and dusk side (right panel). The plots at the top panel show color-coded current density plots under northward IMF conditions, and the plots at the bottom panel show the simulation grid in xz direction for each simulation. The top plot on the left is from the simulation when the center of the stretched Cartesian grid shifted 8 R_E downside

(bottom plot on the left). It shows that KH waves are generated only in the high-resolution part of simulated magnetosphere boundary, which means at the downside magnetopause. The top plot in the middle shows the simulation results under northward IMF when the center of the stretched Cartesian grid has not shifted and the high-resolution region is located at the center of the plot. The plot shows KH waves at both side of magnetosphere boundary, dawn and dusk magnetopause, since high-resolution region of magnetosphere boundary is at $Y (-17, 17)$ as shown in the middle plot at the bottom panel. The top plot on the right is for the simulation when the center of the stretched Cartesian grid is shifted $8 R_e$ duskside. Therefore, the high-resolution region of magnetosphere boundary is at $Y (-9, 25)$ as shown in the right plot at the bottom panel. It shows KH waves are only generated at the dusk flank magnetopause (high-resolution region). The plots in figure 4.9 show that the KH wave is sensitive to grid spacing in OpenGGCM simulations.

4.4 Event study: THEMIS Observations

Using actual satellite measurements as the input for OpenGGCM simulation is called event study. In this section we present the OpenGGCM Simulations for a THEMIS observations on 07 June 2014. This helps us to check whether or not the OpenGGCM reproduces the observed KH waves signatures.

4.4.1 THEMIS Observations on 07/06/2014

THEMIS observed a series of surface waves near dawn flank magnetopause on 7th Jun 2014. Figure 4.10 shows Geotail observations of solar wind parameters for the event. The Geotail data has not been time shifted and the figure 4.10 shows approximately 15 minutes delay. The wavelet spectrum of the density and velocity in figure 4.10 during the event interval (is shown with red vertical dashed lines) indicates that there were no significant solar wind dynamic pressure variations before or during the event. Figure 4.11 shows an example of a KH event observed by THEMIS E under both southward and northward IMF conditions. THEMIS observed quasi-periodic fluctuations during the interval 22:35-23:50 UT. The solar wind is under southward IMF during 2235-2315 UT, and turned northward around 2315 UT as shown in Figure 4.10. THEMIS moved from (3.3, -9.9,3.3) to (3.8, -10,3.4) during this interval, i.e., it crossed the magnetopause about 3 R_E sunward of the dawn terminator. As shown in Figure 4.11, the characteristics of the fluctuations changed from the 2245-2258 UT to the 2258-2315, finally changing again during 2325-2350 UT interval. This event is unique. It presents three different processes: FTEs, KH waves under southward and northward IMF.

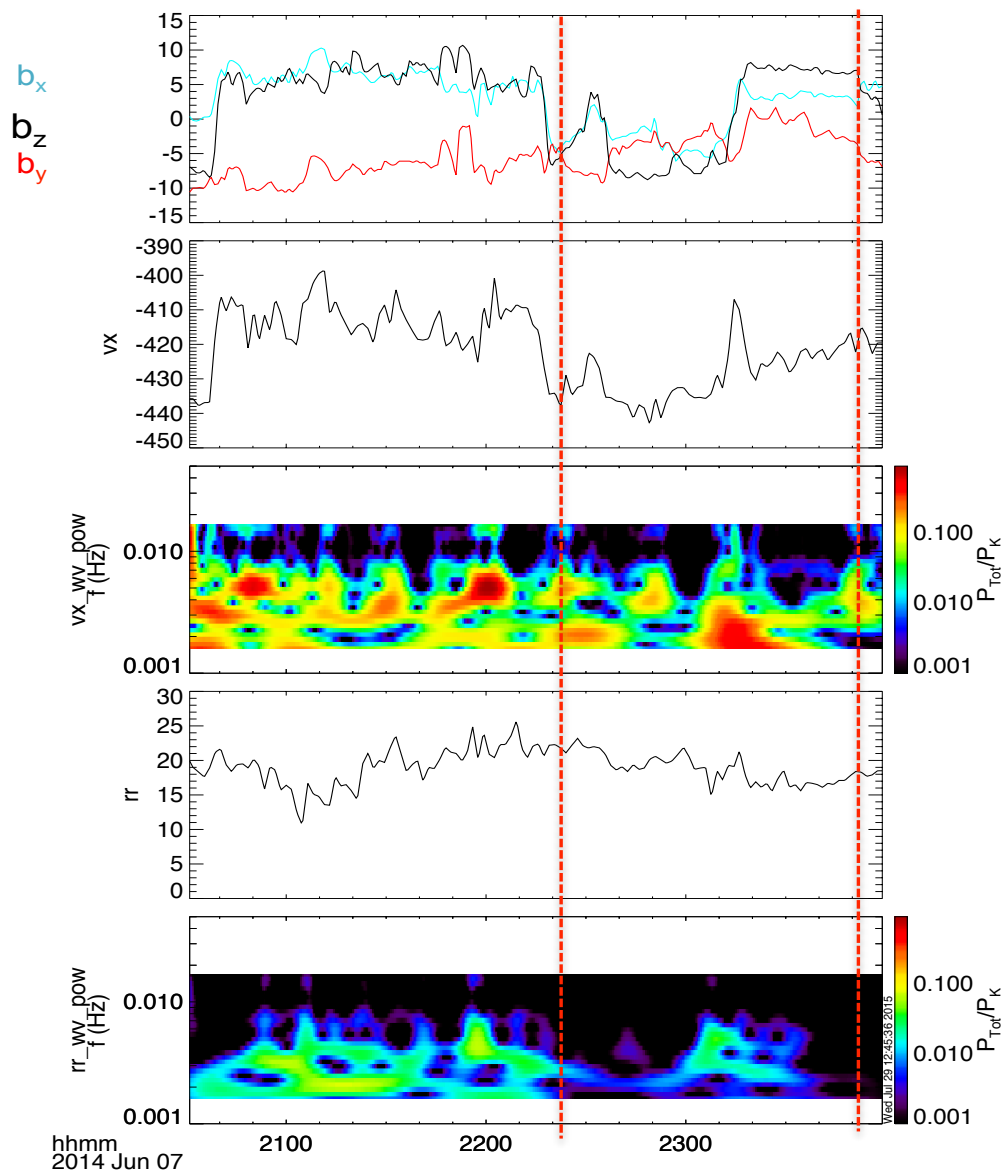


Figure 4.10: Geotail observations of solar wind parameters on 7 June 2014. From top to bottom: magnetic field components by (red), b_x (blue), b_z (black, X component of the velocity V_x , (c) wavelet spectrum of V_x , n_r density, and wavelet spectrum of the density, n_r . The red vertical dashed lines show the event interval.

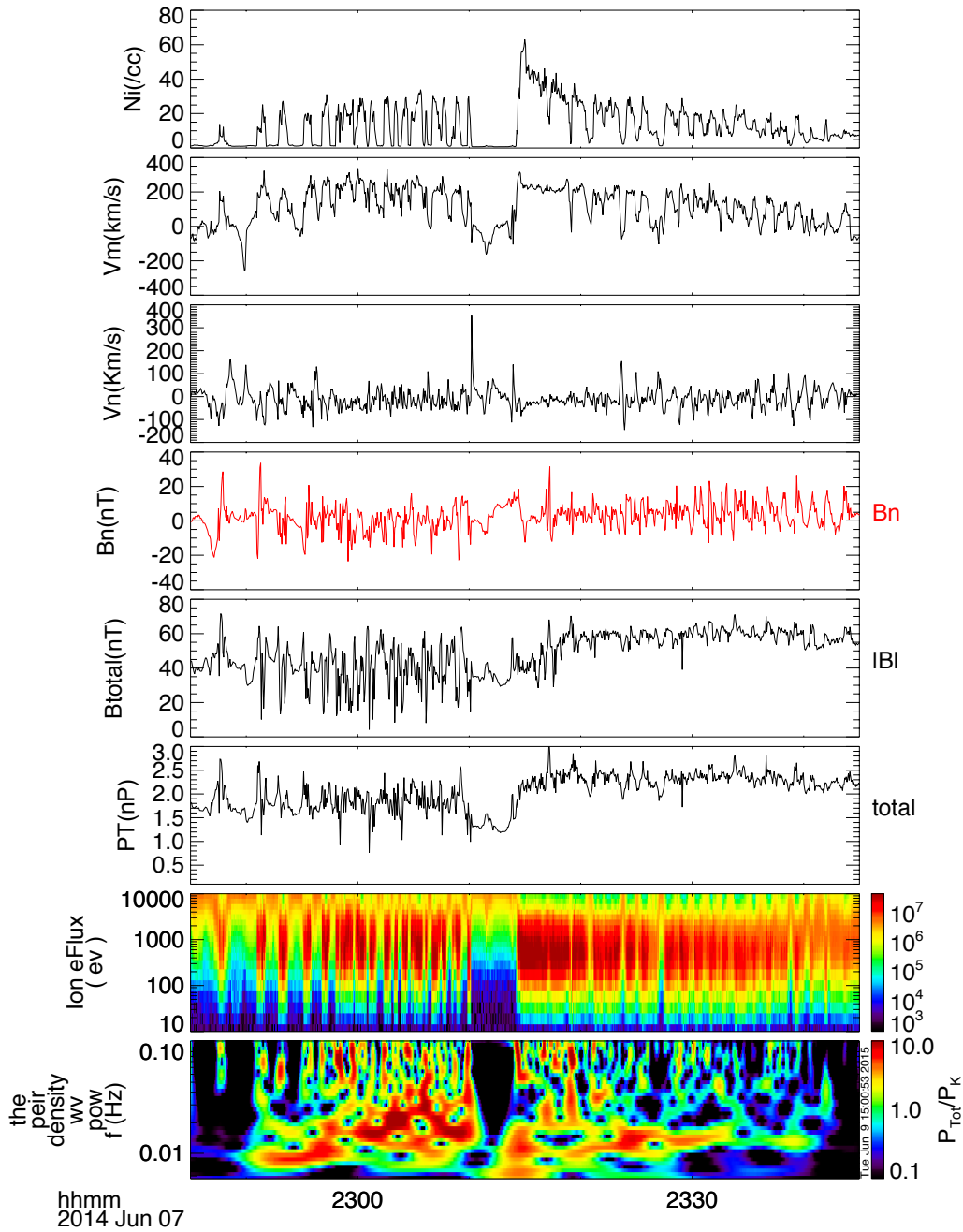


Figure 4.11: THEMIS E observations on 7 June 2014. From top to bottom: (a) Ion density, (b) M component of the velocity V_m , (c) N components of the velocity V_n , (d) N components of magnetic field B_N , (e) Magnetic field magnitude B_{total} , (f) total (magnetic plus ion) pressure, (g) Omni-directional ion energy flux, and (h) wavelet spectrum of density.

We can see clear differences in the signatures for these three intervals as shown in Figure 4.11. During the first sub interval the fluctuations are separated by several minutes of quiet, while the second part of the event is characterized by continuous fluctuations and shorter periods. The first part of the event clearly consists of FTEs; it also has all the other FTE signatures listed in Chapter 2. The second part shows irregular and high frequency oscillations of density, Velocity, magnetic field component and total pressure. This interval 2258-2315 shows KH wave signatures under southward IMF. The last interval 2325-2350 demonstrates the periodic and regular oscillations in density, velocity, magnetic field component, and total pressure. During this interval solar wind is under northward IMF. We can see from this data that the signatures of the KH waves under northward IMF are different than under southward IMF (second interval). Additionally, we are able to compare our simulation results during southward and northward IMF (idealized, constant solar wind) presented in the previous section with THEMIS observations (real data). The results are consistent with our OpenGGCM simulation results with idealized solar wind input, which exhibit different signatures for KH waves under southward and northward IMF condition.

4.4.2 OpenGGCM simulation of THEMIS Observations

The result of OpenGGCM Simulation that models the THEMIS event on 7th June 2014 shows the surface waves similar to spacecraft observations. To test whether the observed magnetopause motions are from KH waves or driven by fluctuations in the solar wind dynamic pressure, we conducted two runs for the event, one with the real solar wind condition, and one by keeping the solar wind density and the velocity constant. We have also used high-resolution OpenGGCM

simulations $975 \times 702 \times 340$. Characteristics of the waves remain unchanged during the run with constant solar wind density and the velocity. This assures us that the waves are not generated by fluctuations of solar wind dynamic pressure. Figure 4.12 compares the simulation results on the left panel with THEMIS observations on the right panel. The figure shows how reasonably OpenGGCM produced the three different processes: FTEs, KH waves under southward, and KH waves under northward, similar to THEMIS observations although the frequency is somewhat lower. To simulate the event with wave characteristics approximately similar to observations, we needed to increase the resolution. The wavelet spectrum of density from THEMIS observations (right panel in figure 4.12) and wavelet spectrum of the y component of velocity from OpenGGCM simulation (left panel in figure 4.12) shows that in both THEMIS data and simulation, KH frequency is higher for southward IMF as compared to northward IMF. This result is in good agreement with generic simulation results presented in the first part of this chapter.

Figure 4.13 compares the scatter plots of the ion velocity V_x versus ion density for both OpenGGCM and THEMIS observations to see how OpenGGCM produce the KH waves growth rates. The plots in the top panel compare the scatterplot of OpenGGCM results on the left with the scatterplot of THEMIS data on the right for KH waves under southward IMF (2258-2315 UT). The scatterplots show approximately identical V_x -N profile for both OpenGGCM simulation and THEMIS observation. The plots in the bottom panel compare the scatterplot of OpenGGCM results on the left with the scatterplot of THEMIS data on the right for the KH waves under northward IMF (2320-2345 UT). The simulation and the observation both shows

that the waves under northward IMF have not yet developed into vortices and is in linear stage. Figure 4.13 confirms that the KH waves reproduced by OpenGGCM are in very good agreement with in suit observations.

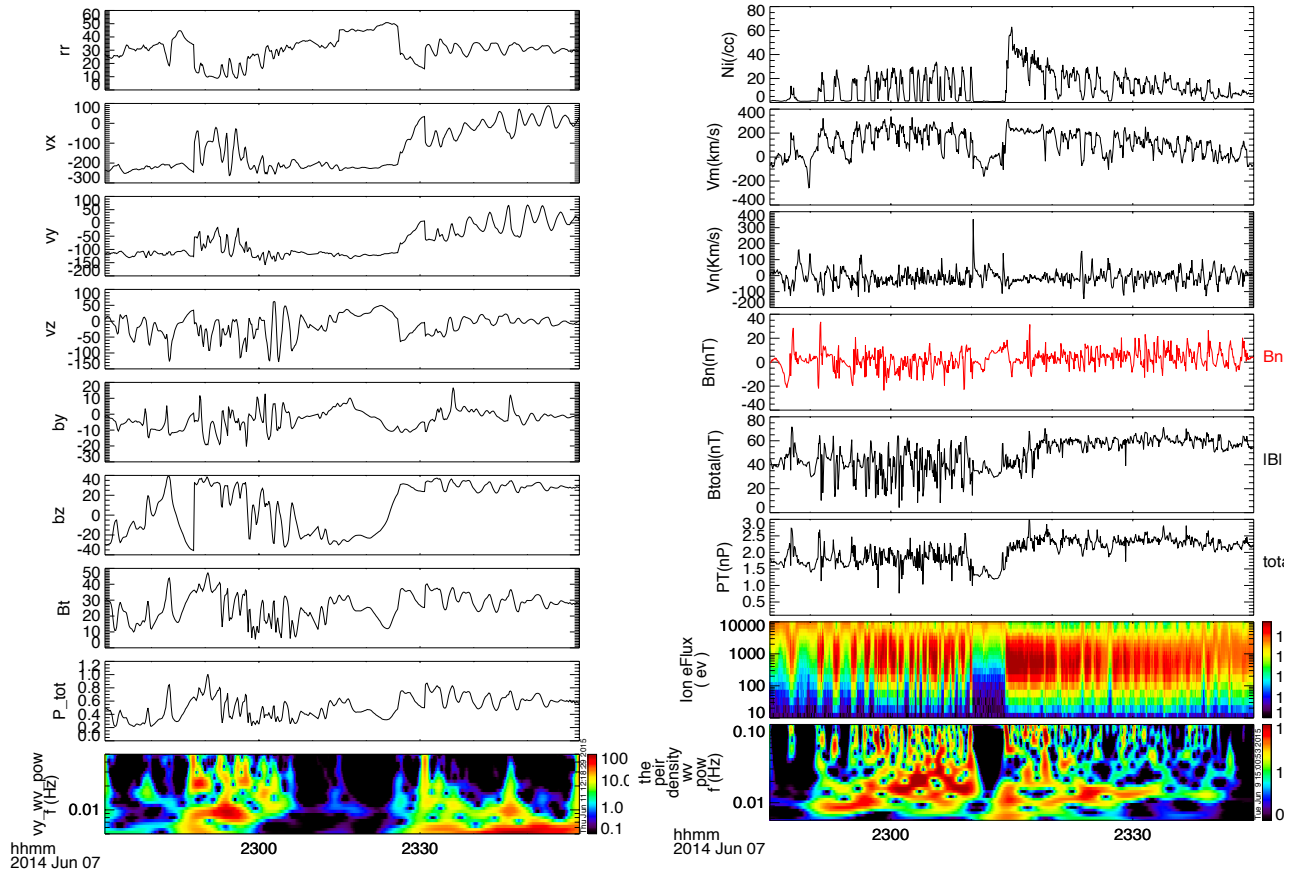


Figure 4.12: A comparison of THEMIS observations with OpenGGCM simulation. On 7 June 2014. Left panel is OpenGGCM result: From top to bottom: Ion density rr , x component of the velocity V_x , y components of the velocity V_y , x and components of magnetic field B_x and B_y , Magnetic field magnitude B_{tot} , total (magnetic plus ion) pressure, and wavelet spectrum of the y component of velocity. Right panel are THEMIS observations. From top to bottom: (a) Ion density, (b) M component of the velocity V_m , (c) N components of the velocity V_n , (d) N component of magnetic field B_n , (e) Magnetic field magnitude B_{tot} , (f) total (magnetic plus ion) pressure, (g) ion energy flux, and (h) wavelet spectrum of density.

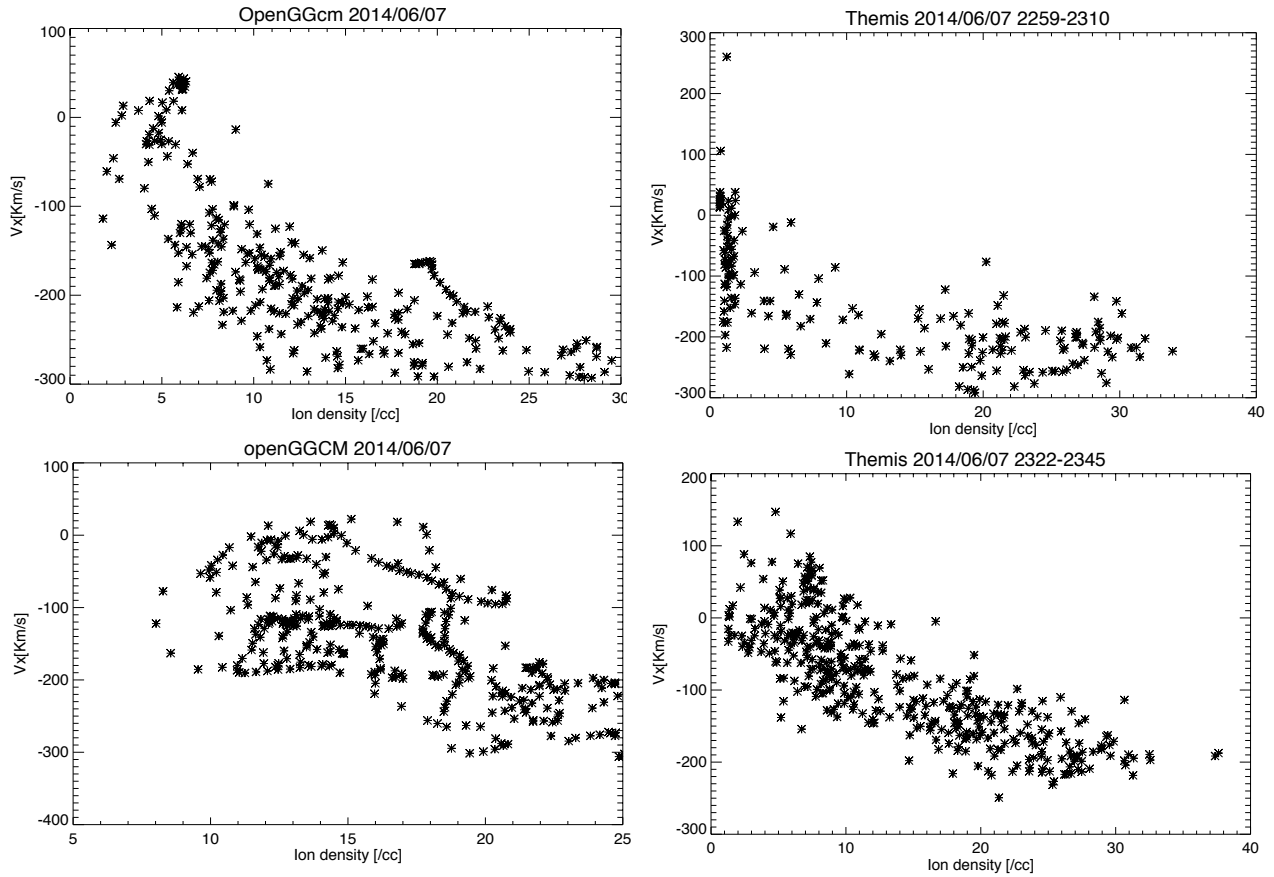


Figure 4.13: A comparison of THEMIS observations with OpenGGCM simulation. Scatter plot of the ion velocity V_x versus ion density. The plots on the left panel are for OpenGGCM simulations.

Figure 4.14 depicts the OpenGGCM simulation of event observed by THEMIS on 7 June 2014 as color-coded current density plots in the equatorial plane. Starting from the top left, the first plot shows typical FTEs; the two next panels show the evolution of FTEs in time. The three plots in the middle panel illustrate the time evolution of KH under southward IMF. The first panel in the bottom left shows KH waves under northward IMF, and the next two panels to the right show the evolution of waves in time under northward IMF.

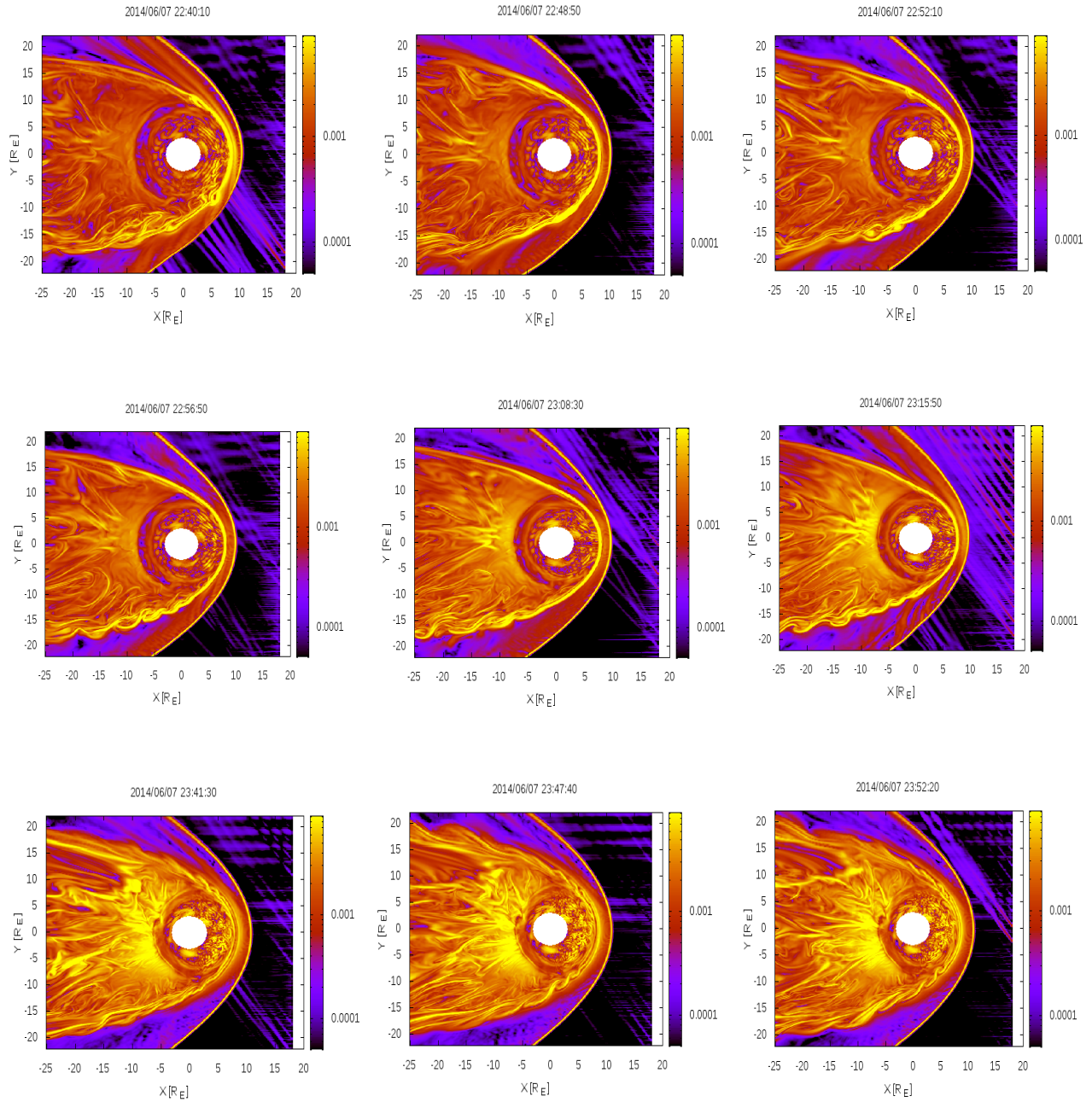


Figure 4.14: OpenGGCM simulation of event observed by THEMIS on 7, June 2014 shown in Figure 4.9. The color-coding shows the current density in the equatorial plane.

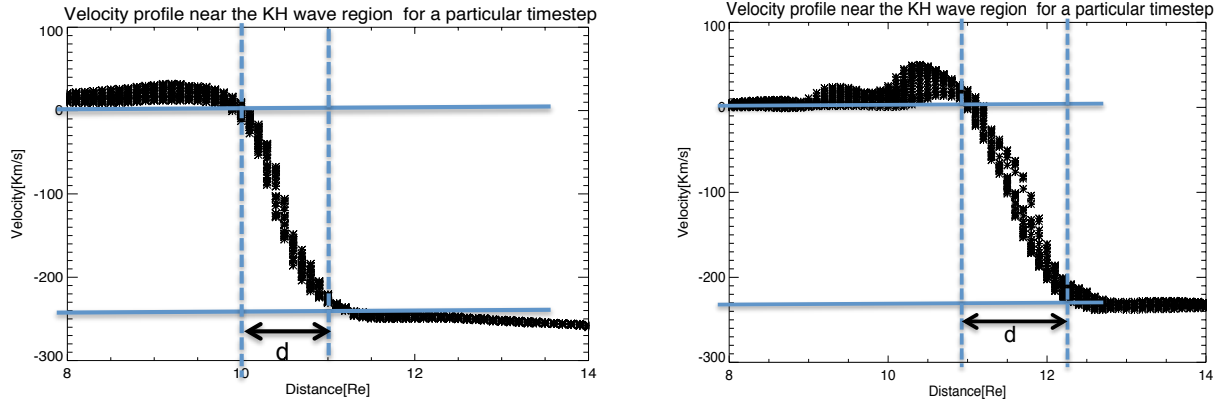


Figure 4.15: Velocity profile near the KH wave region for a particular timestep for the OpenGGCM simulation of THEMIS event for two different intervals: The left plot simulated boundary layer under southward IMF. The right plot is simulated boundary layer under northward IMF. The region between these two vertical dashed lines, d , is the simulation boundary layer.

Figure 4.15 shows a comparison of simulated boundary layer for the last two intervals of THEMIS observations: KH waves under southward (The left panel) and KH under northward IMF (right panel). The thickness of boundary layer is approximately 1.0 Re under southward IMF and the thickness of boundary layer is approximately 1.25 Re under northward IMF. These results indicate that the simulated boundary layer for KH under southward is thinner than the simulated boundary layer under northward IMF. This is also consistent with the simulation results for idealized constant solar wind conditions under southward and northward IMF.

4.5 Discussion and conclusions

By using a three-dimensional global MHD simulation of the Earth's magnetosphere, OpenGGCM, we have studied the properties and signatures of the waves for different IMF conditions. The simulation results for KH waves under constant solar wind parameters show KH waves under southward IMF behave quite differently than the waves under northward IMF. These differences are shown to exist in both properties and signatures of the waves: properties such as frequency, wavelength, amplitude, and the growth rate and signatures of the KH waves such as magnetic field and velocity profiles.

KH waves during southward IMF are higher frequency than KH waves under northward IMF. High frequency waves for southward IMF may be attributed to a thin boundary layer. Higher frequency waves according to $(f=V\rho/\lambda)$ by assuming that $V\rho$, Phase velocity, is constant would have smaller wavelengths. The KH waves under southward IMF in our results demonstrate smaller wavelengths than the KH waves under northward IMF. Another feature of KH waves, which is investigated in this study, is the phase of the KH wave growth. The V_X -N method has been used to identify the phase of the KH wave growth in our simulations. These results suggest that the KH waves under southward IMF do not grow sufficiently to rolled-up vortices, and that the growth rate for northward IMF is higher than that for southward IMF. This might be related to the thin boundary layer for southward IMF. Because, the thickness of boundary layer must be larger than grid spacing to be capable of resolving the instability and allow the wavelength to grow.

The effect of the magnitude of the magnetic field under pure northward IMF conditions is also investigated. The results show that increasing the magnitude of the magnetic field when it lies northward enhances the KH growth rate. This is consistent with the results reported by Fejer (1964), Ong and Roderick (1972), and Miura and Pritchett (1982).

We have also conducted the OpenGGCM simulation of an event on 7 June 2014 observed by THEMIS. During the June 7, 2014 event, KH first occurred during southward IMF, then the IMF turned northward and KH waves continued. OpenGGCM reproduces the KH waves under northward and under southward conditions reasonably with similar signatures and features to these observations. The frequency is somewhat lower in simulation, which can be fixed by increasing the grid resolution. In both observation and simulation, KH under southward IMF has a higher frequency when compared to northward IMF. The simulated boundary layer is thinner during southward IMF as compared to northward IMF.

We concluded that there are many differences in wave properties (frequency, wavelength, amplitude, growth rate) as well as the wave signatures under southward and northward IMF conditions. This might explain a few in-situ observations of KH waves under southward IMF. One reason is that the signatures of KH under southward IMF are quite different than the signatures observed by the spacecraft and expected for KH waves under northward IMF. This means that even if the KH waves under southward IMF have been observed, they have not been suitable for reporting or publication. The second reason might be related to the properties of the KH waves under southward IMF, which have small wavelengths and amplitudes. In general, the probability of detecting large waves is higher than detecting the small waves. Even if the

spacecraft could detect the small waves, any small movement of the spacecraft will terminate the detection of the waves. This could explain the short duration of observed KH waves under southward IMF in our THEMIS survey as well as the other two reported KH waves under southward IMF (Hwang et al. 2011, Yan et al. 2014).

Chapter 5

Discussion and Future Work

5.1 Discussion and Conclusions

In this thesis, we have conducted a survey of THEMIS data to create a database of magnetopause crossings throughout the entire mission. We surveyed data from 2007 to 2013, when the THEMIS spacecraft frequently crossed the magnetopause during the dawn and dusk orbital phases. We examined the plasma and magnetic field data to catalogue magnetopause crossings for the purpose of identifying KH waves. We find that about half of the crossings show waves or quasi-periodic variations, but not all of them are KH waves. Often, such periodic or quasi-periodic structures seem to be caused by dynamic pressure variations in the solar wind or magnetosheath and non-steady magnetopause reconnection or Flux Transfer Events (FTEs). We thus needed to differentiate all magnetopause wave observations against FTEs and buffeting of the magnetosphere by the solar wind. Our analysis method using very conservative criteria to positively identify KH waves has been discussed in Chapter 2. The primary goal of this chapter was to describe our methods to distinguish between FTEs signatures and KH wave signatures from single spacecraft observations.

The statistical results of our KH and magnetopause crossings database are discussed in Chapter 3. This statistical analysis showed that KH waves at the Earth's magnetopause occur ~19% of the time regardless of the solar wind conditions. We found that the KH waves occurrence rate increases with solar wind speed, Alfvén Mach number, and number density, while remaining mostly independent of IMF magnitude. These occurrence rate dependences on solar wind parameters are weak in comparison to KH wave occurrence dependences on IMF direction (clock angle).

The fact that KH occurrence rate increases with solar wind speed is as expected from the linear theory. However, there appears to be no low-speed cutoff for KH waves; KH waves are still observed at solar wind speed as low as 300 km s^{-1} . The occurrence rate increases with IMF cone angle and maximizes at zero IMF clock angle. The IMF cone angle dependence is as expected from the linear dispersion relation of KH waves which predicts that the instability maximizes when the magnetic field on either side of the shear layer is close to collinear, which occurs for $\sim 90^\circ$ cone angle. The IMF clock angle dependence indicated that the occurrence rate is ~35% for near northward IMF, near 20% if the IMF lies in the equatorial plane, and about 10% for southward IMF. Although the occurrence rate under southward IMF is surprising, it is still approximately 4 times less than the occurrence rate under northward IMF. Hwang et al. (2011) suggested that KH waves under southward IMF are irregular and temporally intermittent due to dynamically active sub solar behavior. This may explain the preferential in-situ detection of KH waves when the IMF is northward, because the irregular and short structures are less likely identified as KH waves than the rather regular and longer KH wave trains typical for northward IMF. This explanation is also consistent with the KH instability events under

southward IMF in our database. The majority of the events during southward IMF are irregular, short and polychromatic. This chapter concludes that KH waves are much more ubiquitous and occur under most solar wind and IMF conditions and may thus be more important for plasma transport across the magnetopause than previously thought.

During our THEMIS survey we have noticed that the signatures of the KH waves are different during southward IMF than northward IMF. In order to better isolate such differences and investigate the behavior of KH waves under southward IMF we used OpenGGCM simulations in two ways: simulation with constant solar wind for purely southward and northward IMF conditions, as well as simulation of one of the KH events observed by THEMIS under both southward and northward IMF. These simulation results are discussed in Chapter 4. The results show that OpenGGCM reproduces KH waves under northward and southward conditions with approximately the same signatures as observations. KH waves under southward IMF in the simulations demonstrate irregular structures similar to KH waves under southward IMF in our database and reported by Hwang et al. (2011). The simulation results show that KH under southward IMF has higher frequency and thinner boundary when compared to northward IMF conditions. From simulation results KH waves grow into rolled-up vortices during northward IMF, while failing to do so during southward IMF. Additionally, the simulation results demonstrate smaller waves in both wavelength and amplitude in comparison with northward IMF. Also, as the magnetic field magnitude increases, the growth rate also increases. This destabilizing effect of perpendicular magnetic field on KH waves might be attributed to the accelerated flow caused by $\mathbf{J} \times \mathbf{B}$ force.

5.2 Future works

- The first and most important question than can be addressed by using our KH database is dawn-dusk asymmetry of KH waves at the flank magnetopause. Are there significant dawn-dusk asymmetries in KH wave occurrence and/or their properties such as growth rate, and plasma mixing within the vortices? A number of studies have suggested that such asymmetries exist (Walters, G. K., 1964; Huba, J. D, 1996; Walsh, B. M., et al., 2012; Taylor, M. G. G. T. et al., 2012).
- Since we have the biggest database of KH waves under southward IMF conditions (about 40 events), the second question that can be answered by our database is the differences between KH waves under southward and northward IMF conditions, which have already been discussed from simulation results in Chapter 4. This also might lead to answer why the KH wave occurrences based on observations favor under northward IMF condition while there should be no difference, according to theory.

5.2.1 Dawn-dusk asymmetry

The occurrence of the Kelvin–Helmholtz instability at the earth magnetopause may have a dawn–dusk asymmetry. One possible explanation for these dawn–dusk asymmetries is from the average orientation of the (IMF) solar wind, which follows the Parker spiral. Such a Parker spiral magnetic configuration introduces the necessary geometry for dawn–dusk asymmetries in foreshocks, magnetosheath, and magnetopause. Higher ion density in the dawn magnetosheath, higher temperature in dawn, and higher magnetic field magnitude in dusk magnetosheath was

observed through a number of studies. A study by Haaland and Gjerloev (2013) reported significant and persistent dawn–dusk asymmetries in current density (higher in dusk side magnetopause) and magnetopause thickness (thicker at a downside). Since Kelvin–Helmholtz instability is produced by velocity shear flows between the magnetosheath and the magnetosphere at the magnetopause, the dawn–dusk asymmetry in magnetosheath and magnetopause parameters such as magnetosheath ion density, magnetosheath magnetic field magnitude, and magnetopause thickness may cause a dawn–dusk asymmetry in occurrence of the Kelvin–Helmholtz instability.

The growth of the Kelvin–Helmholtz instability may also have a dawn–dusk asymmetry. If finite Larmor radius effects are taken into account, growth is favored on the dusk-side, while conditions in the magnetosheath under Parker spiral IMF conditions might favor growth on the dawn side. A statistical study of the occurrence of Kelvin–Helmholtz vortices on the flank magnetopause from Geotail data shows detection of 18 KH waves events in nonlinear stage with 9 events at dawn flank magnetopause and 9 events at dusk flank magnetopause. This suggests no particular dawn–dusk asymmetry. An extension of this study by Taylor et al. (2012), including Double Star TC-1 data, did find an asymmetry with the occurrence of Kelvin–Helmholtz vortices favored on the dusk flank magnetopause. They found that 17 events exhibited rolled-up behavior with 12 at dusk flank magnetopause.

Plasma mixing in Kelvin–Helmholtz vortices may also have a dawn–dusk asymmetry. Nishino et al. (2011) reported one observation of vortices occurring simultaneously on both flanks and showed that while their macroscopic properties were similar, differences were

observed on the microscopic level, with more plasma mixing between magnetosheath and magnetospheric populations in the downside vortex than the dusk-side vortex. The dawn-dusk asymmetry of occurrence and growth of Kelvin–Helmholtz waves might be different under southward and northward IMF conditions.

Nonetheless, all these results were based on numerical studies or observational studies that were limited to a few events. Moreover, their results are also contradictory, and the causes for such asymmetry are still speculative. To fully explore the dawn-dusk asymmetry, at least one-year of observational dataset would be needed. We have already built a comprehensive database of THEMIS KH events that spans 7 years of observations. Today, by using our huge KH database, with MMS and THEMIS data when are placed in both hemispheres opposite to each other, is the best time to address this question.

5.2.2 Kelvin-Helmholtz instability under southward IMF

According to theory, the unstable conditions for the KH instability would not be different by the sign of the IMF component perpendicular to the boundary plane, so there should be no difference in the occurrence of KH instability under southward and northward IMF. However, the in-situ observations of the KH waves have been reported to occur preferentially for northward interplanetary magnetic field (IMF) (Kivelson and Chen, 1995; Hasegawa et al. 2004) and only a few KH waves have been reported under southward IMF conditions (Mozer et al., 1994; Hwang et al., 2011; Yan et al., 2014). Mozer et al. (1994) investigated an observation of the linear stage of surface waves observed by Geotail under southward IMF conditions. Hwang et al. (2011) reported the first observation of K-H vortices by Cluster at the dawnside of the

magnetopause under southward IMF. Also recently Yan et al. (2014) published THEMIS observations of KH vortices at the dusk side of the magnetopause under southward IMF. Several explanations for this preference have been suggested, which include the competition with a tearing mode that suppresses KH instability development for large magnetic shear under southward IMF (Chen et al. 1993, 1997) and the formation of a slow rarefaction region with a magnetic pressure maximum just inside the magnetopause under southward IMF (Miura, 1995). Additionally, the formation of a thin KH unstable plasma sheet layer between the northern and southern lobes during southward IMF has a stabilizing effect on the KH instability due to the intense lobe magnetic field (Hashimoto and Fujimoto, 2005). Furthermore, during northward IMF, the formation of a dense LLBL resulting from high-latitude reconnection that lowers the threshold of the KH instability, together with magnetosheath compressional waves that serve as seed fluctuations for the KH instability during northward IMF might be the reason for KH instability preference during northward IMF. To summarize, the current status is that most observations of K-H vortices are reported under northward IMF, and for southward IMF there are only three events reported by (Yan et al. 2014; Hwang et al. 2011; Mozer et al. 1994). Our recent statistical study shows that KH waves occur roughly ~10% of the time under southward IMF. Although this occurrence rate is more than what we expected, it is still about 4 times less than under northward IMF. Our simulation and observations shows irregular, short, and polychromatic KH waves under southward IMF similar to the KH waves reported by Hwang et al. (2011). Hwang et al. (2011) suggested these KH wave behaviors under southward IMF might explain the preferential in-situ detection of KH vortices when the IMF is northward, since these irregular and short structures would leave little chance to observe well-developed KH wave

under southward IMF. Therefore, by using high resolution OpenGGCM simulation under southward IMF, we might be able to explain this atypical behavior of KH waves under southward IMF.

While the simulations serve as a guide, we will use our extensive event database to establish how KH waves during southward IMF differ from those under northward IMF and the causes for those differences. We will bisect the database into subsets of northward and southward IMF KH events. For each of the subsets we will determine the appropriate statistics, for example frequency, wavelength, boundary layer thickness, field magnitude and plasma density on the sheath side, etc. These parameters will then be contrasted and we will be able to eliminate some of the hypotheses that have been discussed above.

Bibliography

Angelopoulos V., Sibeck D., Carlson C., McFadden J., Larson D., Lin R., Bonnell J., Mozer F., Ergun R., Cully C., Glassmeier K., Auster U., Roux A., LeContel O. Frey S., Phan T., Mende S., Frey H., Donovan E., Russell C., Strangeway R., Liu J., Mann I., Rae I., Raeder J., Li X., Liu W., Singer H., Sergeev V., Apatenkov S., Parks G., Fillingim M., Sigwarth J. (2008), First results from the THEMIS mission. *Space Sci. Rev.* 141, 453–476.

Asamura, K, Chaston, C.C, Y. Itoh, M. Fujimoto, T. Sakanoi, Y. Ebihara, A. Yamazaki, M. Hirahara, K. Seki, Y. Kasaba, M. Okada, (2009), Sheared flows and small-scale Alfvén wave generation in the auroral acceleration region. *Geophys. Res. Lett.* 36, 5105. doi:10.1029/2008GL036803.

Aubry, M. P., M. G. Kivelson, and C. T. Russell (1971), Motion and structure of the magnetopause, *J. Geophys. Res.*, 76, 1673–1696.

Auster, H. U., Glassmeier, K. H., Magnes, W., Aydogar, O., Baumjohann, W., Constantinescu, D., Fischer, D., Fornacon, K. H., Georgescu, E., Harvey, P., Hillenmaier, O., Kroth, R., Ludlam, M., Narita, Y., Nakamura, R., Okrafka, K., Plaschke, F., Richter, I., Schwarzl, H., Stoll, B. (2008), The THEMIS fluxgate magnetometer. *Space Sci. Rev.* 141, 235–264.

Baker, D. N., Pulkkinen T. I., Li X., Kanekal S. G., Blake J. B., Selesnick R. S., Henderson M. G., Reeves G. D., Spence H. E., and Rostoker G. (1998), Coronal mass ejections, magnetic clouds, and relativistic magnetospheric electron events: ISTP, *J. Geophys. Res.*, 103, 17,279.

Belcher, J. W., and L. Davis, Jr. (1971), Large-amplitude Alfvénic waves in the interplanetary medium, *J. Geophys. Res.*, 76, 3534.

Berchem, J., J. Raeder, and M. Ashour-Abdalla (1995a), Reconnection at the magnetospheric boundary: Results from global MHD simulations, in *Physics of the Magnetopause*, edited by B. U. Sonnerup and P. Song, vol. 90 of *AGU Geophysical Monograph*, p. 205.

Berchem, J., J. Raeder, and M. Ashour-Abdalla (1995b), Magnetic flux ropes at the high-latitude magnetopause, *Geophys. Res. Lett.*, 22, 1189.

Boardsen, S.A., Sundberg, T., Slavin, J.A., Anderson, B.J., Korth, H., Solomon, S.C. Blomberg, L.G., (2010), Observations of Kelvin-Helmholtz waves along the dusk-side boundary of Mercury's magnetosphere during MESSENGER's third flyby, *Geophys. Res. Lett.*, 37, L12101, doi:10.1029/2010GL043606.

Bucciantini, N, Amato, E, Del Zanna, L, (2005), Relativistic MHD simulations of pulsar bow-shock nebulae. *Astron. Astrophys.* 434, 189–199. doi:10.1051/0004-6361:20042205

Chacon, L., D. A. Knoll, and J. M. Finn (2003), Hall MHD effects on the 2D Kelvin-Helmholtz/tearing instability, *Physics Letters A*, 308, Issue 2-3, pp. 187-197.

- Chandrasekhar, S. (1961), Hydrodynamic and hydromagnetic stability, in International Series of Monographs on Physics, Oxford Univ. Press, New York.
- Chapman, S. and V. C. A. Ferraro (1930), A new theory of magnetic storms, *Nature*, 126, 129.
- Chapman, S., and V. C. A. Ferraro (1931a), A new theory of magnetic storms, *Terr. Magn. Atmos. Electr.*, 36(2), 77–97, doi:10.1029/TE036i002p00077.
- Chapman, S., and V. C. A. Ferraro (1931b), A new theory of magnetic storms (continued), *Terr. Magn. Atmos. Electr.*, 36(2), 171–186, doi:10.1029/TE036i003p00171.
- Chapman, S. (1957), Notes on the Solar Corona and the Terrestrial Ionosphere, *Smithsonian Contributions to Astrophysics*, 2, 1.
- Chaston, C.C., Wilber, M., Mozer, F.S., Fujimoto, M., Goldstein, M.L., Acuña, M., Rème, H., Fazakerley, A., (2007), Mode conversion and anomalous transport in Kelvin-Helmholtz vortices and kinetic Alfvén waves at the Earth's magnetopause, *Phys. Rev. Lett.*, 99, 175004-175007, doi: 10.1103/PhysRevLett.99.175004.
- Chaston, C.C, Seki, K. (2010), Small-scale auroral current sheet structuring. *J. Geophys. Res.* 115, 11221, doi:10.1029/2010JA015536.
- Chen, S.-H., Kivelson, M.G., (1993), On nonsinusoidal waves at the Earth's magnetopause, *Geophys. Res. Lett.*, 20, 2699-2702.
- Chen, S.-H., Kivelson, M.G., Gosling, J.T., Walker, R.J. Lazarus, A.J., (1993), Anomalous aspects of magnetosheath flow and of the shape and oscillations of the magnetopause during an interval of strongly northward interplanetary magnetic field, *J. Geophys. Res.*, 98, 5727- 5742.
- Claudepierre, S. G., S. R. Elkington, and M. Wiltberger (2008), Solar wind driving of magnetospheric ulf waves: pulsations driven by velocity shear at the magnetopause, *Journal of Geophysical Research*, 113, A05,218.
- Cowee, M., Winske, D. and Gary, S. P. (2009), Two-dimensional hybrid simulations of super diffusion at the magnetopause driven by Kelvin-Helmholtz instability. *J. Geophys. Res.* 114, A10209.
- Cowley, S. W. H. (1976), Comments on the merging of non-antiparallel magnetic fields, *J. Geophys. Res.*, 81(19), 3455.
- Cowley, S. W. H., and M. Lockwood, (1992), Excitation and decay of solar wind-driven flows in the magnetosphere-ionosphere system, *Ann. Geophys.*, 10, 103-115.
- Cowley, S. W. H., and C. J. Owen, (1989), A simple illustrative model of open flux tube motion over the dayside magnetopause, *Planet. Space Sci.*, 37, 1461.
- Crooker, N. U., R. A. Greenwald, M. Hesse, M.K. Hudson, W. J. Hughes, L. R. Lyons, N.C. Maynard, C. T. Russell, and G.L. Siscoe, (1999), Report from the first geospace environment modeling GEM campaigns:1991-1997, p. cover, *Space science center, IGPS, UCLA*.

- Lin, D., C. Wang, W. Li, B. Tang, X. Guo, and Z. Peng (2014), Properties of Kelvin-Helmholtz waves at the magnetopause under northward interplanetary magnetic field: Statistical study, *J. Geophys. Res. Space Physics*, *119*, 7485–7494, doi:10.1002/2014JA020379.
- Delamere, P.A. (2009), Hybrid code simulations of the solar wind interaction with Pluto. *J. Geophys. Res. (Space Phys.)*, *114*, 3220 (2009). doi:10.1029/2008JA013756.
- Dungey, J. W. (1954), Ionosphere Research Laboratory Report, (69) (Pennsylvania State University).
- Dungey, J. W. (1955), Electrodynamics of the Outer Atmosphere in Physics of the Ionosphere, pp. 229-236.
- Dungey, J. W., (1961), Interplanetary Magnetic Field and the Auroral Zones, *Phys. Rev. Lett.*, *6*, 47-48.
- Eastman, T. E., E. W. Hones, S. J. Bame and J. R. Asbridge (1976), The magnetospheric boundary layer: Site of plasma, momentum and energy transfer from the magnetosheath into the magnetosphere, *Geophys. Res. Lett.*, *3*, 685–688.
- Eastman, T. E., E. W. Hones (1979), Characteristics of the Magnetospheric Boundary Layer and Magnetopause Layer as Observed by Imp 6, *J. Geophys. Res.*, *84(A5)*, 2019- 2028.
- Elkington, S. R., M. K. Hudson, and A. A. Chan (1999), Acceleration of relativistic electrons via drift-resonant interaction with toroidal-mode Pc-5 ULF oscillations, *Geophys. Res. Lett.*, *26*, 3273.
- Elkington, S. R., M. K. Hudson, and A. A. Chan (2003), Resonant acceleration and diffusion of outer zone electrons in an asymmetric geomagnetic field, *J. Geophys. Res.*, *108*, 1116.
- Elkington, S. R. (2006), A review of ULF interactions with radiation belt electrons, Magnetospheric ULF Waves: Synthesis and New Directions. *Geophys. Monogr. Ser 169*, 177–193.
- Elphic, R. C. (1990), Observations of flux transfer events: Are FTEs flux ropes, islands, Q7 or surface waves? *Phys. Magn. Flux Ropes Geophys. Monogr. Ser 58*.
- Elphic, R. C., Baumjohann, W., Cattell, C. A., Lu 'hr, H., and Smith, M. F. (1994), A search for upstream pressure pulses associated with flux transfer events: An AMPTE/ISEE case study, *J. Geophys. Res.*, *99*, 13 521–13 527.
- Elphic, R. C. (1995), Observations of flux transfer events: A review. *Phys. Magnetopause Geophys. Monogr. Ser 90*.
- Fairfield, D. H., Global (1979), aspects of the Earth's magnetopause, in Magnetospheric Boundary Layers, edited by *J. Lemaire*, vol. 148 of ESA Special Publication, pp. 5–13.
- Fairfield, D. H., Baumjohann, W., Paschmann, G., Lu 'hr, H., and Sibeck, D. G. (1990), Upstream pressure variations associated with the bow shock and their effects on the magnetosphere, *J. Geophys. Res.*, *95*, 3773–3786.
- Fairfield, D. H., Geotail (2000), Observations of the Kelvin-Helmholtz instability at the equatorial

magnetotail boundary for parallel northward fields, *J. Geophys. Res.*, *105*, 21,159.

Fairfield, D. H., A. Otto, T. Mukai, S. Kokubun, R. P. Lepping, J. T. Steinberg, A. J. Lazarus, and T. Yamamoto (2000), Geotail observations of the Kelvin-Helmholtz instability at the equatorial magnetotail boundary for parallel northward fields, *J. Geophys. Res.*, *105*, A9, pp. 21159-21174.

Fairfield, D. H., C. J. Farrugia, T. Mukai, T. Nagai, and A. Fedorov (2003), Motion of the dusk flank boundary layer caused by solar wind pressure changes and the Kelvin-Helmholtz instability: 10-11 January 1997, *J. Geophys. Res.*, *108*, A12, pp. SMP 20-1, Cite ID 1460, doi: 10.1029/2003JA010134.

Fairfield, D.H., Kuznetsova, M.M., Mukai, T., Nagai, T., Gombosi, T.I., Ridley, A.J., (2007), Waves on the dusk flank boundary layer during very northward interplanetary magnetic field conditions: observations and simulation, *J. Geophys. Res.*, *112*, A08206, doi:10.1029/2006JA012052.

Farrugia, C. J., Elphic, R. C., Southwood, D. J., and Cowley, S. W. H. (1987), Field and flow perturbations outside the reconnected field line region in flux transfer events, *Theory, Planet. Space Sci.*, *35*, 227–240.

Farrugia, C. J., Southwood, D. J., Cowley, S. W. H., Rijnbeek, R. P., and Daly, P. W. (1987), Two-regime flux transfer events, *Planet. Space Sci.*, *35*, 737–744.

Farrugia, C. J., Rijnbeek, R. P., Saunders, M. A., Southwood, D. J., Rodgers, D. J., Smith, M. F., Chaloner, C. P., Hall, D. S., Christiansen, P. J., and Woolliscroft, L. J. C. (1988), A multi-instrument study of flux transfer event structure, *J. Geophys. Res.*, *93*, 14 465–14 477.

Farrugia, C. J., Gratton, F. T., Contin, J., Cochechi, C. C., Arnoldy, R. L., Ogilvie, K. W., Lepping, R. P., Zastenker, G. N., Nozdrachev, M. N., Fedorov, A., Sauvaud, J.-A., Steinberg, J. T., Rostoker, G., (2000), Coordinated Wind, Interball/tail, and ground observations of Kelvin-Helmholtz waves at the near-tail, equatorial magnetopause at dusk: January 11, 1997, *J. Geophys. Res.*, *105*, 7639.

Farrugia, C.J, Gratton, F. T. (2011), Aspects of magnetopause/magnetosphere response to interplanetary discontinuities, and features of magnetopause Kelvin–Helmholtz waves, *Journal of Atmospheric and Solar-Terrestrial Physics*, *73*, 40-51.

Fejer, J. A. (1964), Hydromagnetic stability at a fluid velocity discontinuity between compressible fluids, *Phys. Fluids*, *7*, 499.

Freeman, J. W., C. S. Warren, and J. J. Maguire (1968), Plasma flow directions at the magnetopause on January 13-14, 1967, *J. Geophys. Res.*, *73*, 5719.

Foullon, C., C. J. Farrugia, A. N. Fazakerley, C. J. Owen, F. T. Gratton, and R. B. Torbert, (2008), Evolution of Kelvin-Helmholtz activity on the dusk flank magnetopause, *J. Geophys. Res.*, *113*, A11203, doi:10.1029/2008JA013175.

Fujimoto, M., T. Terasawa (1994), Anomalous ion mixing within an MHD scale Kelvin-Helmholtz vortex, *J. Geophys. Res.*, *99*, 8601.

Fujimoto, M., A. Nishida, T. Mukai, Y. Saito, T. Yamamoto, and S. Kokubun (1996), Plasma entry from

the flanks of the near-Earth magnetotail: Geotail observations in the dawnside LLBL and the plasma sheet, *J. Geomag. Geoelec.*, *48*, 711.

Fujimoto, M., T. Mukai, H. Kawano, M. Nakamura, A. Nishida, Y. Saito, T. Yamamoto, and S. Kokubun (1998), Structure of the low-latitude boundary layer: A case study with Geotail data, *J. Geophys. Res.*, *103*, 2297.

Giovanelli, R. G (1947), Magnetic and electric phenomena in the sun's atmosphere associated with sunspots. *Mon. Not. R. Astron. Soc.*, 107:338.

Gratton, F. T., Bender L., Farrugia, C. J., Gnani, G. (2004), Concerning a problem on the Kelvin-Helmholtz stability of the thin magnetopause. *J. Geophys. Res.* *109*, A04211.

Gold, T. (1959), Motions in the magnetosphere of the Earth, *J. Geophys. Res.*, *64*(9), 1219–1224, doi:10.1029/JZ064i009p01219.

Gurnett, D. A., and A. Bhattacharjee (2005), Introduction to Plasma Physics With Space and Laboratory Applications, Cambridge University Press, Cambridge, United Kingdom.

Gunell, U.V. Amerstorfer, H. Nilsson, C. Grima, M. Koepke, M. Fränz, J.D. Winningham, R.A. Frahm, J.-A. Sauvaud, A. Fedorov, N.V. Erkaev, H.K. Biernat, M. Holmström, R. Lundin, S. Barabash (2008), Shear driven waves in the induced magnetosphere of Mars. *Plasma Phys. Control. Fusion* *50*(7), 074018 doi:10.1088/0741-3335/50/7/074018

Haaland, S. and Gjerloev, J. (2013), On the relation between asymmetries in the ring current and magnetopause currents, *J. Geophys. Res.*, *118*, 7593–7604, doi:10.1002/2013JA019345.

Hasegawa, A. (1975), Plasma Instabilities and Nonlinear Effects, *Springer-Verlag*, New York.

Hasegawa, H., Fujimoto M., Phan T.-D., Rème H., Balogh A., Dunlop, M. W., Hashimoto, C., and TanDokoro R. (2004a), Transport of solar wind into Earth's magnetosphere through rolled-up Kelvin-Helmholtz vortices. *Nature* *430*, 755–758.

Hasegawa, H., M. Fujimoto, T. Phan, H. Rème, A. Balogh, M. W. Dunlop, C. Hashimoto, and R. TanDokoro (2004b), Rolled-up Kelvin-Helmholtz vortices and associated solar wind entry at Earth's magnetopauses, *Nature*, *430*, 755.

Hasegawa, H., Fujimoto M., Takagi K., Saito Y., Mukai T., Rème H. (2006), Single-spacecraft detection of rolled-up Kelvin-Helmholtz vortices at the flank magnetopause. *J. Geophys. Res.* *111*, A09203.

Hasegawa, H., Retinò A., Vaivads, A., Khotyaintsev, Y., André, M., Nakamura, T. K. M., The W.-L., Sonnerup, B. U. Ö., Schwartz S. J., Seki Y., Fujimoto M., Saito Y., Rème H., Canu, P. (2009), Kelvin-Helmholtz waves at the Earth's magnetopause: multiscale development and associated reconnection. *J. Geophys. Res.* *114*, A12207.

Hasegawa, H., (2012), Structure and dynamics of the magnetopause and its boundary layers. *Monogr. Environ. Earth Planets* *1*, 71–119.

Hashimoto, C., and M. Fujimoto (2005), Kelvin-helmholtz instability in an unstable layer of finite thick-

ness, *Adv. Space Res.*, 37, 527–531.

Hu, Y. D., Z. X. Liu (1986), Respond and reconnection of magnetic field caused by fluid vorte at the boundary region of magnetopause, paper presented at International Symposium on Space Physics, Chin. Soc. of Space Res., Beijing.

Huba, J. D. (1996), The Kelvin–Helmholtz instability: Finite Larmor radius magnetohydrodynamics, *Geophys. Res. Lett.*, 23, 2907–2910, doi:10.1029/96GL02767.

Hwang, K.-J., Kuznetsova M. M., Sahraoui F., Goldstein M. L., Lee E., Parks G. K. (2011), Kelvin-Helmholtz waves under southward interplanetary magnetic field. *J. Geophys. Res.* 116, A08210.

Hones, E. W. (1972), Measurements of magnetotail plasma flow made with Vela 4B, *J. Geophys. Res.*, (77), 5503-5522.

Kavosi, S., and J. Raeder (2013), THEMIS observations and OpenGGCM simulations of Kelvin-Helmholtz instability, *GEM Summer Workshop*, Snowmass, Colorado, USA.

Kavosi, S., and Raeder J. (2015), Ubiquity of Kelvin-Helmholtz waves at Earth's magnetopause, *Nature Comm.*, 6, 7019, doi:10.1038/ncomms8019.

Kepko, E. L., and H. E. Spence (1972), Observations of discrete, global magnetospheric oscillations directly driven by solar wind density variations, *J. Geophys. Res.*, 108, 1257, DOI:10.1029/2002JA009,676, 2003. Knight, S., Parallel electric fields, *Planet. Space Sci.*, 21, 741.

Kepko, L., H. E. Spence, H. J. Singer (2002), ULF waves in the solar wind as direct drivers of magnetospheric pulsations, *J. Geophys. Res.*, 29, 1197, doi:10.1029/2001GL014405.

Kivelson, M. G., and Z. Pu (1984), The Kelvin-Helmholtz instability on the magnetopause, *Planet. Space Sci.*, (32), 1335-1341.

Kivelson, M. G., J. Etcheto, and J. G. Trotignon (1984), Global compressional oscillations of the Terrestrial magnetosphere: The evidence and a model, *J. Geophys. Res.*, (89), 9851-1984.

Kivelson, M. G., and S. H. Chen (1995), The magnetopause: Surface waves and instabilities and their possible dynamical consequences, in *Physics of the Magnetopause, Geophys. Monogr. Ser.*, vol.(90), edited by P. Song, B. U. O. Sonnerup, and M. F. Thomsen, pp. 257-268, AGU, Washington, D.C.

Kivelson, M. G., and C. T. Russel (1995), Eds., Introduction to Space Physics, *Cambridge University Press*, New York.

Kuo, H., C. T. Russell, and G. Le (1995), Statistical studies of flux transfer events, *J. Geophys. Res.*, 100, 3513 – 3519.

Lee, L. C. and Fu, Z. F. (1985), A theory of magnetic flux transfer at the Earth's magnetopause, *Geophys. Res. Lett.*, 12, 105–108.

Lerche, F. (1966). Validity of the hydromagnetic approach in discussing instability of the magnetospheric

boundary, *J. geophys. Res.*, 7X, (9),2X3.

Li, W., J. Raeder, J. Dorelli, M. Øieroset, and T. D. Phan (2005), Plasma sheet formation during long period of northward IMF, *Geophys. Res. Lett.*, 32, L12S08, doi: 10.1029/2004GL021,524.

Li, W., J. Raeder, M. F. Thomsen, and B. Lavraud (2008b), Solar wind plasma entry into the magnetosphere under northward IMF conditions, *J. Geophys. Res.*, 113, A04,204.

Li, W., J. Raeder, M. Øieroset, and T. D. Phan, (2009), Cold dense magnetopause boundary layer under northward IMF: Results from THEMIS and MHD simulations, *J. Geophys. Res.*, 114, A00C15, doi:10.1029/2008JA013,497.

Lobanov, A. P., Zensus, J.A. (2001), A cosmic double helix in the archetypical quasar 3C273. *Science* 294, 128–131, doi:10.1126/science.1063239.

Lockwood, M. (1991), Flux-transfer events at the dayside magnetopause: transient reconnection or magnetosheath dynamic pressure pulses? *J. Geophys. Res* 96, 5497–5509.

Lockwood, M. and Wild, M. N. (1993), On the quasi-periodic nature of magnetopause flux transfer events, *J. Geophys. Res.*, 98, 5935–5940.

Lockwood, M. and Hapgood, M. A. (1998), On the cause of a magnetospheric flux transfer event, *J. Geophys. Res.*, 103, 26 453–26 478.

Lyon, J. G., J. A. Fedder, and C. M. Mobarry (2004), The Lyon–Fedder–Mobarry (LFM) global MHD magnetospheric simulation code, *J. Atmos. Solar-Terr. Phys.*, 66, 1333.

Masters, A., Achilleos, N., Bertucci, C., Dougherty, M.K., Kanani, S.J., Arridge, C.S., McAndrews, H.J., Coates, A.J., (2009). Surface waves on Saturn's dawn flank magnetopause driven by the Kelvin-Helmholtz instability, *Planet. Space Sci.*, 57, 1769-1778.

Matsumoto, Y., Hoshino, M., (2004), Onset of turbulence induced by a Kelvin-Helmholtz vortex, *Geophys. Res. Lett.*, 31, L02807, doi:10.1029/2003GL018195.

Matsumoto, Y., Hoshino, M., (2006), Turbulent mixing and transport of collisionless plasmas across a stratified velocity shear layer, *J. Geophys. Res.*, 111, A05213, doi:10.1029/2004JA010988.

Matsumoto, Y. and Seki, K. (2010), Formation of a broad plasma turbulent layer by forward and inverse energy cascades of the Kelvin–Helmholtz instability. *J. Geophys. Res.* 115, A10231.

McComas, D. J, Bagenal, F. (2008), Reply to comment by S.W.H. Cowley et al. on “Jupiter: a fundamentally different magnetospheric interaction with the solar wind”. *Geophys. Res. Lett.* 35, 10103, doi:10.1029/ 2008GL034351.

McFadden, J. P., Carlson, C. W., Larson, D., Angelopoulos, V., Ludlam, M., Abiad, R., Elliott, B., Turin, P., Marckwordt, M. (2008), The THEMIS ESA Plasma Instrument and in-flight calibration. *Space Sci. Rev.* 141, 277–302.

Merkin, V. G., J.G. Lyon, S.G. Claudepierre (2013), Kelvin-Helmholtz instability of the magnetospheric

- boundary in a three-dimensional global MHD simulation during northward IMF conditions. *J. Geophys. Res. Space Phys.* 118, 5478–5496, doi:10.1002/jgra.50520
- Miura, A., and P. L. Pritchett (1982), Nonlocal stability analysis of the MHD Kelvin-Helmholtz instability in a compressible plasma, *J. Geophys. Res.*, 87, 7431.
- Miura, A. (1984), Anomalous transport by magnetohydrodynamic Kelvin-Helmholtz instabilities in the solar wind-Magnetosphere interaction, *J. Geophys. Res.*, 89, A2, pp. 801-818.
- Miura, A. (1987), Simulation of Kelvin-Helmholtz instability at the magnetospheric boundary, *J. Geophys. Res.*, 92, A4, pp. 3195-3206.
- Miura, A. (1990), Kelvin-Helmholtz instability for supersonic shear flow at the magnetospheric boundary, *Geophys. Res. Lett.*, 17, No. 6, pp. 749-752.
- Miura, A. (1992), Kelvin-Helmholtz instability at the magnetospheric boundary: Dependence on the magnetosheath sonic Mach number, *J. Geophys. Res.*, 97, A7, pp. 10,655-10,675.
- Miura, A. (1997), Compressible magnetohydrodynamic Kelvin-Helmholtz instability with vortex pairing in two-dimensional transverse configuration, *Phys. Plasmas*, 4, No. 8, pp. 2871-2885.
- Miura, A. (1999), Self-organization in the two-dimensional magnetohydrodynamic transverse Kelvin-Helmholtz instability, *J. Geophys. Res.*, 104, A1, pp. 395-412.
- Miura, A., (1995), Dependence of the Magnetopause Kelvin-Helmholtz Instability on the Orientation of the Magnetosheath Magnetic Field, *Geophys. Res. Lett.*, 22(21), 2993-2996.
- Mozer, F., S. K. Tsuruda, H. Hayakawa, M. Nakamura, S. Kokubun, and T. Yamamoto (1994), The morning side low latitude boundary layer as determined from electric and magnetic field measurements on Geotail, *Geophys. Res. Lett.*, 21, 2983.
- Nakamura, T. K. M., Hayashi, D., Fujimoto, M., Shinohara, I., (2004), Decay of MHD-scale Kelvin-Helmholtz vortices mediated by parasitic electron dynamics, *Phys. Rev. Lett.*, 92, 145001, doi:10.1103/PhysRevLett.92.145001.
- Nakamura, T. K. M., Fujimoto, M., (2005). Magnetic reconnection within rolled-up MHD- scale Kelvin-Helmholtz vortices: Two-fluid simulations including finite electron inertial effects, *Geophys. Res. Lett.*, 32, L21102, doi:10.1029/2005GL023362.
- Nakamura, T.K.M. Fujimoto, M, Otto, A, (2006), Magnetic reconnection induced by weak Kelvin-Helmholtz instability and the formation of the low-latitude boundary layer. *Geophys. Res. Lett.* 33, 14106, doi: 10.1029/2006GL026318
- Nakamura, T. K. M, Fujimoto, M, (2008), Magnetic effects on the coalescence of Kelvin-Helmholtz vortices. *Phys. Rev. Lett.* 101(16), 165002, doi:10.1103/PhysRevLett.101.165002.
- Nakamura, T. K. M. Hasegawa, H. Shinohara, I., (2010), Kinetic effects on the Kelvin- Helmholtz instability in ion-to-magnetohydrodynamic scale transverse velocity shear layers: Particle simulations, *Phys. Plasmas*, 17, 4, 42119-42122, doi:10.1063/1.3385445.

- Nakamura, T.K.M, Hasegawa, H., Shinohara, I., Fujimoto, M., (2011), Evolution of an MHD-scale Kelvin–Helmholtz vortex accompanied by magnetic reconnection: two-dimensional particle simulations. *J. Geophys. Res.* *116*, 3227, doi:10.1029/2010JA016046
- Nakamura, T.K.M, Daughton, W, Karimabadi, H, Eriksson, S, (2013), Three-dimensional dynamics of vortex- induced reconnection and comparison with THEMIS observations. *J. Geophys. Res.* *118*, 5742–5757, doi:10.1002/jgra.50547
- Neudegg, D. A., S. W. H. Cowley, S. E. Milan, T. K. Yeoman, M. Lester, G. Provan, G. Haerendel, W. Baumjohann, B. Nikutowski, J. BuÈchner, U. Auster, K.-H. Fornacon, E. Georgescu. (2000), A survey of magnetopause FTEs and associated flow bursts in the polar ionosphere, *Ann. Geophys.*, *18*, 416 – 435.
- Neugebauer, M., and B. Buti (1990), A search for evidence of the evolution of rotational discontinuities in the solar wind from nonlinear Alfvén waves, *J. Geophys. Res.*, *95*, 13.
- Nishino, M. N., Hasegawa, H., Fujimoto, M., Saito, Y., Mukai, T., Dandouras, I., Rème, H., Retinò, A., Nakamura, R., Lucek, E., and Schwartz, S. J. (2011), A case study of Kelvin–Helmholtz vortices on both flanks of the Earth’s magnetotail, *Planet. Space Sci.*, *59*, 502–509, doi:10.1016/j.pss.2010.03.011.
- Nykyri, K., and Otto, A. (2001), Plasma transport at the magnetospheric boundary due to reconnection in Kelvin-Helmholtz vortices. *Geophys. Res. Lett.* *28*, 3565.
- Nykyri, K., A. Otto, B. Lavraud, C. Mouikis, L. M. Kistler, A. Balogh, and H. Rème (2006), Cluster observations of reconnection due to the Kelvin-Helmholtz instability at the dawnside magnetospheric flank, *Ann. Geophys.*, *24*, 2619.
- Nykyri, K, Foullon. C, (2013), First magnetic seismology of the CME reconnection outflow layer in the low corona with 2.5-D MHD simulations of the Kelvin–Helmholtz instability. *J. Geophys. Res.* *40*, 4154–4159 doi:10.1002/grl.50807.
- Ogilvie, K. W., and R. J. Fitzenreiter (1989), The Kelvin-Helmholtz instability at the magnetopause and inner boundary layer surface, *J. Geophys. Res.*, *94*, 15,113.
- Ong, R.S.B. and Roderick. N (1972), On The Kelvin-Helmholtz Instability of the Earth’s magnetopause, *Planet. Space Sci.* 1972, Vol. 20,1-10.
- Otto, A., and Fairfield, D. H. (2000), Kelvin-Helmholtz instability at the magnetotail boundary: MHD simulation and comparison with Geotail observations. *J. Geophys. Res.* *105*, 21175–21190.
- Otto, A., and K. Nykyri (2003), Kelvin Helmholtz instability and magnetic reconnection: Mass transport at the LLBL, vol. 133, p. 253, *AGU Monogr. Ser.*, American Geophysical Union.
- Paschmann, G., Haerendel, G., Papamastorakis, I., Sckopke, N., Bame, S. J., Gosling, J. T., and Russell, C. T. (1982), Plasma and magnetic field characteristics of magnetic flux transfer events, *J. Geophys. Res.*, *87*, 2159–2168.
- Parker, E. N., (1958), Dynamics of the Interplanetary Gas and Magnetic Fields, *Astrophys. J.*, *128*, 664–676.

- Parker, E. N. (1963), The Solar-Flare Phenomenon and the Theory of Reconnection and Annihilation of Magnetic Fields., *Ap. J. S.*, 8, 177–211.
- Parks, G.P. (2004), *Physics of Space Plasmas An Introduction*, Westview Press.
- Plaschke, F., Taylor, M. G. G. T. and Nakamura, R. (2014), Alternative interpretation of results from Kelvin-Helmholtz vortex identification criteria. *Geop. Res. Lett.* 41, 244–250.
- Pope, S.A., Balikhin, M.A., Zhang, T.L., Fedorov, A.O, Gedalin, M. Barabash, S (2009), Giant vortices lead to ion escape from Venus and re-distribution of plasma in the ionosphere. *J. Geophys. Res.* 36, 7202, doi:10.1029/2008GL036977.
- Pu, Z., and M. G. Kivelson (1983b), Kelvin-Helmholtz instability at the magnetopause: Solution for compressible plasmas, *J. Geophys. Res.*, 88, 841.
- Rae, I. J., Donovan E. F., Mann I. R., Fenrich F. R., Watt C. E. J., Milling D. K., Lester M., Lavraud B., Wild J. A., Singer H. J., Rème H., Balogh A. (2005), Evolution and characteristics of global Pc5 ULF waves during a high solar wind speed interval. *J. Geophys. Res.* 110, A12211.
- Raeder, J., D. Larson, W. Li, E. L. Kepko, and T. Fuller-Rowell (2008), OpenGGCM simulations for the THEMIS mission, *Space Sci. Rev.*, 141, 535.
- Raeder, J. (2003), Global magnetohydrodynamics—A tutorial, in *Space Plasma Simulation*, ed. by J. Büchner, C.T. Dum, M. Scholer (Springer, Berlin).
- Raeder, J., J. Berchem, and M. Ashour-Abdalla (1998), The Geospace Environment Modeling grand challenge: Results from a Global Geospace Circulation Model, *J. Geophys. Res.*, 103, 14,787.
- Raeder, J., J. Berchem, and M. Ashour-Abdalla (1996), The importance of small scale processes in global MHD simulations: Some numerical experiments, in *The Physics of Space Plasmas*, edited by T. Chang and J. R. Jasperse, vol. 14, p. 403, MIT Cent. for Theoret. Geo/Cosmo Plasma Phys., Cambridge, MA.
- Raeder, J. (2006), Flux transfer events: 1. Generation mechanism for strong southward IMF, *Ann. Geophys.*, 24 , 381.
- Raeder, J., W. Li, M. Gilson, and S. Kavosi (2012), Predictions of plasma entry and its ionospheric signatures from global simulations, in *AGU Fall Meeting*, San Francisco, California.
- Rijnbeek, R. P., Cowley, S. W. H., Southwood, D. J., and Russell, C. T. (1982), Observations of reverse polarity flux transfer events at the Earth's magnetopause, *Nature*, 300, 23–26.
- Rijnbeek, R. P., S. W. H. Cowley, D. J. Southwood, and C. T. Russell, (1984), A Survey of Dayside Flux Transfer Events Observed by Isee 1 and 2 Magnetometers, *J. Geophys. Res.*, 89(A2), 786-800.
- Rijnbeek, R. P. and Cowley, S. W. H. (1984), Magnetospheric flux erosion events are flux transfer events, *Nature*, 309, 135–138.
- Rijnbeek, R. P., Farrugia, C. J., Southwood, D. J., Dunlop, M. W., Mier- Jedrzejowicz, W. A. C., Chaloner, C. P., Hall, D. S., and Smith, M. F. (1987), A magnetic boundary signature within flux transfer

events, *Planet. Space Sci.*, 35, 871–878.

Russell, C. T. and McPherron, R. L. (1973), The magnetotail and substorms, *Space Sci. Rev.*, 15, 205–266.

Russell, C. T. and Walker, R. J. (1985), Flux transfer events at Mercury, *J. Geophys. Res.*, 90, 11 067–11 074.

Russell, C. T., and R. C. Elphic (1978), Initial ISEE magnetometer results: Magnetopause observations, *Space Sci. Rev.*, 22, 681–715.

Russell, C. T., and R. C. Elphic (1979), ISEE Observations of Flux Transfer Events at the Dayside Magnetopause, *Geophys. Res. Lett.*, 6(1), 33–36.

Russell, C. T., Berchem, J., and Luhmann, J. G. (1985), On the source region of flux transfer events, *Adv. Space Res.*, 5, 363–368.

Sen, A. (1963), Stability of hydromagnetic Kelvin-Helmholtz discontinuity, *Phys. Fluids*, 6, 1154.

Sharp, D. H. (1984), AN Overview of Rayleigh-Taylor Instability, *Physica D*, 12, 3.

Sibeck, D. G. and Angelopoulos, V. (2008), THEMIS science objectives and mission phases. *Space Sci. Rev.* 141, 35–59.

Sibeck, D. G. (1990), A model for the transient magnetospheric response to sudden solar wind dynamic pressure variations. *J. Geophys. Res.* 95, 3755–3771.

Sibeck, D. G., Lopez, R. E., and Roelof, E. C. (1991), Solar wind control of the magnetopause shape, location, and motion, *J. Geophys. Res.*, 96, 5489–5495.

Slavin, J.A, Acuña, M.H, Anderson, B.J, Baker, D.N, Benna, M, Gloeckler, G, Gold, R.E, G.C. Ho, R.M. Killen, H. Korth, S.M. Krimigis, R.L. McNutt, L.R. Nittler, J.M. Raines, D. Schriver, S.C. Solomon, R.D. Starr, P. Trávníček, T.H. Zurbuchen, (2008). Mercury’s magnetosphere after MESSENGER’s first flyby. *Science* 321, 85 doi:10.1126/science.1159040

Smets, R., D. Delcourt, G. Chanteur, and T. E. Moore, (2002), On the incidence of Kelvin-Helmholtz instability for mass exchange process at the Earth's magnetopause, *Ann. Geo-phys.*, 20, 757- 769.

Song, P., R. C. Elphic, and C. T. Russell (1988), ISEE 1 and 2 observation of the oscillating magnetopause, *Geophys. Res. Lett.*, 15, 744–747.

Song, P., and C. Russell, (1992), Model of the Formation of the Low-Latitude Boundary Layer for Strongly Northward Interplanetary Magnetic Field, *J. Geophys. Res.*, 97(A2), 1411–1420.

Song, P., Le, G., and Russell, C. T. (1994), Observational differences between flux transfer events and surface waves at the magnetopause, *J. Geophys. Res.*, 99, 2309–2320.

Southwood, D. J., Farrugia, C. J., and Saunders, M. A. (1988), What are flux transfer events?, *Planet. Space Sci.*, 36, 503–508.

- Southwood, D. J. (1968), The hydromagnetic stability of the magnetospheric boundary, *Planet. Space Sci.*, 16, 587–605.
- Southwood, D. J. (1979), Magnetopause Kelvin-Helmholtz instability in Proceedings of Magnetospheric Boundary Layers Conference, ESA Scientific and Technical Publications Branch. Noordwijk, The Netherlands.
- Takagi, K., Hashimoto C., Hasegawa H., Fujimoto M., Tan Dokoro R. (2006), Kelvin-Helmholtz instability in a magnetotail flank-like geometry: three-dimensional MHD simulations. *J. Geophys. Res.* 111, A08202.
- Takahashi, K., D. G. Sibeck, P. T. Newell, and H. E. Spence (1991), ULF waves in the low-latitude boundary layer and their relationship to magnetospheric pulsations - A multisatellite observation, *J. Geophys. Res.*, 96, 9503–9519.
- Takahashi, A. Y., K., Anderson, B. J., Korth .H, (2005), The impact of inner magnetospheric ULF waves on the outer radiation belt electrons, *J. Geophys. Res.*, 110, A10, 202.
- Talwar, S. P. (1964), Hydromagnetic stability of the magnetospheric boundary. *J. Geophys. Res.* 69, 2707–2713.
- Taylor, M. G. G. T., Hasegawa, H., Lavraud, B., Phan, T., Escoubet, C. P., Dunlop, M. W., Bogdanova, Y. V., Borg, A. L., Volwerk, M., Berchem, J., Constantinescu, O. D., Eastwood, J. P., Masson, A., Laakso, H., Soucek, J., Fazakerley, A. N., Frey, H. U., Panov, E. V., Shen, C., Shi, J. K., Sibeck, D. G., Pu, Z. Y., Wang, J., and Wild, J. A. (2012), Spatial distribution of rolled up Kelvin–Helmholtz vortices at Earth’s dayside and flank magnetopause, *Ann. Geophys.*, 30, 1025–1035, doi:10.5194/angeo-30-1025-2012.
- Thomas, B., and E. Smith, (1980), The Parker Spiral Configuration of the Interplanetary Magnetic Field Between 1 and 8.5 AU, *J. Geophys. Res.*, 85(A12), 6861-6867.
- Thomsen, M. F., J. E. Borovsky, R. M. Skoug, and C. W. Smith (2003), Delivery of cold, dense plasma sheet material into the near-Earth region, *J. Geophys. Res.*, 108, 1151, doi: 10.1029/2002JA009, 544.
- Thomas, V.A., Winske, D. (1991), Kinetic simulation of the Kelvin-Helmholtz instability at the Venus ionopause. *Geophys. Res. Lett.* 18, 1943–1946.
- Thomas, V.A., Winske, D. (1993), Kinetic simulations of the Kelvin-Helmholtz instability at the magnetopause. *J. Geophys. Res.* 98, 11425–11438.
- Umeda, T., Miwa, J., Matsumoto, Y., Nakamura, T. K. M., Togano, K., Fukazawa, K., Shinohara, I., (2010), Full electromagnetic Vlasov code simulation of the Kelvin.Helmholtz instability, *Phys. Plasmas*, 17, 5, 52311-52321, doi: 10.1063/1.3422547.
- Walker, A. D. M. (1981), The Kelvin-Helmholtz instability in the low-latitude boundary layer. *Planet. Space Sci.* 29, 1119–1133.
- Walker, R., and C. Russell (1985), Solar-wind interactions with magnetized planets, in Introduction to Space Physics, ed. M.G. Kivelson and C.T. Russell, *Cambridge University Press*, Cambridge.

- Walsh, B. M., Sibeck, D. G., Wang, Y., and Fairfield, D. H. (2012), Dawn- dusk asymmetries in the Earth's magnetosheath, *J. Geophys. Res.*, *117*, A12211, doi:10.1029/2012JA018240.
- Walters, G. K. (1964), Effect of Oblique Interplanetary Magnetic Field on Shape and Behavior of the Magnetosphere, *J. Geophys. Res.*, *69*, 1769–1783, doi:10.1029/JZ069i009p01769.
- Wang, Y. L., Elphic, R. C., Lavraud, B., Taylor, M. G. G. T., Birn J., Raeder J., Russell C. T., Kawano H., Zong Q.-G., Zhang H., Zhang X. X., Friedel R. H. (2005), Initial results of high-latitude magnetopause and low-latitude flank flux transfer events from 3 years of Cluster observations. *J. Geophys. Res.* *110*, A1122.
- Wang, Y. L., J. Raeder, and C. T. Russell (2004), Plasma depletion layer: Structure and forces, *Ann. Geophys.*, *22*, 1001.
- Wang, Y. L., J. Raeder, C. T. Russell, T. D. Phan, and M. Manapat (2003), Plasma depletion layer: Event studies with a global model, *J. Geophys. Res.*, *108*, 1010, doi:10.1029/2002JA009, 281.
- Wang, C, Belcher, J.W. (1998), Numerical investigation of hydrodynamic instabilities of the heliopause. *J. Geophys. Res.* *103*, 247. doi:10.1029/97JA02773.
- Wu, C. C. (1986), Kelvin-Helmholtz instability at the magnetopause boundary, *J. Geophys. Res.*, *91*, A3, pp. 3042-3060.
- Yan, G. Q., Mozer, F. S., Shen C., Chen T., Parks G. K., Cai C. L., McFadden J. P. (2014) Kelvin-Helmholtz vortices observed by THEMIS at the dusk side of the magnetopause under southward interplanetary magnetic field. *Geophys. Res. Lett.* *41*, 4427–4434.